

INFORMATION TO USERS

This manuscript has been reproduced from the microfilm master. UMI films the text directly from the original or copy submitted. Thus, some thesis and dissertation copies are in typewriter face, while others may be from any type of computer printer.

The quality of this reproduction is dependent upon the quality of the copy submitted. Broken or indistinct print, colored or poor quality illustrations and photographs, print bleedthrough, substandard margins, and improper alignment can adversely affect reproduction.

In the unlikely event that the author did not send UMI a complete manuscript and there are missing pages, these will be noted. Also, if unauthorized copyright material had to be removed, a note will indicate the deletion.

Oversize materials (e.g., maps, drawings, charts) are reproduced by sectioning the original, beginning at the upper left-hand corner and continuing from left to right in equal sections with small overlaps. Each original is also photographed in one exposure and is included in reduced form at the back of the book.

Photographs included in the original manuscript have been reproduced xerographically in this copy. Higher quality 6" x 9" black and white photographic prints are available for any photographs or illustrations appearing in this copy for an additional charge. Contact UMI directly to order.

UMI

A Bell & Howell Information Company
300 North Zeeb Road, Ann Arbor MI 48106-1346 USA
313/761-4700 800/521-0600

New Joint Time-Frequency Transforms with Improved Properties

BY

Osama Abdl-Wahhab Ahmed

A Dissertation Presented to the
FACULTY OF THE COLLEGE OF GRADUATE STUDIES
KING FAHD UNIVERSITY OF PETROLEUM & MINERALS
DHAHRAN, SAUDI ARABIA

In Partial Fulfillment of the
Requirements for the Degree of

DOCTOR OF PHILOSOPHY

In

Electrical Engineering

UMI Number: 9907233

UMI Microform 9907233

Copyright 1998, by UMI Company. All rights reserved.

**This microform edition is protected against unauthorized
copying under Title 17, United States Code.**

UMI

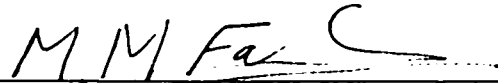
**300 North Zeeb Road
Ann Arbor, MI 48103**

**KING FAHD UNIVERSITY OF PETROLEUM AND MINERALS
DHAHRAN 31261, SAUDI ARABIA**

COLLEGE OF GRADUATE STUDIES

This Dissertation written by Osama Abdel Wahhab Ahmed
under the direction of his Dissertation Advisor and approved by his Dissertation
Committee, has been presented to and accepted by the Dean of the College of Grad-
uate Studies, in partial fulfillment of the requirements for the degree DOCTOR OF
PHILOSOPHY

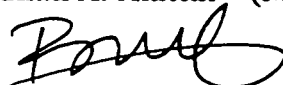
Dissertation Committee



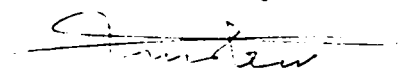
Dr. Moustafa M. Fahmy (Advisor)



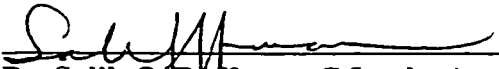
Dr. Adnan A. Alattar (Member)



Dr. Maamar Bettayeb (Member)



Dr. Saud A. Al-Semari (Member)



Dr. Salih O. Daifuaa (Member)

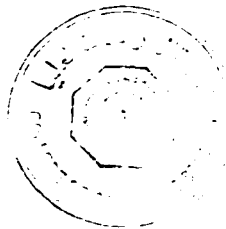


Department Chairman



Dean, College of Graduate Studies

26/7/98
Date



To my mother, my wife and my daughters for their boundless love.

ACKNOWLEDGMENTS

Praise be to God, the Merciful, the Compassionate, the Lord of the Two Worlds, and blessing and peace upon the Prince of Prophets, our master Muhamed, whom God bless and preserve with abiding and continuing peace and blessings until the Day of the Faith!

First of all I have to express my sincere gratitude for my advisor Professor Moustafa Fahmy for offering me continuous support, unfailing enthusiasm, and good ideas. I will always remember his relentless encouragement and friendship.. I also wish to thank the other member of my Dissertation Committee Dr. Adnan El-Attar, Dr. Maamar Bettayeb, Dr. Saud Al-Semari, and Dr. Salih Daffuaa for their valuable advice and support.

The support of King Fahd University of Petroleum and Minerals is gratefully acknowledged.

Finally, no words will be enough to express my indebtedness to my mother and my wife.

TABLE OF CONTENTS

LIST OF FIGURES	ix
LIST OF TABLES	xiii
DISSERTATION ABSTRACT	xiv
CHAPTER 1: INTRODUCTION	1
CHAPTER 2: PROBLEM DEFINITION	10
2.1 Mathematical Background	10
2.1.1 Expansion Theory	11
2.1.2 Fourier Transform	12
2.1.3 Short Time Fourier Transform	13
2.1.4 Uncertainty Principle	15
2.2 Gabor Expansion	16
2.3 The Concept of Biorthogonal Function	21
2.4 Real Gabor Expansion	25
2.5 Requirements for Universal Joint Time-Frequency Transform	26
2.6 Existing Solutions	30
2.6.1 Over-sampling Solution	30
2.6.1.1 Dependent Coefficients	31
2.6.2 Real Gabor Transform	34
CHAPTER 3: MATRIX FORM AND STABILITY OF DISCRETE GABOR TRANSFORMS	41
3.1 Introduction	41
3.2 Matrix Form of Discrete Gabor Transforms	42
3.3 Aperiodic Real Gabor Transform	46

3.4 The Biorthogonal Function of Discrete Gabor Transforms	49
3.5 Stability of Discrete Linear Transforms	54
3.6 Stability of Discrete Gabor Transforms	56
CHAPTER 4: NON-SEPARABLE SAMPLING OF THE REAL GABOR TRANSFORM	58
4.1 Non-separable Sampling	59
4.2 Hexagonal Real Gabor Transform	61
4.3 Practical Calculation of H^{-1}	67
4.4 Practical Calculation of the Hexagonal Real Gabor Transform coefficients	69
4.5 Conclusion	73
CHAPTER 5: ORTHOGONAL GABOR-DCT TRANSFORM	78
5.1 Introduction	78
5.2 Real Gabor Transform: Second Visit	80
5.3 Stability of Gabor-DCT Transforms	82
5.4 Orthogonal Gabor-DCT Transform	82
5.5 Results	89
5.6 Conclusion	91
CHAPTER 6: STABLE CRITICALLY-SAMPLED JTF TRANSFORM WITH LOCALIZED BIORTHOGONAL FUNCTION	93
6.1 Introduction	94
6.2 The Proposed Transform	95
6.3 The Resulting Biorthogonal Function	106
6.4 Practical Calculation of the Transform Coefficients	112
6.4.1 Calculation of H^{-1}	115

6.4.2 Calculation of the Transform Coefficients	118
6.4.2.1 Method 1	118
6.4.2.2 Method 2	119
6.4.3 Truncated Gaussian Function	120
6.5 Conclusion	123
CHAPTER 7: APPLICATION: NOISE REDUCTION FOR NUCLEAR MAGNETIC RESONANCE FREE INDUCTION DECAY SIGNALS	126
7.1 Introduction	126
7.2 Basic Theory of NMR	128
7.3 Noise Removal of NMR-FID Signals	130
7.4 Behavior of the Transform Coefficients for Modulated Exponent.	132
7.5 Removing Noise from Phosphorus FID Signal.	139
7.6 Removing Noise from a Real-life FID Signal	149
7.7 Conclusion	155
CHAPTER 8: CONCLUSION	158
8.1 Recommendations and Future Work	161
APPENDIX A: PERMUTATION MATRICES	164
APPENDIX B: CIRCULANT MATRICES AND TOEPLITZ MATRICES.	166
APPENDIX C: DISCRETE CRITICALLY-SAMPLED GABOR TRANSFORMS	169
C.1 Periodic Complex Gabor Transform	169
C.2 Aperiodic Complex Gabor Transform	170
C.3 Periodic Real Gabor Transform	172
C.4 Aperiodic Real Gabor Transform	174

APPENDIX D: DISCRETE OVER-SAMPLED GABOR TRANSFORM	176
APPENDIX E: DISCRETE COSINE TRANSFORM TYPE IV	179
APPENDIX F: DISCRETE SINE TRANSFORM TYPE IV (DST-IV)	180
APPENDIX G: GENERALIZED GABOR TRANSFORM	181
REFERENCES	184

LIST OF FIGURES

1	JTF representation of a two chirp function. Below, the time representation. On the right, the frequency representation.	3
2	JTF representation of a non-linear chirp function. Below, the time representation. On the right, the frequency representation.	3
3	Ionized impulse signal (Data courtesy of Non-Proliferation & International security Division, Los Alamos National Laboratory)	4
4	The ionized impulse signal masked from noisy background	4
5	The ionized impulse signal before and after filtering	4
6	Types of the bilinear (non-linear) JTF representations.	6
7	Types of the linear JTF representations.	6
8	JTF representation of the 2-chirp function using Wigner-Ville distribution.	7
9	A linear chirp signal and its Short Time Fourier Transform.	14
10	The Gaussian function, g , in both time and frequency domains	17
11	Expansion of arbitrary signal in complex elementary signals.	19
12	The biorthogonal function of the complex Gabor transform	23
13	The time signal $x(t)$	24
14	The Gabor coefficients of $x(t)$	24
15	Cosine type elementary function.	27
16	Sine type elementary function.	27
17	Expansion of a signal in cosine-type and sine-type elementary signals.	28
18	The biorthogonal function of the over sampling case for $OVSR = 2$	32

19	The biorthogonal function of the over sampling case for $OVSR = 4$	33
20	A low-pass filter	35
21	The biorthogonal function of the real Gabor Transform.	40
22	The biorthogonal function, $\gamma_m(k)$, of the aperiodic Real Gabor Transform for $m = 0, 1, 2, 3$	50
23	The biorthogonal function, $\gamma_m(k)$, of the aperiodic Real Gabor Transform for $m = 4, 5, 6, 7$	51
24	The biorthogonal function of the periodic and the aperiodic Real Gabor Transform for $m = 0$	52
25	Packing a 2-D space with squares.	60
26	Packing a 2-D space with hexagons.	60
27	Constructing Hexagon lattice JTF plane sampling set (b) from Square lattice JTF plane sampling set (a)	62
28	The discrete biorthogonal function of the Hexagonal Real Gabor transform.	66
29	Comparison between the biorthogonal function in the frequency domain in (a) the case of uniform sampling and (b) hexagon sampling.	68
30	Truncated discrete Gaussian window to a length of $2N$. $M = N = 8$	72
31	A test signal composed of a concatenation of two sinusoids with different amplitudes and frequencies.	74
32	JTF representation of the test signal using the truncated hexagon real Gabor transform with length $2N$	74
33	JTF representation of the test signal using the hexagon real Gabor transform.	75
34	JTF representation of the test signal using the truncated real Gabor transform with length $2N$	75

35	JTF representation of the test signal using the truncated real Gabor transform with length $3N$	76
36	Example of a window function for the orthogonal Gabor-DCT, $M = N = 16$ and $m = 2$	90
37	Another window function for the orthogonal Gabor-DCT, $M = N = 16$ and $m = 2$	92
38	Expansion of a signal in cosine-type elementary signals.	97
39	The new JTF distribution. $a_{n,m}$ belongs to $h_{m,n}^{even}(t)$ and $b_{n,m}$ belongs to $h_{m,n}^{odd}(t)$	99
40	The biorthogonal function of the proposed transform.	113
41	JTF representation of the test signal using the proposed transform.	114
42	Effect of truncating the Gaussian window into a length of $2N$ in the frequency domain.	124
43	Modulated exponent in time (e) is the multiplication of non-decaying complex exponent (a) with the exponential decay function (c). In frequency, modulated exponent (f) is the convolution of the non-decaying complex exponent (b) with the exponential decay function (d).	133
44	The transform coefficients, magnitudes, of the modulated exponent.	135
45	The transform coefficients of the modulated exponent. (surface plot)	136
46	The transform coefficients of the modulated exponent after adding AWGN.	140
47	Real part of the Phosphorus FID signal without noise.	141
48	Imaginary part of the Phosphorus FID signal without noise.	142
49	Spectrum of the Phosphorus FID without noise.	143
50	Spectrum of the Phosphorus FID with added zero mean Gaussian noise with St. Dev. = 2000.	144

51	Same spectrum after removing the noise by the proposed method.	146
52	The square error in the original signal (a), after removing the noise with the proposed transform (b) , and after removing the noise with GGT (c).	147
53	Same spectrum after removing the noise by the GGT method.	148
54	Real part of the real-life NMR-FID signal.	150
55	The spectrum of the real-life NMR-FID signal.	151
56	The transform coefficients (magnitude) for the same signal.	152
57	The transform coefficients of the same signal after thresholding with $thr = 66$	153
58	The resulting spectrum of the same signal after thresholding.	154
59	GGT coefficients of the NMR-FID signal.	156
60	The discrete biorthogonal function of periodic complex Gabor transform centered on the analysis window $m = 3$	171
61	The biorthogonal function of the periodic and the aperiodic complex Gabor Transform cenetred on the analysis window $m = 3$	173
62	The discrete biorthogonal function of periodic real Gabor transform centered on the analysis window $m = 3$	175
63	The discrete biorthogonal function of the over-sampling case, $OVSR = 4$	178
64	The analysis window function used in GGT.	182
65	The discrete biorthogonal function of GGT.	183

LIST OF TABLES

1	Condition number of various Gabor transforms	57
2	Operational savings of the truncated hexagon sampling method over the Zak based one	72
3	Condition number of various implementations of Gabor-DCT transform	83
4	Correlation between $h_{m,n}$ and $h_{m+m',n+n'}$ in the Real Gabor transform	96
5	Correlation between $h_{m,n}$ and $h_{m+m',n+n'}$ in the new transform	98
6	Condition number of the proposed method compared to critically-sampled Gabor Transforms	105
7	Condition number of the proposed transform compared to the over-sampled gabor Transform	105
8	Operational savings of the proposed method over the Zak based one.	124
9	Parameters of Simulated Phosphorus FID	140
10	Condition number of the GGT	182

DISSERTATION ABSTRACT

Osama Abdel Wahhab Ahmed

New Joint Time-Frequency Transforms with Improved Properties

Electrical Engineering

May 24, 1998

In this dissertation, the problem of the Joint Time-Frequency (JTF) transforms is addressed with the objective of developing *linear critically-sampled* JTF transform with optimal characteristics, namely being *stable* and having the biorthogonal function and the analysis function both *localized* in the time domain and in the frequency domain.

First, the non-separable sampling of the JTF plane for the real Gabor transform is introduced. It is shown that the hexagon sampling, in particular, enhances the localization of the biorthogonal function in the frequency domain while maintaining all other properties. Second, the stability is considered with the objective of developing an orthogonal linear JTF transform (thus achieving the highest possible stability). The orthogonality conditions on the analysis window function (leading to orthogonal transform) have been derived. Two functions satisfying these conditions are presented. Third, using alternate types of kernels, a *stable linear critically-sampled* JTF transform with *localized biorthogonal function* and *analysis function* has been developed.

Since the computational requirements of all JTF transforms is an obstacle to their practical usage, practical implementation which dramatically reduces the computational requirements is developed for all of the above proposed transform.

To demonstrate the usefulness of the proposed transforms in real-life situation, the third transform is applied to the traditional, yet difficult, problem of noise reduction of the nuclear magnetic resonance signals. It is shown that the proposed transform gives far better results with lower computational requirements than other JTF transforms.

DOCTOR OF PHILOSOPHY DEGREE
KING FAHD UNIVERSITY OF PETROLEUM AND MINERALS
Dhahran, Saudi Arabia
May 24, 1998

بِسْمِ اللَّهِ الرَّحْمَنِ الرَّحِيمِ

خلاصة الرسالة

أسامة عبد الوهاب أحمد سالم

تحويلات وقت وتردد مشتركة جديدة بمواصفات محسنة

هندسة كهربائية

مايو ١٩٩٨

في هذه الأطروحة نُوقِشت مشاكل تحويلات الوقت والتردد المشتركة بهدف إنشاء تحويلة خطية ذات تحليل حرج بمواصفات مثالية. هذه المواصفات المثالية هي أن تكون التحويلة متزنة وأن يكون كلاً من الدالة الثنائية التعامد والدالة المحللة متمركزتين في مجال الوقت ومجال التردد معاً. ولتحقيق هذا فقد قدمنا ثلاث اقتراحات: أولاً: التحليل الغير قابل للانفصال لمستوي الوقت والتردد لتحويلة حابور الحقيقية. وقد وجد أن التقسيم السداسي لهذا المستوي يحسّن تمرکز الدالة الثنائية التعامد في مجال التردد مع المحافظة على باقي الصفات الأخرى كما هي. ثانياً: رُكِّزَ علي خاصية الاتزان بحيث كان الهدف هو إنشاء تحويلة خطية عمودية (وبهذا تكون في حالة الاتزان المثلى) ذات تحليل حرج. وقد استنتجنا شروط التعامد أي الشروط التي تجعل التحويلة الخطية عمودية. ثالثاً: باستعمال نوعين مختلفين من الدوال الأولية بالتبادل استطعنا الحصول على تحويلة خطية متزنة ذات تحليل حرج بالإضافة إلى الدالة الثنائية التعامد والدالة المحللة متمركزتين في مجال الوقت ومجال التردد معاً. وبما أن المتطلبات الحسابية لتحويلات الوقت والتردد المشتركة تمثل عقبة في طريق استخدام هذه التحويلات في المجالات العملية فقد قمنا بتطوير طريقة عملية لاختصار المتطلبات الحسابية لكل التحويلات المطروحة. ولتوضيح فائدة هذه التحويلات في الحياة العملية فقد طبقنا التحويلة الثالثة علي عملية إزالة الضوضاء من إشارات الرنين المغناطيسي النووي وقد تبين في هذا التطبيق أن التحويلة المطروحة أعطت نتائج أفضل بكثير من أي تحويلة أخرى منشورة بالإضافة إلى متطلبات حسابية أقل.

درجة الدكتوراه في الفلسفة

جامعة الملك فهد للبترول والمعادن

الظهران المملكة العربية السعودية

مايو ١٩٩٨

CHAPTER 1

INTRODUCTION

A standard goal in *signal processing* is to find a representation in which certain attributes of the signal are made explicit. In principle, there is an infinite number of ways to describe a signal. The most fundamental variables in signal processing are *time* and *frequency*. Frequency representations usually have simpler patterns than the time waveforms and these have been widely used in many applications like filter design, control, system identification, image enhancement, . . .etc. In Fourier transform, the signal is compared to complex sinusoidal functions which spread into the entire time domain. As a result, the Fourier transform does not explicitly indicate how a signal's frequency content evolve in time. Even though the phase of the Fourier transform relates to time shifting, it is difficult to extract time information from the phase. On the other hand, the frequency contents of the majority of signals encountered in the real world change with time. Thus, in many real applications, it is far more useful to characterize the signal in time and frequency domain simultaneously. This has led to the currently increasingly popular subject, *joint time-frequency (JTF) analysis*. In Figures 1 and 2, the JTF representation obtained by Gabor transform for a two chirp function and a non-linear chirp function are plotted. For comparison, the time representa-

tion and the frequency representation are also plotted. It is clear from the two figures that the signal is easily characterized in the JTF representation than in the time or the frequency representations.

JTF analysis is a powerful technique for detection and estimation of signal corrupted by noise. Random noise tends, in general, to spread in JTF domain, while the signal itself concentrates in a relatively small range. Thus, one can enhance the signal-to-noise ratio significantly by JTF analysis. For example, Fig. 3 depicts the impulse signal received by the U.S. Department of Energy ALEXIS/BLACKBREAD satellite plotted from [1]. After passing through the ionosphere (dispersive media) the signal becomes a non-linear chirp signal. The signal is severely corrupted by noise. As shown from the figure, neither time waveform nor the power spectrum indicate the existence of the impulse signal. This impulse signal is, however, very clear in the time-frequency plot. Fig. 4 shows the signal after filtering it in the joint time-frequency domain. Figure 5 shows the signal before (gray) and after filtering (dark).

In image compression, transform-based coding methods (like DCT, DFT, DST) are very popular because they provide the best quality for the same compression ratio due to their decorrelative properties and because of the existence of fast algorithms for computing the coefficients that can be implemented easily in VLSI. They, however, are not localized in the spatial domain. Therefore, they must be calculated over a number of spatial partitioned regions (blocks). This method suffers from blocking effects especially for very low bit rate compression. On the other hand, Gabor functions have optimal localization in the joint spatial and frequency domain. Besides, Gabor transform achieves the lowest bound on the

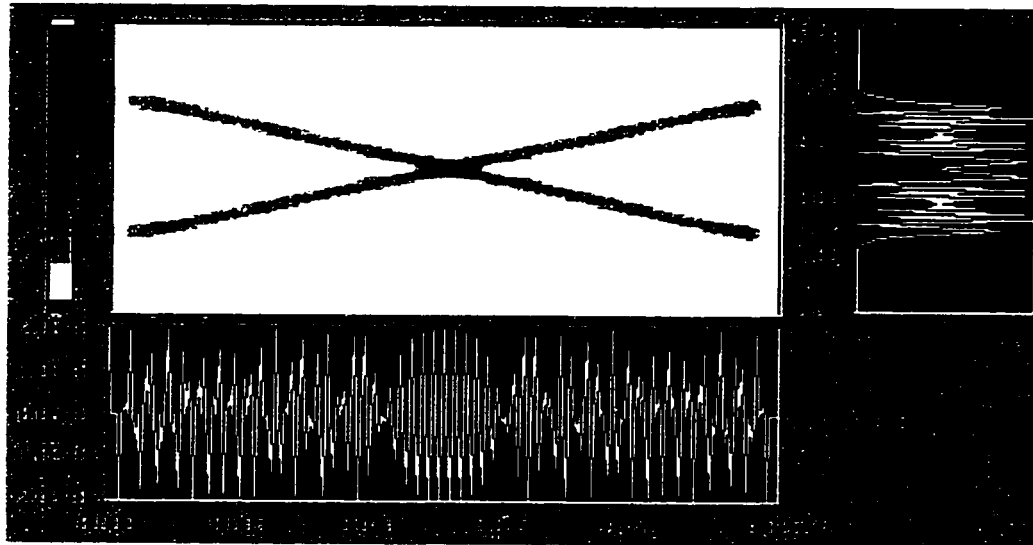


Figure 1: JTF representation of a two chirp function. Below, the time representation. On the right, the frequency representation.

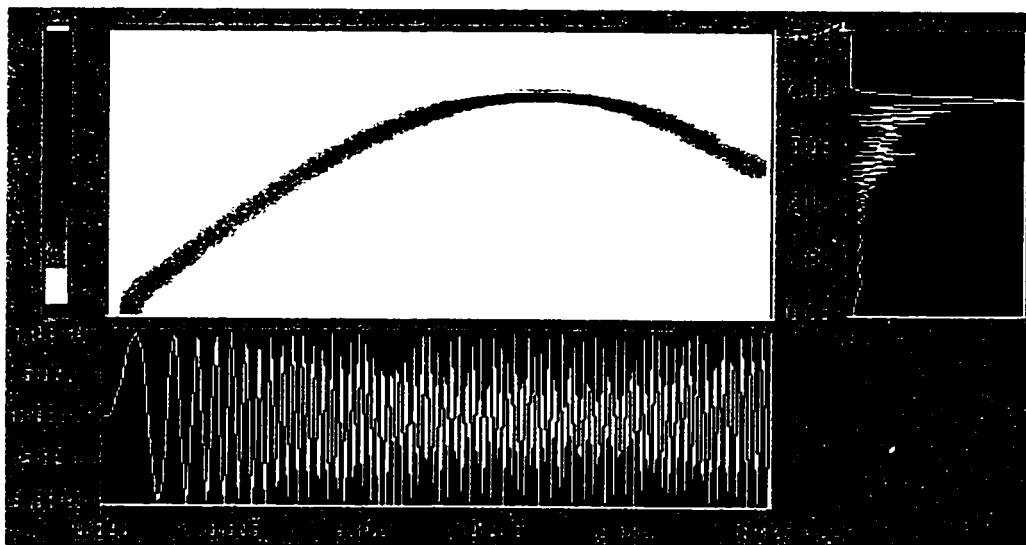


Figure 2: JTF representation of a non-linear chirp function. Below, the time representation. On the right, the frequency representation.

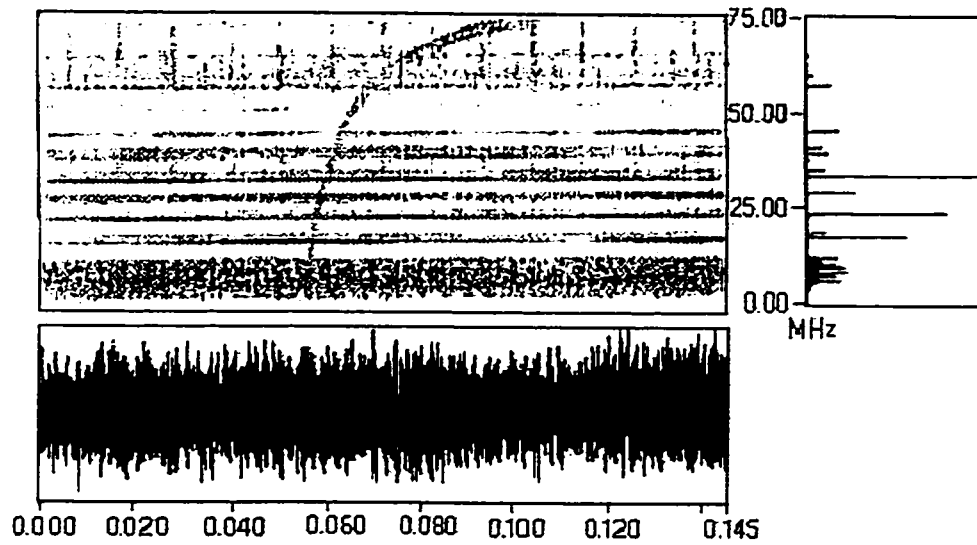


Figure 3: Ionized impulse signal (Data courtesy of Non-Proliferation & International security Division, Los Alamos National Laboratory)

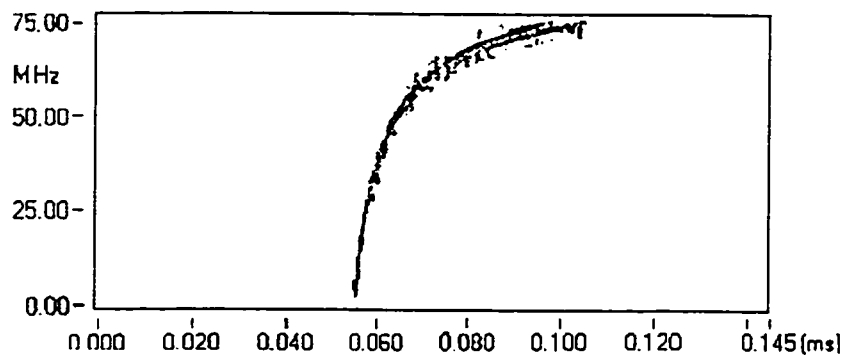


Figure 4: The ionized impulse signal masked from noisy background

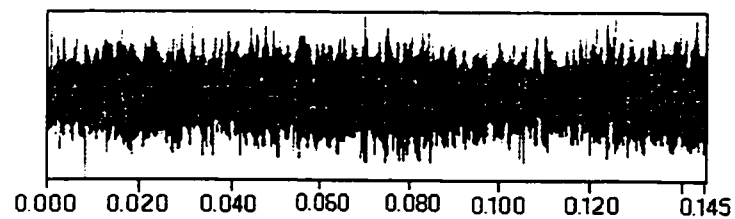


Figure 5: The ionized impulse signal before and after filtering

joint entropy. This has proven to be very useful for image compression, texture analysis, and many other applications. Also, the majority of receptive field profiles of the mammalian visual system match quite well this function.

One major problem of the JTF analysis is its high computational requirements. However, as the computing power of recent computers rapidly increases, JTF analysis is gaining increasing popularity in enormous number of applications such as speech processing, target recognition, noise removal, system identification, image processing, economical studies and many others.

JTF analysis is divided into 2 main categories: linear and nonlinear (bilinear) representations. Bilinear JTF representations are the counterpart of the power spectrum in Fourier analysis. Bilinear JTF representations, Fig. 6, include Choi-Williams distribution, cone-shape distribution, and Wigner-Ville distribution. Linear JTF representation, Fig. 7, includes wavelet, Gabor transform, and the related subject of short time Fourier transform (STFT) or windowed Fourier transform.

Bilinear JTF transforms possess the best time-frequency resolution. However, all bilinear JTF transforms share the problem of not being able to adequately get back the signal from the transformed domain. Also, they suffer from the problem of cross-term interference. In comparison, the JTF representation of the same two-chirp function by Wigner-Ville distribution is plotted in Fig. 8. The cross-term interference is very noticeable.

On the other hand, linear JTF transforms are free from the cross-term interference and the inverse transform is considerably easier to get than in the case of the bilinear transforms.

Gabor in 1946 defined the characteristics of the optimal linear JTF transform. He did

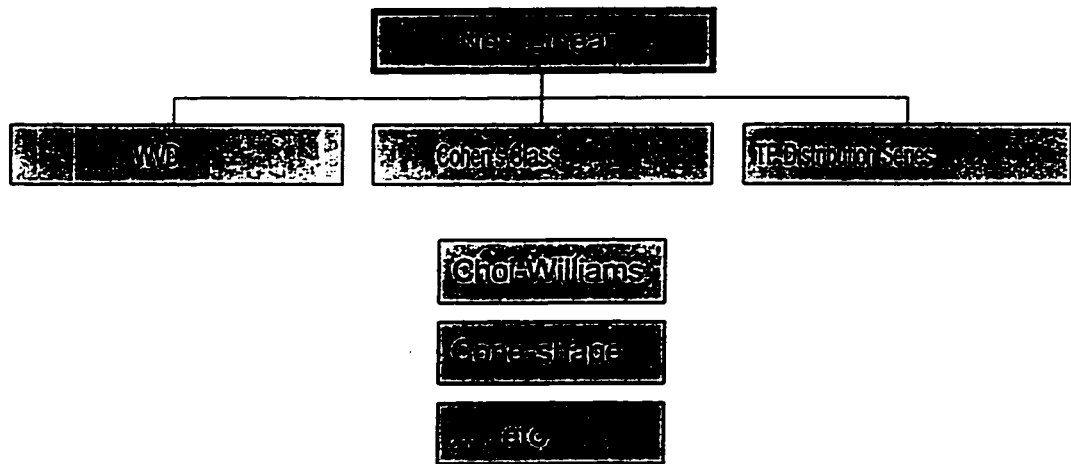


Figure 6: Types of the bilinear (non-linear) JTF representations.



Figure 7: Types of the linear JTF representations.

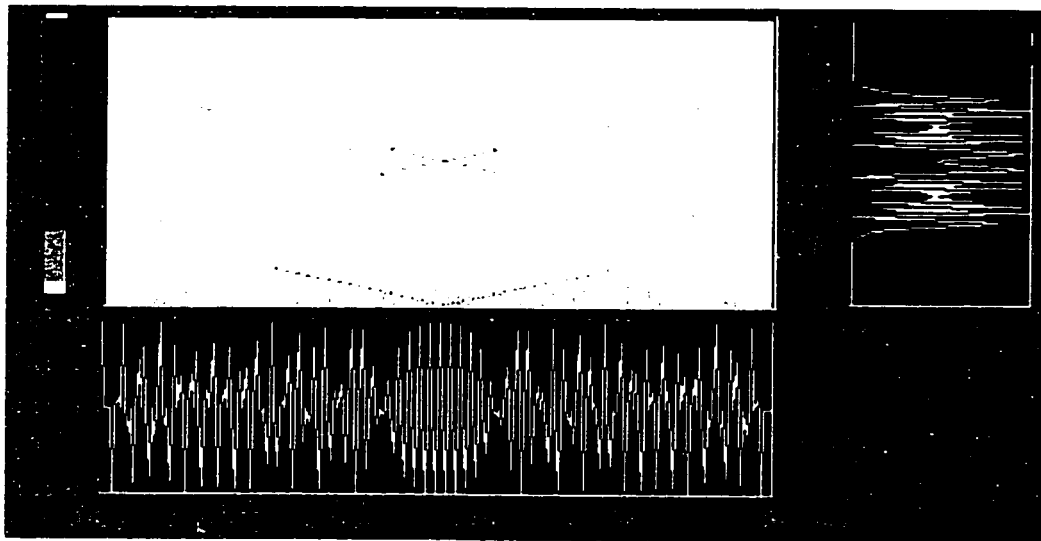


Figure 8: JTF representation of the 2-chirp function using Wigner-Ville distribution.

not, however, define a practical way to get the transform coefficients. It was no earlier than 1981 when the first practical algorithm to calculate the transform coefficients was introduced. Gabor transform is shown, however, to be unstable. This instability makes the research go to the over-sampled Gabor transform which has good stability. However, over-sampled Gabor transform has many problems like its high redundancy, its difficulty to get back the signal from the transformed domain after filtering operation¹,...etc. In 1995, the first implementation of the real Gabor expansion appeared but it is also unstable. Gabor transform belongs to the wider family of "Short Time Fourier Transform" in which Gabor transform represents the optimal among this family in the sense of resolution. The Short time Fourier transforms family is related to the wavelet (or time-scale) transforms family. In the Short time Fourier transforms, the "ruler" used to measure the signal's JTF property is made up of time-shift and frequency-modulated single prototype function. On the other hand, the "ruler" used in the wavelet transforms is obtained by the dilation and translation of a prototype function "mother wavelet". Consequently, the Short time Fourier transforms tile the JTF domain in linear fashion. However, the wavelet transforms tile the JTF domain in logarithmic (diadic) fashion.

Thus, in JTF analysis, each of these two classes of JTF transforms (linear and bilinear) has its own advantage and disadvantages which make it useful only in certain applications. Therefore, there is not a "universal" JTF transform, i.e., a JTF transform which is accepted in all branches of engineering, to be the counterpart of the Fourier transform in the time frequency domain. This limits the development of the JTF analysis.

¹ We will later discuss these problems in detail in the next chapter after introducing some mathematical background

Our objective in this thesis is to develop a JTF transform with such properties as to make it applicable to practically all branches of engineering.

In the next chapter we will give some mathematical background that enables us to define the problem and determine, mathematically, the requirements to be satisfied by a "universal" transform. In addition, we will review the available literature addressing the solution of this problem. In Chapter 3, we will present the mathematical framework which will be used throughout this thesis. This format enables us to analyze quantitatively the performance of any linear JTF transform. In particular, the localization of the biorthogonal function and the stability of the transform will be examined. In Chapters 4, 5, and 6, we will propose three different transforms which meet some or all of the optimal characteristics required for the universal JTF transform. In Chapter 7, we will demonstrate the usefulness of the developed transforms by applying it to the traditional, yet difficult, problem of noise reduction of the nuclear magnetic resonance signals. It will be shown that the proposed transform gives far better results with lower computational requirements than other transforms.

CHAPTER 2

PROBLEM DEFINITION

Gabor in 1946 defined the optimal joint time frequency transform. His pioneering work will be summarized in Section 2.2. Since Gabor did not define a practical way to get the transform coefficients, it was not earlier than 1981 for the first practical algorithm to calculate the transform coefficients to appear. Since that date, tens of methods have appeared in the literature to calculate the transform coefficients which vary, basically, in their speed. We have chosen the biorthogonal function method (which is introduced in Section 2.3) since it gives a clear insight regarding the characteristics of the transform and the problems accompanying this transform. Gabor introduced another optimal expansion for real signals which is introduced in Section 2.4 since it is a cornerstone in our work. In Section 2.1, we summarize some mathematical background which is used throughout the thesis.

2.1 Mathematical Background

We will discuss four mathematical topics needed for this research. These are: Expansion Theory, Fourier Transform, Short time Fourier Transform, and Uncertainty Principle.

2.1.1 Expansion Theory

Given any signal x from the domain G (G be of a finite or an infinite dimension in the set of integers Z), one may write x in terms of linear combination of a set of the elementary functions $\{g_n\}_{n \in Z}$ for the G – domain, i.e.,

$$x = \sum_n a_n g_n \quad (2.1)$$

i.e., the expansion coefficient a_n is the signal projection on the elementary function g_n . If the set $\{g_n\}_{n \in Z}$ is *complete* for G , that is, all signals $x \in G$ can be represented as (2.1), there will exist a *dual* set $\{\hat{g}_n\}$ such that the expansion coefficients can be computed by some regular inner product [1], such as

$$a_n \triangleq \langle x, \hat{g}_n \rangle = \sum_k x[k] \hat{g}_n^*[k] \quad (2.2)$$

If $\{g_n\}$ is complete and linearly dependent, the representation is redundant and is named the *frame*. In this case, the set $\{\hat{g}_n\}$ is, in general, not unique. If $\{g_n\}$ is complete and linearly independent, then $\{\hat{g}_n\}$ is unique and we say that $\{g_n\}$ and $\{\hat{g}_n\}$ are *biorthogonal*. That is

$$\langle g_n, \hat{g}_{n'} \rangle = \delta(n - n') \quad (2.3)$$

In this case, the set $\{g_n\}$ is called a *basis*. If, in addition

$$\langle g_n, g_{n'} \rangle = \delta(n - n') \quad (2.4)$$

i.e., $\{g_n\}$ is *orthonormal*, then $\{g_n\}$ is called an *orthonormal basis*. Under this condition, $g_n = \hat{g}_n$ and g_n is called *self-dual*, which is the case of Fourier transform, Cosine transform, Walsh-Hadamard transform, . . . etc. Note that, (2.1) is called the inverse transform and (2.2) is called the forward transform. Accordingly, \hat{g}_n is called the *analysis function* and g_n is called the *synthesis function*.

2.1.2 Fourier Transform

In 1804, Jean Baptiste Joeseph Fourier introduced the concept of presenting any time signal by a linear weighted sum of harmonically related sinusoids or complex exponents, i.e., expanding the signal into the elementary functions $\{\exp(j\omega t)\}_{\omega \in \mathbb{Z}}$. His motivation was that the functions $\{\exp(j\omega t)\}_{\omega \in \mathbb{Z}}$ are the eigenfunctions of any linear time-invariant system, i.e., if the input to any linear time-invariant system is $\exp(j\omega t)$ the output will be the same function with the same frequency but with amplitude and phase determined by the system. The transform pair is

$$S(\omega) = \int s(t) \exp(-j\omega t) dt \quad (2.5a)$$

$$s(t) = \int S(\omega) \exp(j\omega t) d\omega \quad (2.5b)$$

Since the introduction of this transform in 1804, it has become the most widely used tool to study a signal's frequency properties in all scientific and engineering fields like optics, electromagnetics, control, electronics, power systems, . . . etc.

The major disadvantage of Fourier Transform is that the elementary function $\exp(j\omega t)$

has infinite duration in time. Thus, based on the Fourier transform, it is hard to tell whether or not a signal's frequency contents evolve in time.

2.1.3 Short Time Fourier Transform

Since the Fourier transform does not explicitly reflect the signal time-varying properties, a simple way to overcome this deficiency is to multiply the signal by a short time-duration function $\gamma(t)$ before taking the Fourier transform. This function, $\gamma(t)$, is named the window function. One example of this window function is the Hamming window

$$\gamma(t) = \begin{cases} 0.54 - .46 \cos(2\pi t) & 0 < t < 1 \\ 0 & \text{otherwise} \end{cases} \quad (2.6)$$

The Short Time Fourier transform becomes

$$STFT(t, \omega) = \int s(\tau) \gamma(\tau - t) \exp(-j\omega\tau) d\tau \quad (2.7)$$

As shown in Fig. 9, the STFT operation is done as follows: First multiply the window function $\gamma(t)$ with the signal $s(t)$ and then take the Fourier transform of the product. Second, shift $\gamma(t)$ in time and repeat the same process [2]. Thus, to have a better time resolution, we choose a short duration window. But the shorter window implies a wider spectrum of $\gamma(t)$ which results in broader frequency resolution. This phenomenon is illustrated in detail in [2].

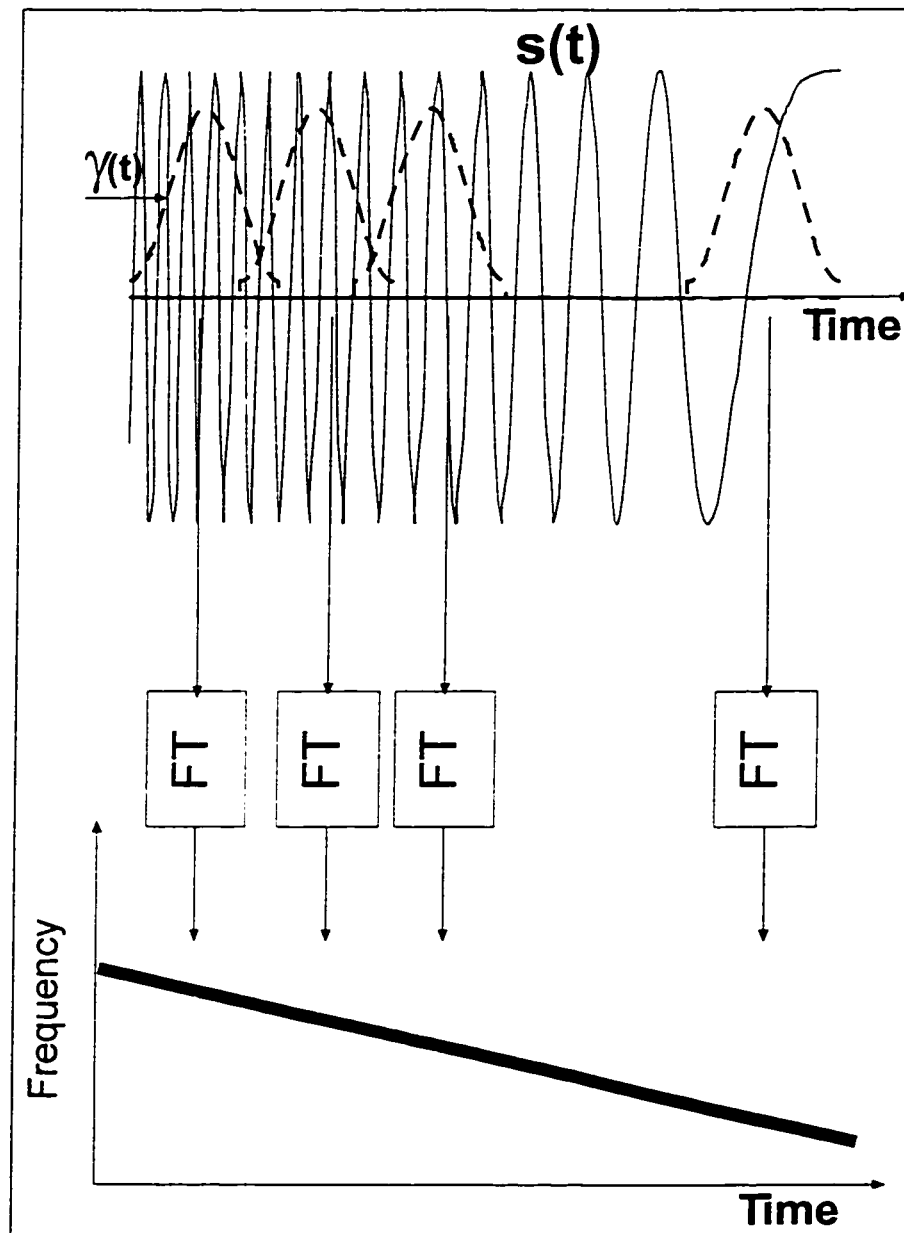


Figure 9: A linear chirp signal and its Short Time Fourier Transform.

2.1.4 Uncertainty Principle

It is known that there are some basic connections between a signal's time and frequency representations. The most important to us in our development is the relationship between a signal's time duration and frequency bandwidth. It is known that the more a signal is concentrated in the time domain, the more spread it is in the frequency domain. We will put this in mathematical terms for future usage.

The energy E contained in a signal $s(t)$ is given by

$$E = \int |s(t)|^2 dt = \frac{1}{2\pi} \int |S(\omega)|^2 d\omega \quad (2.8)$$

Then, the normalized functions $\frac{|s(t)|^2}{E}$ and $\frac{|S(\omega)|^2}{2\pi E}$ are the signal energy density in the time and frequency domains, respectively. Thus, one can use the concept of variance to measure the signal's spreading in time and frequency domains. Usually, $2\Delta_t, 2\Delta_\omega$ are defined for the time duration and frequency bandwidth respectively where Δ_t, Δ_ω are given by

$$\Delta_t^2 = \frac{1}{E} \int (t - \langle t \rangle)^2 |s(t)|^2 dt \quad (2.9a)$$

$$\Delta_\omega^2 = \frac{1}{2\pi E} \int (\omega - \langle \omega \rangle)^2 |S(\omega)|^2 d\omega \quad (2.9b)$$

where $\langle t \rangle, \langle \omega \rangle$ are the mean time and the mean frequency, respectively, and are given by

$$\langle t \rangle \triangleq \frac{1}{E} \int t |s(t)|^2 dt \quad (2.10a)$$

$$\langle \omega \rangle \triangleq \frac{1}{2\pi E} \int \omega |S(\omega)|^2 d\omega \quad (2.10b)$$

The quantities Δ_t and Δ_ω are related to each other. The uncertainty principle theory [1] states that

If $\sqrt{t}s(t) \rightarrow 0$ for $|t| \rightarrow \infty$, then

$$\Delta_t \Delta_\omega \geq \frac{1}{2} \quad (2.11)$$

The equality holds *only* when $s(t)$ is the Gaussian function, $g(t)$

$$g(t) \triangleq a \exp(-\alpha t^2) \quad (2.12)$$

In other words, the Gaussian function has the best localization property among all other functions in both time and frequency domains simultaneously. Figure 10 shows the Gaussian function which has the best localization in both time and frequency. Here, $\Delta_t = \sqrt{\frac{\pi}{2}} \frac{1}{\alpha}$ and $\Delta_\omega = \frac{1}{\sqrt{2\pi}} \alpha$, i.e., $\Delta_t \Delta_\omega = \frac{1}{2}$ which is the lower bound of the uncertainty inequality.

2.2 Gabor Expansion

In 1946, Gabor suggested representing a one dimensional signal, typically the time, in two dimensions with time and frequency as coordinates [3] which he named “the information diagram”. He pointed out that there is a certain elementary signal which occupies the smallest possible area in the information diagram. This minimal area, which reflects the inevitable trade-off between time resolution and frequency resolution, has a lower bound

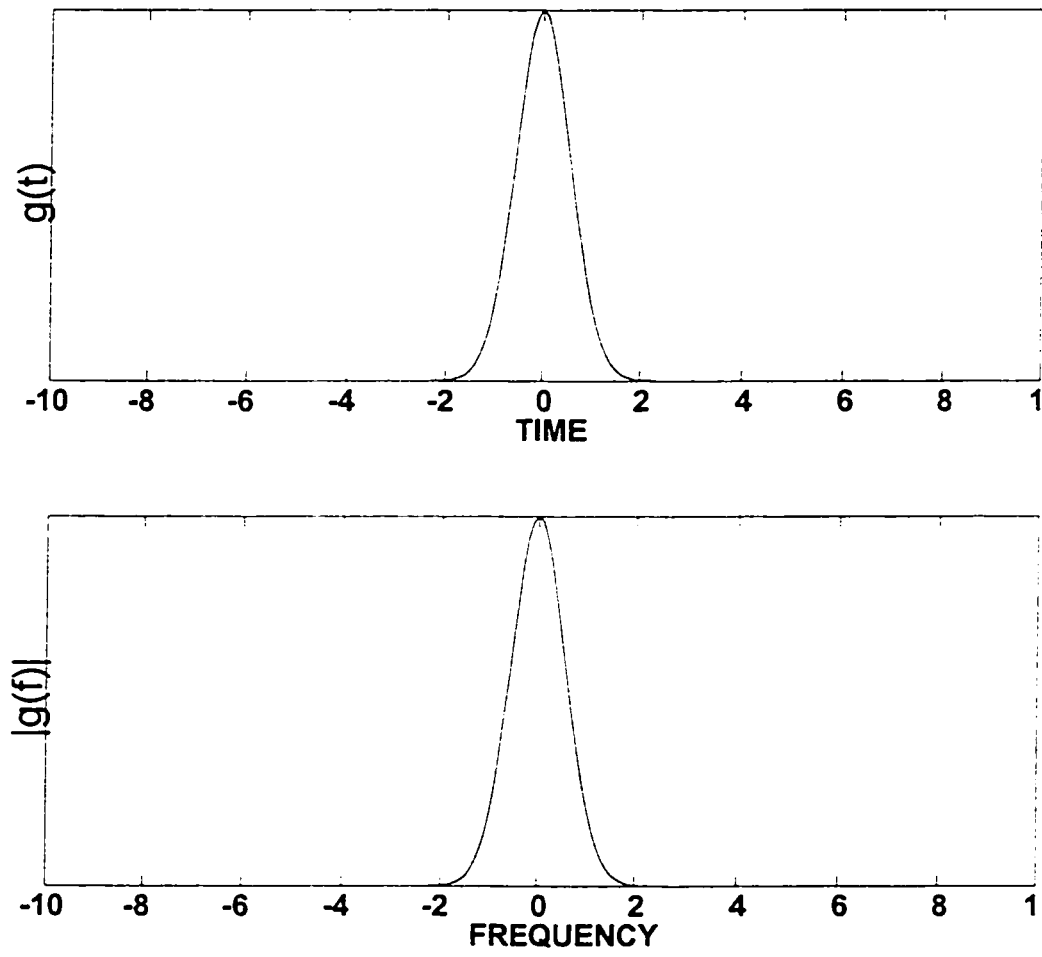


Figure 10: The Gaussian function, g , in both time and frequency domains

in their product, analogous to Heisenberg's uncertainty principle in physics. Each of these areas can be considered as conveying exactly one quantum of information. He selected the modulation product of a harmonic oscillation of any frequency with a Gaussian function to be the elementary function. He proved that this selection² is the *only* optimal elementary signal concentrated in the joint time-frequency domain according to the uncertainty principle. Namely, he expanded the signal to a time and frequency shifts of the elementary function

$$S(t) = \exp(-\alpha^2(t - t_o)^2) \exp(-j2\pi f_o t) \quad (2.13)$$

where t_o is the epoch of its peak, f_o is the frequency of the modulating oscillation and α interpreted as the sharpness of the pulse. When $\alpha = 0$, the elementary signal becomes sine wave of infinite length, i.e., we come back to the frequency domain representation. When $\alpha = \infty$, the elementary signal becomes delta function, i.e., we come back to the time domain representation. These elementary functions divide the time-frequency plane "information diagram" as shown in Fig. 11 into rectangles. Each rectangle has sides Δ_t and Δ_ω and area $\frac{1}{2}$ centering around the point (t_o, ω_o) and represents one elementary function. The expansion is

$$x(t) = \sum_{m=-\infty}^{\infty} h(t - m\Delta_t) \sum_{n=-\infty}^{\infty} a_{m,n} \exp(-2j\pi nt/\Delta_t) \quad (2.14)$$

² Although Gabor restricted himself to Gaussian window, his signal expansion holds for rather arbitrarily shaped signals.

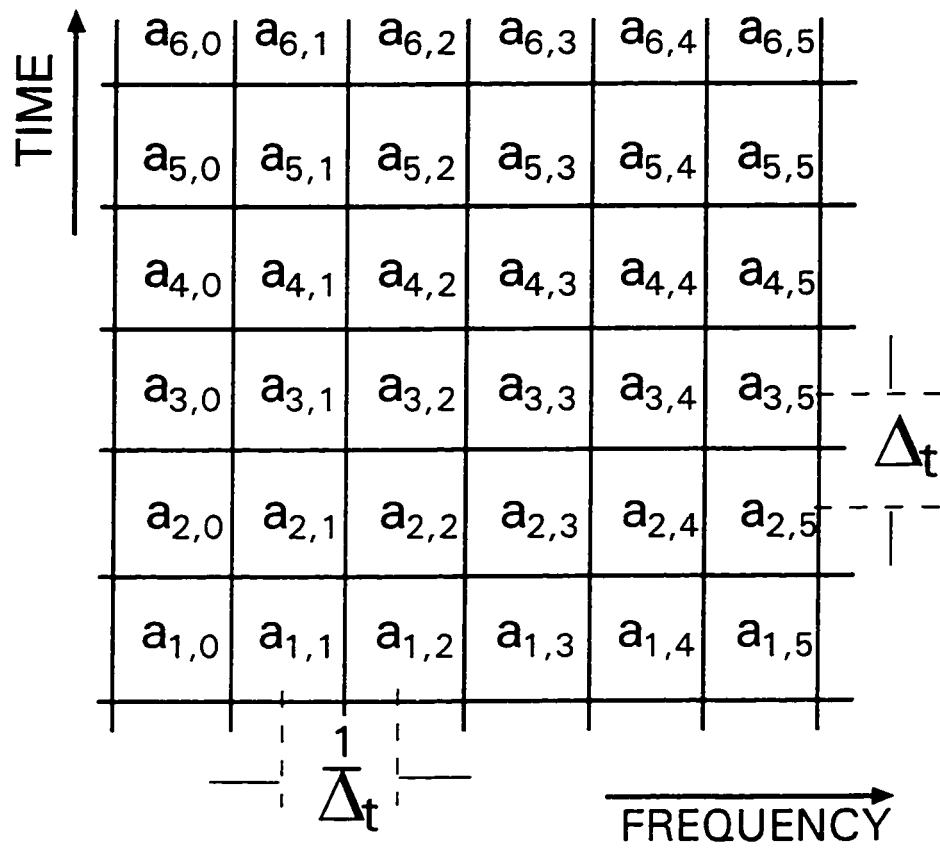


Figure 11: Expansion of arbitrary signal in complex elementary signals.

where $h(t) = \exp\left(-\frac{\pi}{2}(t/\Delta_t)^2\right)$. Unfortunately, the elementary functions are not orthogonal. Thus, there was no direct way to get the expansion coefficients $a_{m,n}$. Gabor, himself, did not publish any practical algorithms for computing the transform coefficients $a_{m,n}$. He proposed an iterative approach to compute the coefficients $a_{m,n}$ which, in general, has been found not to converge [4]. Bastiaans in 1981 was the first one to solve the problem for one-dimension signals by introducing the concept of biorthogonal function (we will discuss it in detail in Section 2.3) which relates Gabor transform with STFT [5]. This method was extended to the two-dimensional case in 1984 by Porat and Zeevi [6]. Daugman proposed a three-layer neural network for extracting the Gabor coefficients [7]. The neural networks learning process was accomplished using a least mean square (LMS) type algorithm. The convergence, however, was slow which hinders the use of the algorithm in real time applications. Teuner and Hosticka [8] presented an algorithm that computes the coefficients using the complex LMS. Ibrahim and Azimi-Sadjadi [9] suggested a significantly faster algorithm using a recursive least square type algorithm. Currently, there are several approaches to implement Gabor expansion for both continuous-time and discrete-time signals like frame theory [10, 11], filter-bank theory [12, 13], and biorthogonal function [14, 15]. We have chosen the biorthogonal function method since it gives clear insight of the characteristics of the Gabor expansion. Note that, as will be seen later, the transform coefficients $a_{m,n}$, for the critical sampling case, are unique, i.e., whatever the method is used to get the transform coefficients, the resulting coefficients are the same.

2.3 The Concept of Biorthogonal Function

According to expansion theory, discussed above, since the set of the Gabor elementary functions is complete, even though it is not orthogonal, there is a dual function $\gamma(t)$ such that the Gabor coefficients can be computed by regular inner product operation, i.e.,

$$a_{m,n} = \int \gamma^*(t - mT) \exp\left(\frac{-jnt}{\Delta_t}\right) s(t) dt \quad (2.15)$$

and since the set of Gabor elementary functions in general does not constitute an orthogonal basis, the dual function $\gamma(t)$ is not, in general, equal to $h(t)$. There are several theorems addressing the relationship between $h(t)$ and $\gamma(t)$ [10,11,14,15]. The biorthogonal function $\gamma(t)$ has to satisfy the equation

$$\sum_{m=-\infty}^{\infty} \sum_{n=0}^{\infty} \gamma_{m,n}^*(t') h_{m,n}(t) = \delta(t - t') \quad (2.16)$$

or by using the Poisson-sum formula (2.16) can be reduced to [16]

$$\int \gamma_{m,n}^*(t) h(t) = \delta(m)\delta(n) \quad (2.17)$$

where $\gamma_{m,n} = \gamma(t - m\Delta_t) \exp jn\Delta_f$. This is known as Wexler-Raz identity. It was shown [16] that the Gabor elementary functions $\{h_{m,n}(t)\}$ are linearly independent and the dual function is unique and biorthogonal to $h(t)$.

The calculation of the biorthogonal function $\gamma(t)$ in an efficient way was treated in many papers [17–19] which give us a function plotted in Fig. 12 in both time and frequency

presentations. Equation (2.15) shows that the Gabor transform is equivalent to short time Fourier transform (STFT) with the biorthogonal function used as the STFT-window. It follows from the STFT theory that to maintain time and frequency resolution, the STFT window function (i.e., biorthogonal function in our case) has to satisfy two contradictory requirements:

1. The window time duration Δ_t should be small so that the spectral characteristics are reasonably stationary over the time duration of the window, Δ_t .
2. Since multiplication with a window in time domain is equivalent to convolution in frequency domain, the frequency response of the window should be as close as possible to the impulse function to maintain frequency resolution. That is, the window frequency bandwidth Δ_f should be small which requires that the window time duration Δ_t should be large according to the uncertainty principle.

In other words, the biorthogonal function has to be also as localized as possible in both frequency and time. As seen from Fig. 12, the resulting biorthogonal function of the Gabor transform is neither localized in frequency nor in time. This leads to the conclusion that the Gabor coefficients $a_{m,n}$ do not reflect the signal behavior in the vicinity of $[(m - \frac{1}{2}) \Delta_t, (m + \frac{1}{2}) \Delta_t] \times [(n - \frac{1}{2}) \Delta_f, (n + \frac{1}{2}) \Delta_f]$, i.e., the Gabor coefficients $a_{m,n}$ fail to describe the signal's local behavior. For example, take the signal $x(t)$, Fig. 13, which consists of four intervals. Each interval has one sinusoid with different amplitude and frequency. The resulting Gabor coefficients is shown in Fig. 14. Due to the non-localization of the biorthogonal function, the coefficients do not describe the time-varying nature of the signal $x(t)$ even though it does lead to perfect reconstruction of the original signal.

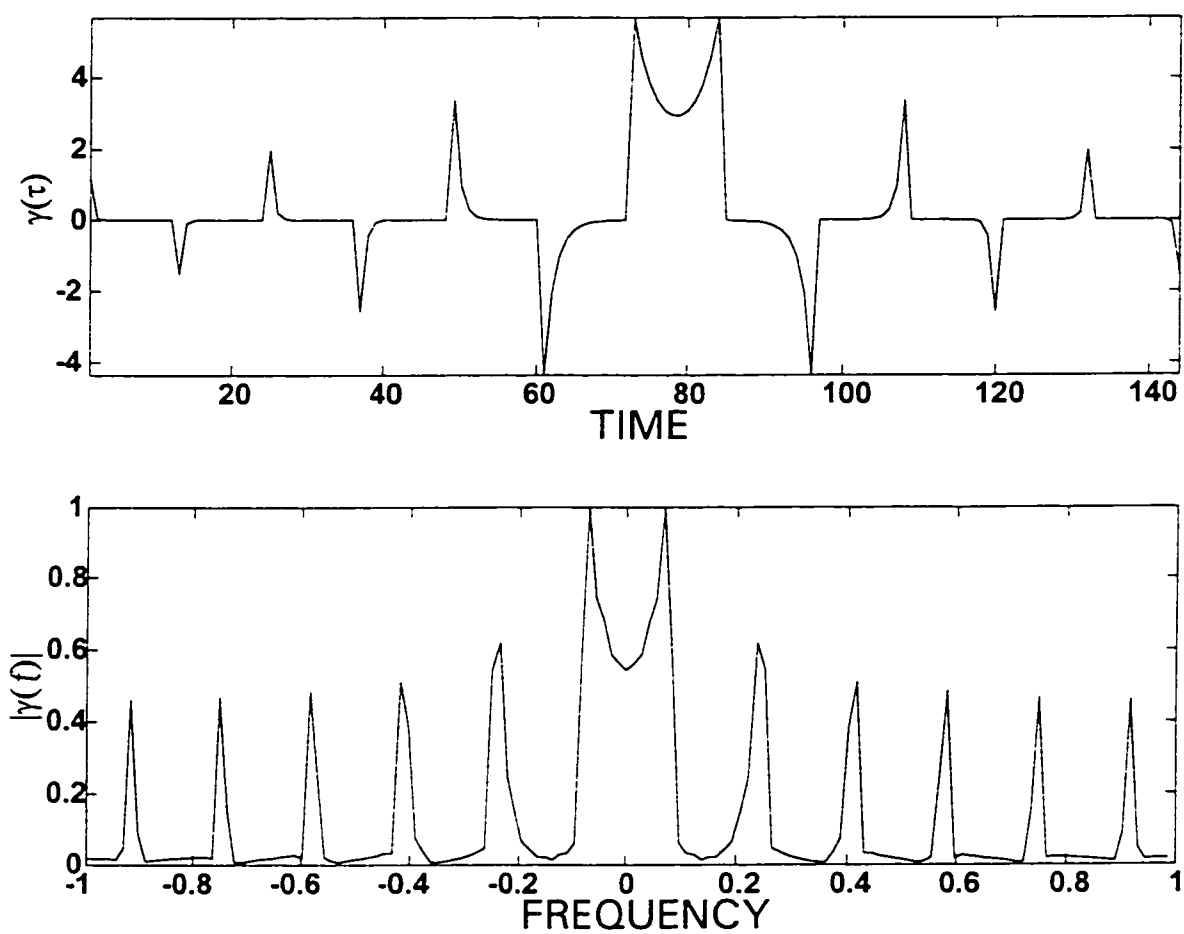


Figure 12: The biorthogonal function of the complex Gabor transform

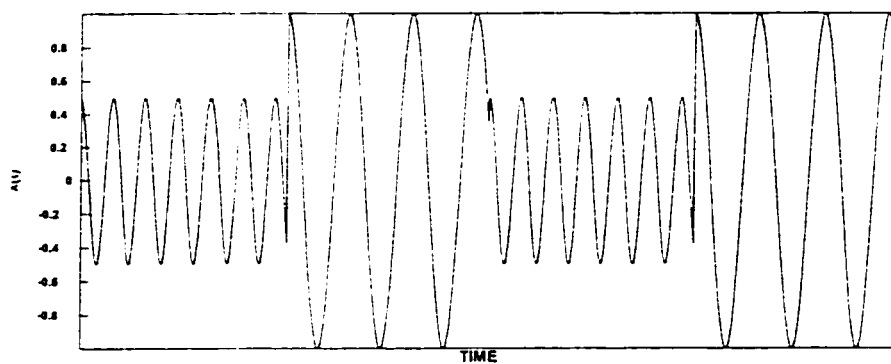


Figure 13: The time signal $x(t)$

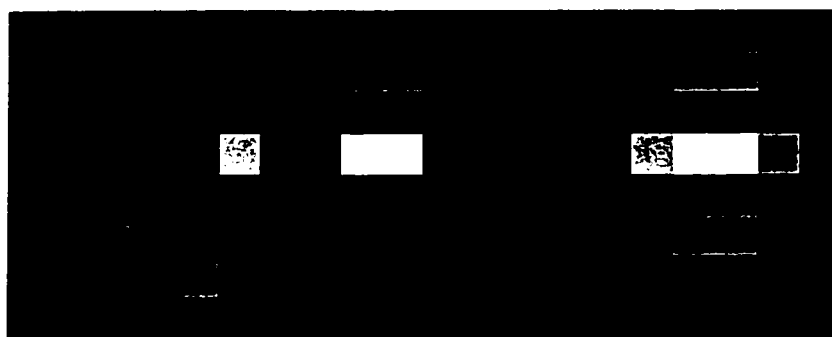


Figure 14: The Gabor coefficients of $x(t)$.

In addition, it was found that the resulting transform is unstable [20]. These two reasons prohibit the practical use of Gabor transform in many applications. In image compression, for example, a comparison between different schemes showed that the normal block DCT gives far better results than the Gabor transform [21].

To solve this problem, one has to find a better biorthogonal function. A theorem by Balian and Low [10, 22–24], however, asserts that a set of functions of type (2.14) can constitute an orthonormal basis only if either $\int |h(t)|^2 dt = \infty$ or $\int |H(f)|^2 df = \infty$. As a consequence, it is concluded that the biorthogonal function of (2.14) can not be localized in both frequency and time simultaneously.

2.4 Real Gabor Expansion

Gabor introduced another optimal, even though less famous, real expansion:

$$x(t) = \sum_{m=-\infty}^{m=\infty} h(t - m\Delta_t) \cdot \sum_{n=0}^{n=\infty} \left(a_{m,n} \cos \frac{2\pi n(t - m\Delta_t)}{\Delta_t} + b_{m,n} \sin \frac{2\pi(n + \frac{1}{2})(t - m\Delta_t)}{\Delta_t} \right) \quad (2.18)$$

in which Gabor expands the signal into two real elementary function, namely “cosine type” and “sine type” elementary signals.

$$\begin{aligned} S_c(t) &= \exp(-\alpha^2(t - t_o)^2) \cos 2\pi f_o(t - t_o) \\ S_s(t) &= \exp(-\alpha^2(t - t_o)^2) \sin 2\pi f_o(t - t_o) \end{aligned} \quad (2.19)$$

These two elementary signals are plotted in Figures 15 and 16. Thus the time-frequency plane “information diagram” is divided up as shown in Fig. 17 into cells of size $\frac{1}{2}$, measuring Δ_t in the time and $\Delta_f = \frac{1}{2\Delta_t}$ in the frequency. This expansion was observed in [20, 25] to have the nice feature of not being subject to the localization restrictions of the Balian-Low theorem, i.e., one can find a localized biorthogonal function in time and frequency domains for this expansion. Stewart *et al.* [25] proposed an implementation which leads to a localized biorthogonal function in the time domain but not in the frequency domain. This implementation will be modified in Chapter 4 to give a localized biorthogonal function in both the time and the frequency domains.

2.5 Requirements for Universal Joint Time-Frequency Transform

Now we are able to summarize the basic requirements of JTF transform as follows:

1. Concentrated analysis function in time and in frequency to have fine resolution in the JTF domain.
2. Linearity to avoid the cross-term interference and to have easy inverse transform.
3. Independent coefficients since dependant coefficients make retrieving the modified signal from the modified JTF representation quite cumbersome. In addition, dependant coefficients result in the increase of the data size. This increase in data size is unacceptable in many applications especially in applications which involve huge amount of data or when the task is to reduce the data size like data compression.

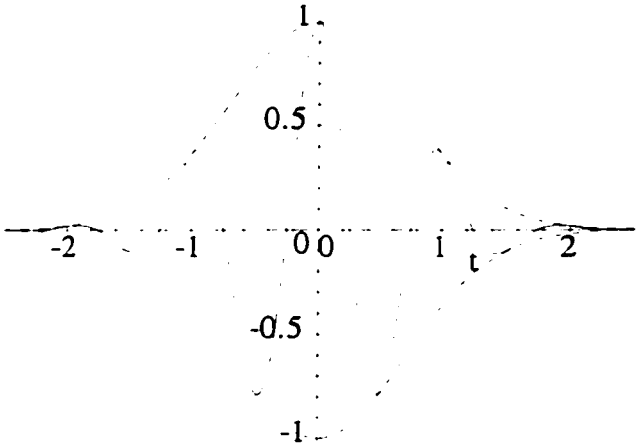


Figure 15: Cosine type elementary function

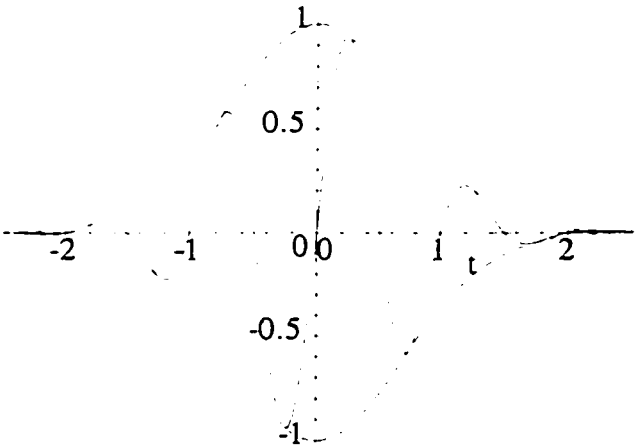


Figure 16: Sine type elementary function

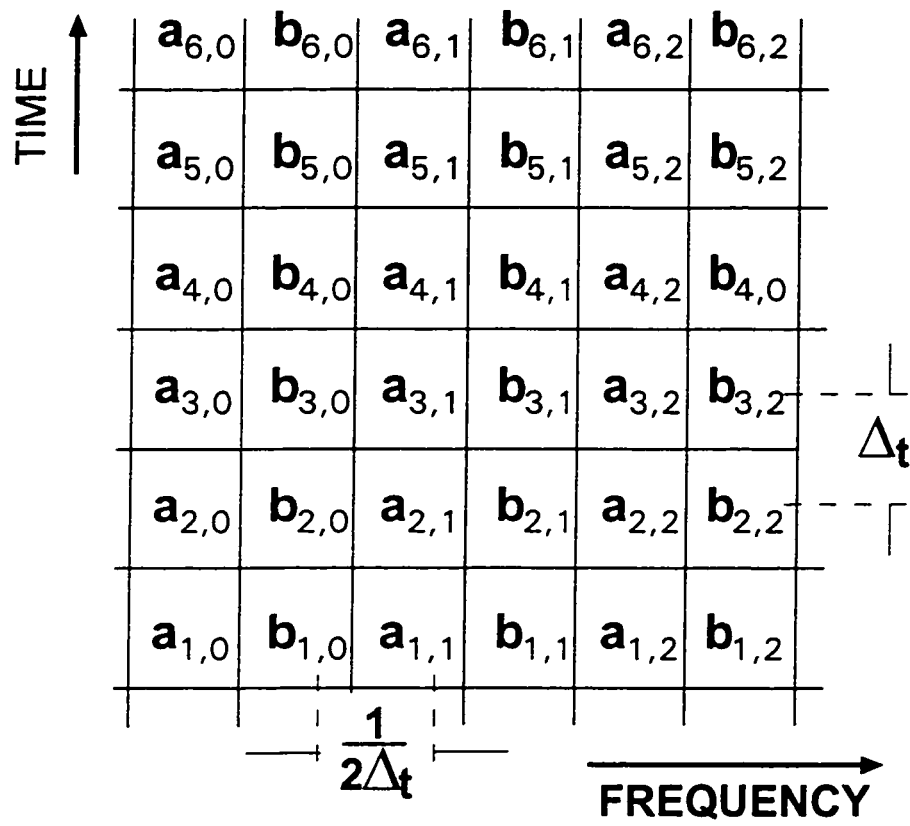


Figure 17: Expansion of a signal in cosine-type and sine-type elementary signals.

4. Concentrated dual function in time and in frequency since a non-localized biorthogonal function will make the transform unable to describe the signal's local behavior (the most important advantage of any JTF analysis).
5. Stability since instability, as will be seen in Section 3.5, makes the transform very sensitive to noise, thus limiting the use of the transform in practical applications.

In addition to the above requirements, the computation involved should be tractable.

Throughout this thesis, an independent set of the modulation product of the Gaussian window with a harmonic kernel was chosen as the elementary functions (which is the optimal elementary functions suggested by Gabor[3]). This choice ensures the **MOST Concentrated analysis function in time and in frequency** as was proved in [3]. Also, we choose to *linearly* expand time signals into an independent set composed of time and frequency shifts of this elementary function. This choice results in meeting the first three requirements³. Thus, we are left with the last two requirements, that is Stability and Concentrated dual function in time and in frequency.

These two requirements, in addition to the computational requirements, have not been met by any critically-sampled Gabor transform available in the literature. Our aim in this study is to develop a JTF transform which maintains the first three properties and satisfies, as close as possible, the last two, keeping in mind the computational requirements.

Throughout this thesis, we assume that the discrete signal $x(k)$ is of length L , M represents the number of shifts of the modulated Gaussian pulse, and N represents the number of frequency components in each shift.

³ The critical-sampled Gabor transform also meets these three requirements.

2.6 Existing Solutions

In the previous sections, we introduced the Gabor transform and showed the problems encountered with the practical implementations of the transform, mainly the non localized biorthogonal function and the instability of the resulting transform. To solve these problems, there exist in the literature two approaches: Over-sampling solution and Real Gabor transform.

2.6.1 Over-sampling Solution

To overcome these two problems, research went to over-sampling case [16,26] in which the sampling distances in time and frequency become denser than the case of the original Gabor expansion, which was named later “*critical sampling case*”. In the over-sampled Gabor transform, the dual functions are not unique. This solves the problem of non-localized dual function by choosing a dual function closest in norm to the Gaussian window. The price to be paid is high redundancy and linear dependency among the coefficients.

Let us rewrite the Gabor expansion for complex signals as

$$x(t) = \sum_{m=-\infty}^{\infty} h(t - m\alpha T) \sum_{n=-\infty}^{\infty} a_{m,n} \exp(-jn\beta\Omega t) \quad (2.20)$$

where the unit time shift αT and the unit frequency shift $\beta\Omega$ satisfy the relationships $\Omega T = 2\pi$. The linear expansion(2.20) can be complete only when $\alpha\beta \leq 1$. When $\alpha\beta = 1$, we will come back to the critical sampling case and the $a_{m,n}$ set can be interpreted as independent data, i.e., degrees of freedom of the signal. If $\alpha\beta < 1$, the set is over-complete,

which implies that the coefficients $a_{m,n}$ become dependant and can no longer be identified as degrees of freedom. Now, there are several approaches to implement over-sampling Gabor transform like frame theory [10, 11], filter-bank theory [12, 13], biorthogonal function [14, 15]. As we mentioned above, the biorthogonal function in this case is not unique. Researchers tried to find the best one closest in ℓ_2 norm to the Gaussian window. In Figs. 18 and 19, the best resulting biorthogonal function is plotted for different over-sampling ratio ($\mathcal{OVS}\mathcal{R} = 1/\alpha\beta$). As we see from the figures, the over-sampled Gabor transform gives a localized biorthogonal function in both the time domain and the frequency domain and this leads to a stable transform as we will prove in the next chapter for the discrete case. This solves the problem but at the expense of a considerable expansion of the size of the data. For example, If we have a two dimensional function (image) with size x and we apply over-sampling with $\mathcal{OVS}\mathcal{R} = 4$, the resulting transformed image will have size $16x$. This increase in data size is unacceptable in many applications especially in applications which involve huge amount of data like image processing or when the task is to reduce the data size like data compression. Also, one main disadvantage of the over-sampling Gabor transform is the linear dependence between the coefficients. This creates many problems in various applications like filtering, noise removal, . . .etc. This phenomenon will be discussed in detail in the next subsection.

2.6.1.1 Dependent Coefficients: One main difficulty in designing time-variant filters is that the modified over-sampled time-frequency representation usually has no physically existing signal that corresponds to it. Our explanation to this is as follows: In the

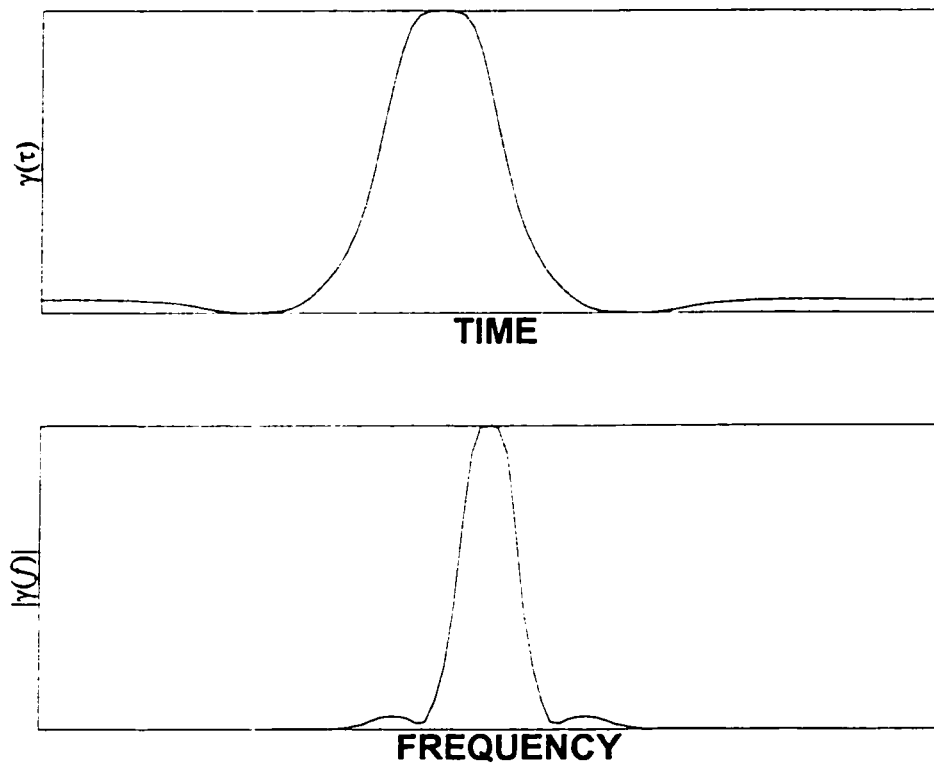


Figure 18: The biorthogonal function of the over sampling case for $OVSR = 2$.

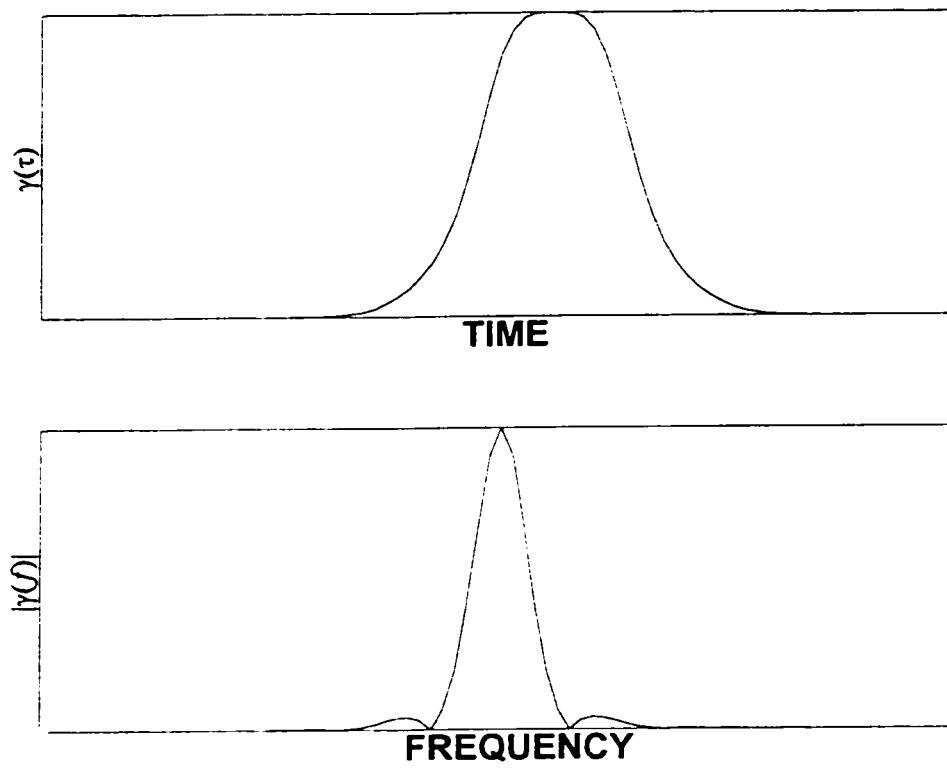


Figure 19: The biorthogonal function of the over sampling case for $OVSR = 4$.

Fourier domain, one can apply any type of filtering, like lowpass filter, Fig. 20 . This is equivalent to setting the coefficients which correspond to the high frequency to zero (the coefficients corresponding to the basis $\{e^{-j\omega t}\}_{\omega > \omega_c}$). This will have no effect on the other coefficients since they are completely independent, even orthogonal to each other in case of Fourier transform, i.e.,

$$\int \exp(-j\omega_n t) \exp(-j\omega_m t) dt = 2\pi \delta(n - m) \quad (2.21)$$

In the case of over-sampling Gabor transform, however, one does not have the freedom to set the coefficient values arbitrarily since the coefficients are dependent. This makes retrieving the modified signal from the modified over-sampled time-frequency representation quite cumbersome. The least squares error method is used in which the time-frequency representation of the estimated signal is closest, in the mean square sense, to the noise-reduced time-frequency representation [1]. In this method we need to calculate the pseudo-inverse of an $l \times l$ matrix, where l is the number of Gabor coefficients which is at least equal to the number of samples!.

Throughout this thesis we are interested in the critically-sampled JTF transforms which happen to be the most compact representation with linearly independent coefficients.

2.6.2 Real Gabor Transform

In [25], an implementation of Gabor expansion for real signal(2.18) was proposed. The implementation gives a concentrated biorthogonal function in the time domain that permits

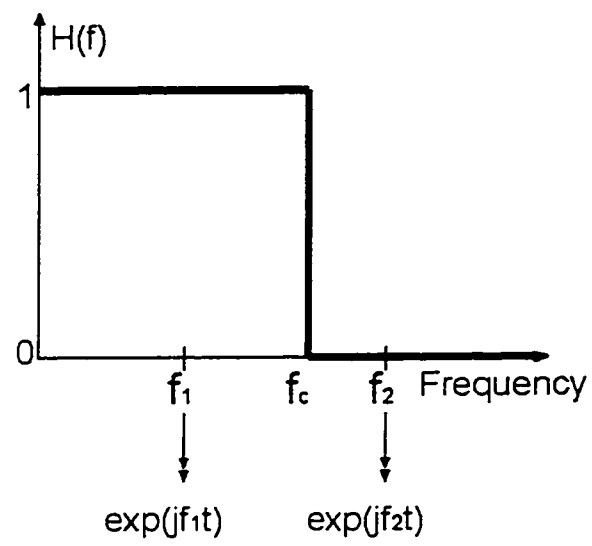


Figure 20: A low-pass filter

a truncated version of the biorthogonal function to be used in near lossless signal analysis and synthesis. This reduces the computation requirements significantly at the expense of its frequency response which is dramatically destroyed (no localization) as shown in Fig. 21. As a result, its frequency resolution is also destroyed. The authors assume that both the signal and the window are periodic which is a substantial change from the natural structure of the transform [19]. Also, as we will prove later, this transform is unstable. Below, an outline of the derivation is given which will be related to our work.

Gabor's expansion for real signals is

$$x(t) = \sum_{m=-\infty}^{m=\infty} h(t - m\Delta_t) \cdot \sum_{n=0}^{n=\infty} \left(a_{m,n} \cos \frac{2\pi n(t - m\Delta_t)}{\Delta_t} + b_{m,n} \sin \frac{2\pi(n + \frac{1}{2})(t - m\Delta_t)}{\Delta_t} \right) \quad (2.22)$$

Centering the Gaussian function on the analysis windows and reformulating (2.22) using only cosine functions:

$$x(t) = \sum_{m=-\infty}^{m=\infty} h(t - m\Delta_t - \Delta_t/2) \sum_{n=0}^{n=\infty} a_{m,n} \cos \frac{\pi n t}{\Delta_t} \quad (2.23)$$

Sampling this continuous-time formulation, we obtain a windowed discrete cosine transform (DCT), specifically

$$x(k) = \sum_{m=0}^{M-1} h(k - mN) \left(a_{m,0} \sqrt{\frac{1}{N}} + \sum_{n=1}^{N-1} a_{m,n} \sqrt{\frac{2}{N}} \cos \frac{(2k+1)\pi n}{2N} \right) \quad (2.24)$$

where $a_{m,n}$ is the expansion coefficients and $h(k)$ is the discrete periodic version of the

window placed at the center of the specified interval, i.e.,

$$h(k) \triangleq \left(\sqrt{\frac{2}{N}} \right)^{\frac{1}{2}} \exp \left(-\pi \left(\frac{k - (N-1)/2}{N} \right)^2 \right) \quad (2.25)$$

$$-\frac{MN}{2} + \frac{N-1}{2} \leq k \leq \frac{MN}{2} + \frac{N-1}{2}$$

Putting (2.24) in matrix notation,

$$\begin{bmatrix} H_0(CJ^0)^T & H_{M-1}(CJ^0)^T & \cdots & H_1(CJ^0)^T \\ H_1(CJ^1)^T & H_0(CJ^1)^T & \cdots & H_2(CJ^1)^T \\ \vdots & \vdots & \ddots & \vdots \\ H_{M-1}(CJ^{M-1})^T & H_{M-2}(CJ^{M-1})^T & \cdots & H_0(CJ^{M-1})^T \end{bmatrix} \begin{bmatrix} \mathbf{a}_1 \\ \mathbf{a}_2 \\ \vdots \\ \mathbf{a}_M \end{bmatrix} = \begin{bmatrix} \mathbf{x}_1 \\ \mathbf{x}_2 \\ \vdots \\ \mathbf{x}_M \end{bmatrix} \quad (2.26)$$

where $\mathbf{a}_m = (a_{m,1}, a_{m,2}, \dots, a_{m,N})^T$ and the matrix $C = [c_{n,k}]_{N \times N}$ with $c_{n,k}$ given by

$$c_{n,k} = \alpha \cos \frac{(2k+1)\pi n}{2N} \quad n, k = 0, \dots, N-1$$

where

$$\alpha = \begin{cases} \sqrt{\frac{1}{N}} & \text{for } n = 0 \\ \sqrt{\frac{2}{N}} & \text{for } n = 1, \dots, N-1 \end{cases}$$

J is the $N \times N$ row exchange matrix defined in (A-1),

$$\mathbf{x}_{m+1} = (x(mN+1), x(mN+2), \dots, x(mN+N))^T$$

and

$$H_m \triangleq \begin{bmatrix} h(mN) & 0 & \cdots & 0 \\ 0 & h(mN+1) & \cdots & 0 \\ \vdots & \vdots & \ddots & \vdots \\ 0 & 0 & \cdots & h(mN+N-1) \end{bmatrix} \quad (2.27)$$

Assuming that M is even, since $J^{2k} = I$, $J^{2k+1} = J$, and $J^T = J$, (2.26) reduces to

$$\begin{bmatrix} H_0 & H_{M-1}J & \cdots & H_1J \\ H_1J & H_0 & \cdots & H_2 \\ \vdots & \vdots & \ddots & \vdots \\ H_{M-1}J & H_{M-2} & \cdots & H_0 \end{bmatrix} \begin{bmatrix} C^T & 0 & \cdots & 0 \\ 0 & JC^T & \cdots & 0 \\ \vdots & \vdots & \ddots & \vdots \\ 0 & 0 & \cdots & JC^T \end{bmatrix} \mathbf{a} = \mathbf{x} \quad (2.28)$$

or

$$\mathbf{x} = \mathbf{H} \mathbf{C}^T \mathbf{a} \quad (2.29)$$

Since \mathbf{C}^T is orthogonal, the inverse of the above equation is

$$\mathbf{a} = \mathbf{C} \mathbf{H}^{-1} \mathbf{x}$$

The inverse matrix \mathbf{H}^{-1} is the block circulant matrix

$$\begin{bmatrix} \Gamma_0 & J\Gamma_1 & \cdots & J\Gamma_{M-1} \\ J\Gamma_{M-1} & \Gamma_0 & \cdots & \Gamma_{M-2} \\ \vdots & \vdots & \ddots & \vdots \\ J\Gamma_1 & \Gamma_2 & \cdots & \Gamma_0 \end{bmatrix} \quad (2.30)$$

where

$$\Gamma_m = \begin{bmatrix} \gamma(mN) & 0 & \cdots & 0 \\ 0 & \gamma(mN+1) & \cdots & 0 \\ \vdots & \vdots & \ddots & \vdots \\ 0 & 0 & \cdots & \gamma(mN+N-1) \end{bmatrix} \quad (2.31)$$

and $\gamma(k)$ comprises the biorthogonal function. For Gaussian window, the resulting biorthogonal function is plotted in Fig. 21. This figure shows a concentrated biorthogonal function in the time domain that permits a truncated version of the biorthogonal function to be used in near lossless signal analysis and synthesis, while its frequency response, as shown in the figure, was dramatically destroyed (no localization). As a result, its frequency resolution is also destroyed. This is one reason which illustrates our findings of the bad results when using this algorithm in image compression. This will be put in mathematical terms in Chapter 3.

In the following chapters, we will give our series of transforms which have better properties than the ones discussed here. As a start, we will put, in the next chapter, the available Gabor transforms in a unified matrix formulation which will be used in the subsequent development.

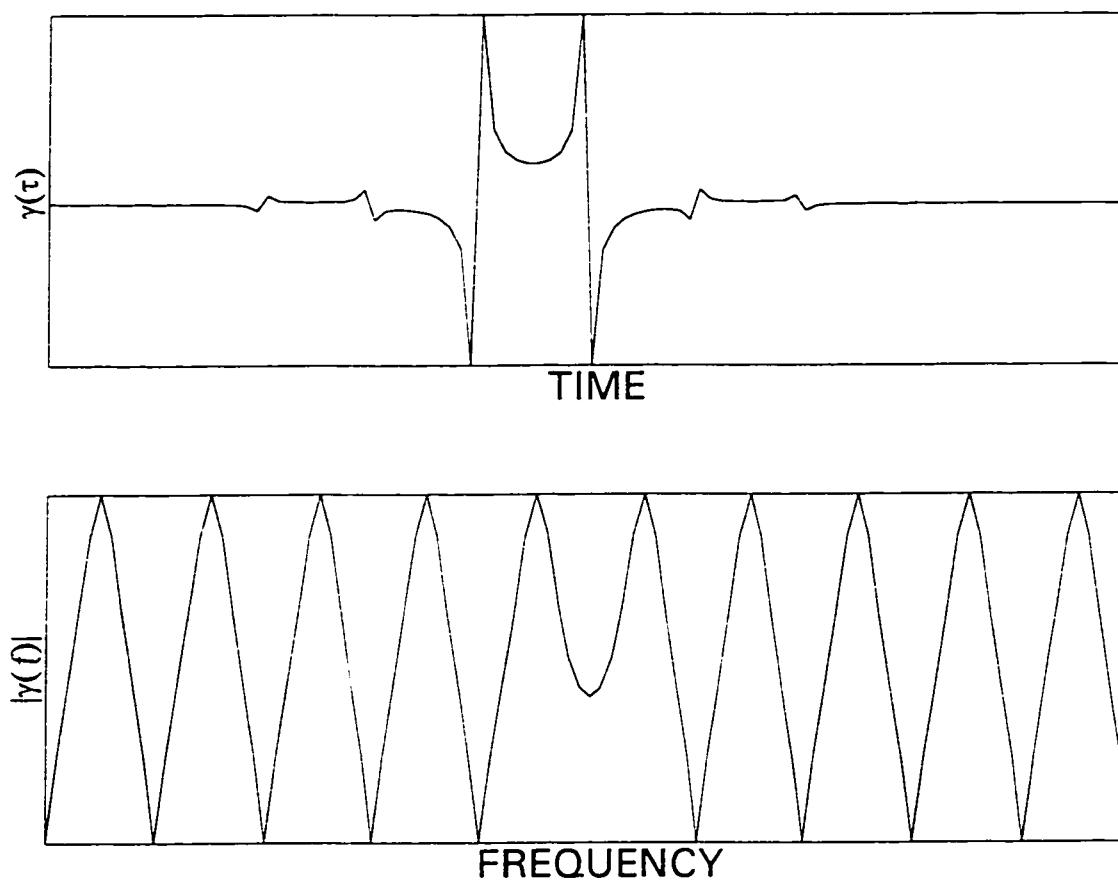


Figure 21: The biorthogonal function of the real Gabor Transform.

CHAPTER 3

MATRIX FORM AND STABILITY OF DISCRETE GABOR TRANSFORMS

In this chapter, the *discrete* aperiodic real Gabor transform will be developed. In addition, the *discrete* version of existing Gabor transforms in the literature will be presented in a unified matrix form. This form enables us to analyze quantitatively the performance of these implementations . In particular, the biorthogonal function and the stability of the transform will be examined.

3.1 Introduction

Since the signals encountered in most applications nowadays are discrete-time, it is necessary to extend the Gabor transforms to the discrete case. Discretization in time is done by either truncating the time signal to compact support region and sample it at a rate capturing their significant behavior (this is called aperiodic sampling) or by periodize the compact support signal before sampling (this is called periodic sampling). Note that sampling the

time variable leads to periodicity in the frequency domain and sampling the frequency variable leads to periodicity in the time domain. Thus, the discrete-time and discrete-frequency Gabor transform coefficients are periodic in both time and frequency. As a consequence, the Gabor transform of any signal is reduced to a linear mapping that relates the samples of the time signal to a periodic $N \times M$ matrix. where M and N are the number of time and frequency cells respectively.

In Section 3.2, the discrete version of the existing Gabor transform implementations in the literature are put in a form that enables us to analyze the performance of these implementations quantitatively. As we have seen in the previous chapters, the two main problems of any linear critically-sampled Gabor transform implementation are the non-localized biorthogonal function and the stability of the transform. These will be tested in Section 3.4 and Section 3.6. In Section 3.3, the discrete *aperiodic* real Gabor transform will be developed which will be used in the next chapter.

In Section 3.5, a precise measure of the stability of any linear *discrete* transform is defined. In Section 3.6, this definition will be applied to the various Gabor transform implementations to show their stability characteristics. We would like to stress the fact that the stability is tested here in the discrete case (NOT in the continuous case as is the case in the current literature).

3.2 Matrix Form of Discrete Gabor Transforms

For the discrete case, we assume that the discrete signal $x(k)$ is of length L , the number

of shifts of the modulated Gaussian pulse is M , and the number of frequency components in each shift is N . Define \bar{N} as L/M . There are many implementations of the Gabor transform in the literature. There are critical-sampling (the original transform) and over-sampling cases. For critical sampling case $N = \bar{N}$ while for over sampling case $N \geq \bar{N}$. The ratio N/\bar{N} represents the over-sampling rate ($\mathcal{OVS\mathcal{R}}$). There are periodic and aperiodic implementations for both equations (2.14) and (2.18). All of the above-mentioned cases could be put in the matrix form

$$\mathbf{x} = \mathbf{H} \mathbf{E}^T \mathbf{a} \quad (\text{synthesis equation}) \quad (3.1)$$

where \mathbf{a} is a vectorized form of the expansion coefficients $a_{m,n}$ defined by

$$\mathbf{a} \triangleq [\mathbf{a}_0^T, \mathbf{a}_1^T, \dots, \mathbf{a}_{M-1}^T]^T \quad (3.2)$$

with

$$\mathbf{a}_m \triangleq [a_{m,0}, a_{m,1}, \dots, a_{m,N-1}]^T \quad (3.3)$$

and \mathbf{x} is a vector containing the discrete signal of length L defined by

$$\mathbf{x} \triangleq [\mathbf{x}_0^T, \mathbf{x}_1^T, \dots, \mathbf{x}_{M-1}^T]^T \quad (3.4)$$

with

$$\mathbf{x}_m \triangleq [x(m\bar{N}), x(m\bar{N} + 1), \dots, x(m\bar{N} + \bar{N} - 1)]^T \quad (3.5)$$

The matrix \mathbf{H} is $M\tilde{N} \times MN$ matrix which provides the desired windowing effect, i.e., localization in the time domain of the elementary function. In all cases, \mathbf{H} is block matrix with $N \times N$ diagonal blocks H_m or anti-diagonal blocks \tilde{H}_m defined by

$$\begin{aligned} H_m &= \begin{bmatrix} h(mN) & & & \\ & h(mN+1) & & \\ & & \ddots & \\ & & & h(mN+N-1) \end{bmatrix} \\ &\triangleq \text{diag}(h(mN), h(mN+1), \dots, h(mN+N-1)) \end{aligned} \quad (3.6)$$

and

$$\begin{aligned} \tilde{H}_m &= \begin{bmatrix} & & & h(mN) \\ & & h(mN+1) & \\ & & & \\ h(mN+N-1) & & & \end{bmatrix} \\ &\triangleq H_m J \end{aligned} \quad (3.7)$$

where J is the $N \times N$ row exchange matrix defined in (A-1) and $h(k)$ is the discrete Gaussian function, or any other chosen function, centered on the analysis window, i.e., $h(k) \triangleq h(t)|_{t=k-\frac{N-1}{2}}$. For Gaussian function, $h(k)$ is given by

$$h(k) \triangleq \sqrt{\frac{2}{\sigma}} \exp\left(-\frac{\pi}{2\sigma^2} (k - (N-1)/2)^2\right) \quad (3.8)$$

where σ is the rms pulse-width and is usually chosen to be equal N .

The matrix \mathbf{E}^T is an $MN \times MN$ block-diagonal matrix with $N \times N$ orthogonal block. Each block is N -point discrete Fourier-Related transform. \mathbf{E}^T represents the linear transformation, i.e., localization in the frequency domain of the elementary function. In all cases,

\mathbf{E}^T is orthogonal, i.e., $(\mathbf{E}^T)^{-1} = \mathbf{E}$. Thus the inverse of the synthesis equation (3.1) is

$$\mathbf{a} = \mathbf{E} \mathbf{H}^{-1} \mathbf{x} \quad (\text{analysis equation}) \quad (3.9)$$

It is easy to verify that the matrix \mathbf{H}^{-1} is $MN \times M\tilde{N}$ block matrix with $N \times N$ diagonal or anti-diagonal blocks. The elements of \mathbf{H}^{-1} comprise the resulting discrete biorthogonal function which is required to be concentrated in both time and frequency.

Both \mathbf{H} and \mathbf{E}^T are different for different cases. For critical-sampling case ($\tilde{N} = N$), \mathbf{H} is a square matrix which is either block-circulant (for periodic implementations) or block-Toeplitz matrix (for aperiodic implementations), i.e.,

$$\mathbf{H} \triangleq \begin{cases} \begin{pmatrix} H_0 & H_{M-1} & \cdots & H_1 \\ H_1 & H_0 & \cdots & H_2 \\ \vdots & \vdots & \ddots & \vdots \\ H_{M-1} & H_{M-2} & \cdots & H_0 \end{pmatrix} & \text{block-circulant} \\ \begin{pmatrix} H_0 & H_{-1} & \cdots & H_{-M+1} \\ H_1 & H_0 & \cdots & H_{-M+2} \\ \vdots & \vdots & \ddots & \vdots \\ H_{M-1} & H_{M-2} & \cdots & H_0 \end{pmatrix} & \text{block-Toeplitz} \end{cases}$$

For the over-sampling case ($N \geq \tilde{N}$), however, \mathbf{H} is a rectangular matrix. Thus, \mathbf{H}^{-1} represents the Pseudo (right) inverse of \mathbf{H} .

The details of these implementations are in Appendix C. For the complex Gabor transform (2.14), the discrete periodic version (Appendix C.1) was put in matrix form by Balart [27]. This was extended to the discrete aperiodic case (Appendix C.2) in [19, 28]. In addition, the discrete over-sampling version (Appendix D) was put in matrix form in [29].

For the real Gabor transform (2.18), the discrete periodic version (Appendix C.3) was

put in matrix form by [25]. In the next section, we will extend this to the general discrete aperiodic case which will be used in the next chapter.

3.3 Aperiodic Real Gabor Transform

According to [19], for the Gabor transform, the assumption of periodicity is a more radical assumption than for the Fourier transform. This is because it involves a substantial change from the natural structure of the transform. Here, we do not assume the periodicity of the window nor the signal. The signal $x(t)$ is assumed to have finite duration T . The analysis window function is assumed to have a duration of at least $2T$.

Starting by the Gabor's expansion for real signals

$$x(t) = \sum_{m=-\infty}^{m=\infty} h(t - m\Delta_t) \cdot \sum_{n=0}^{n=\infty} \left(a1_{m,n} \cos \frac{2\pi n(t - m\Delta_t)}{\Delta_t} + a2_{m,n} \sin \frac{2\pi(n + \frac{1}{2})(t - m\Delta_t)}{\Delta_t} \right) \quad (3.10)$$

Centering the Gaussian function on the analysis windows and reformulate the above equation using only cosine functions

$$x(t) = \sum_{m=-\infty}^{\infty} h(t - m\Delta_t - \frac{\Delta_t}{2}) \cdot \sum_{n=0}^{\infty} \left((-1)^n a1_{m,n} \cos \frac{2\pi nt}{\Delta_t} + (-1)^{n+1} a2_{m,n} \cos \frac{2\pi(n + \frac{1}{2})t}{\Delta_t} \right)$$

which can be written as

$$x(t) = \sum_{m=-\infty}^{m=\infty} h(t - m\Delta_t - \frac{\Delta_t}{2}) \sum_{n=0}^{n=\infty} a_{m,n} \cos \frac{\pi n t}{\Delta_t} \quad (3.11)$$

where the plus and minus signs are absorbed in the coefficient values $a_{m,n}$. Sampling this continuous-time form, a windowed discrete cosine transform (DCT) is obtained, specifically

$$x(k) = \sum_{m=0}^{M-1} h(k - mN) \sum_{n=0}^{N-1} a_{m,n} \alpha \cos \frac{(2k+1)\pi n}{2N} \quad (3.12)$$

where $a_{m,n}$ is the expansion coefficients, $h(k)$ is the discrete version of the window function centered at the center of the specified interval, and α is defined as

$$\alpha = \begin{cases} \sqrt{\frac{1}{N}} & \text{for } n = 0 \\ \sqrt{\frac{2}{N}} & \text{for } n = 1, \dots, N-1 \end{cases} \quad (3.13)$$

Putting (3.12) in matrix notation,

$$\begin{bmatrix} H_0(CJ^0)^T & H_{-1}(CJ^0)^T & \cdots & H_{-M+1}(CJ^0)^T \\ H_1(CJ^1)^T & H_0(CJ^1)^T & \cdots & H_{-M+2}(CJ^1)^T \\ \vdots & \vdots & \ddots & \vdots \\ H_{M-1}(CJ^{M-1})^T & H_{M-2}(CJ^{M-1})^T & \cdots & H_0(CJ^{M-1})^T \end{bmatrix} \begin{bmatrix} \mathbf{a}_1 \\ \mathbf{a}_2 \\ \vdots \\ \mathbf{a}_M \end{bmatrix} = \begin{bmatrix} \mathbf{x}_1 \\ \mathbf{x}_2 \\ \vdots \\ \mathbf{x}_M \end{bmatrix} \quad (3.14)$$

where H_m , \mathbf{a}_m , and \mathbf{x}_m as defined in (3.6), (3.3), and (3.5), respectively. The matrix $C = [c_{n,k}]_{N \times N}$ is the N -point Discrete Cosine Transform matrix with $c_{n,k}$ given by

$$c_{n,k} = \alpha \cos \frac{(2k+1)\pi n}{2N} \quad n, k = 0, \dots, N-1 \quad (3.15)$$

Noting that $J^{2k} = I$, $J^{2k+1} = J$, and $J^T = J$, (3.14) reduces to

$$\begin{bmatrix} H_0 & H_{-1}J & \cdots & H_{-M+1}J \\ H_1J & H_0 & \cdots & H_{-M+2} \\ \vdots & \vdots & \ddots & \vdots \\ H_{M-1}J & H_{M-2} & \cdots & H_0 \end{bmatrix} \begin{bmatrix} C^T & 0 & \cdots & 0 \\ 0 & JC^T & \cdots & 0 \\ \vdots & \vdots & \ddots & \vdots \\ 0 & 0 & \cdots & JC^T \end{bmatrix} \mathbf{x} = \mathbf{x} \quad (3.16)$$

or

$$\mathbf{x} = \mathbf{H} \mathbf{E}^T \mathbf{a} \quad (3.17)$$

where

$$\mathbf{H} \triangleq \begin{pmatrix} H_0 & H_{-1}J & \cdots & H_{-M+1}J \\ H_1J & H_0 & \cdots & H_{-M+2} \\ \vdots & \vdots & \ddots & \vdots \\ H_{M-1}J & H_{M-2} & \cdots & H_0 \end{pmatrix} \quad (3.18)$$

and

$$\mathbf{E}^T = \begin{bmatrix} C^T & 0 & \cdots & 0 \\ 0 & JC^T & \cdots & 0 \\ \vdots & \vdots & \ddots & \vdots \\ 0 & 0 & \cdots & JC^T \end{bmatrix}$$

The inverse of equation (3.17) is

$$\mathbf{a} = \mathbf{E} \mathbf{H}^{-1} \mathbf{x} \quad (3.19)$$

Since the matrix \mathbf{H} is block-Toeplitz matrix, its inverse \mathbf{H}^{-1} is not, in general, block-

Toeplitz matrix. Thus, \mathbf{H}^{-1} is defined by

$$\mathbf{H}^{-1} \triangleq \mathbf{\Gamma} = \begin{bmatrix} \Gamma_0^{(0)} & J\Gamma_1^{(0)} & \cdots & J\Gamma_{M-1}^{(0)} \\ J\Gamma_{-1}^{(1)} & \Gamma_0^{(1)} & \cdots & \Gamma_{M-2}^{(1)} \\ \vdots & \vdots & \ddots & \vdots \\ J\Gamma_{-M+1}^{(M-1)} & \Gamma_{-M+2}^{(M-1)} & \cdots & \Gamma_0^{(M-1)} \end{bmatrix} \quad (3.20)$$

where $\Gamma_l^{(m)}$ is given by

$$\Gamma_l^{(m)} = \begin{bmatrix} \gamma_m(lN) & 0 & \cdots & 0 \\ 0 & \gamma_m(lN + 1) & \cdots & 0 \\ \vdots & \vdots & \ddots & \vdots \\ 0 & 0 & \cdots & \gamma_m(lN + N - 1) \end{bmatrix} \quad (3.21)$$

and $\gamma_m(k)$ comprises the biorthogonal function for the m time-shift. This means that, unlike the periodic case, the biorthogonal function is different for every time-shift and not just a time-shifted version of the same function. However, for strong-decaying analysis function (as the case of the Gaussian window), this implementation leads to almost the same biorthogonal function as the periodic case except at the two ends (i.e., $m = 0$ or $m = M - 1$). In Figures 22 and 23, the resulting biorthogonal function $\gamma_m(k)$ is plotted for $M = N = 8$ and $m = 0, 1, \dots, 7$. For comparison with the periodic case, the aperiodic and the periodic cases for $m = 0$ are plotted in the Fig. 24.

3.4 The Biorthogonal Function of Discrete Gabor Transforms

For the critically-sampled GT's, the resulting discrete biorthogonal functions is shown

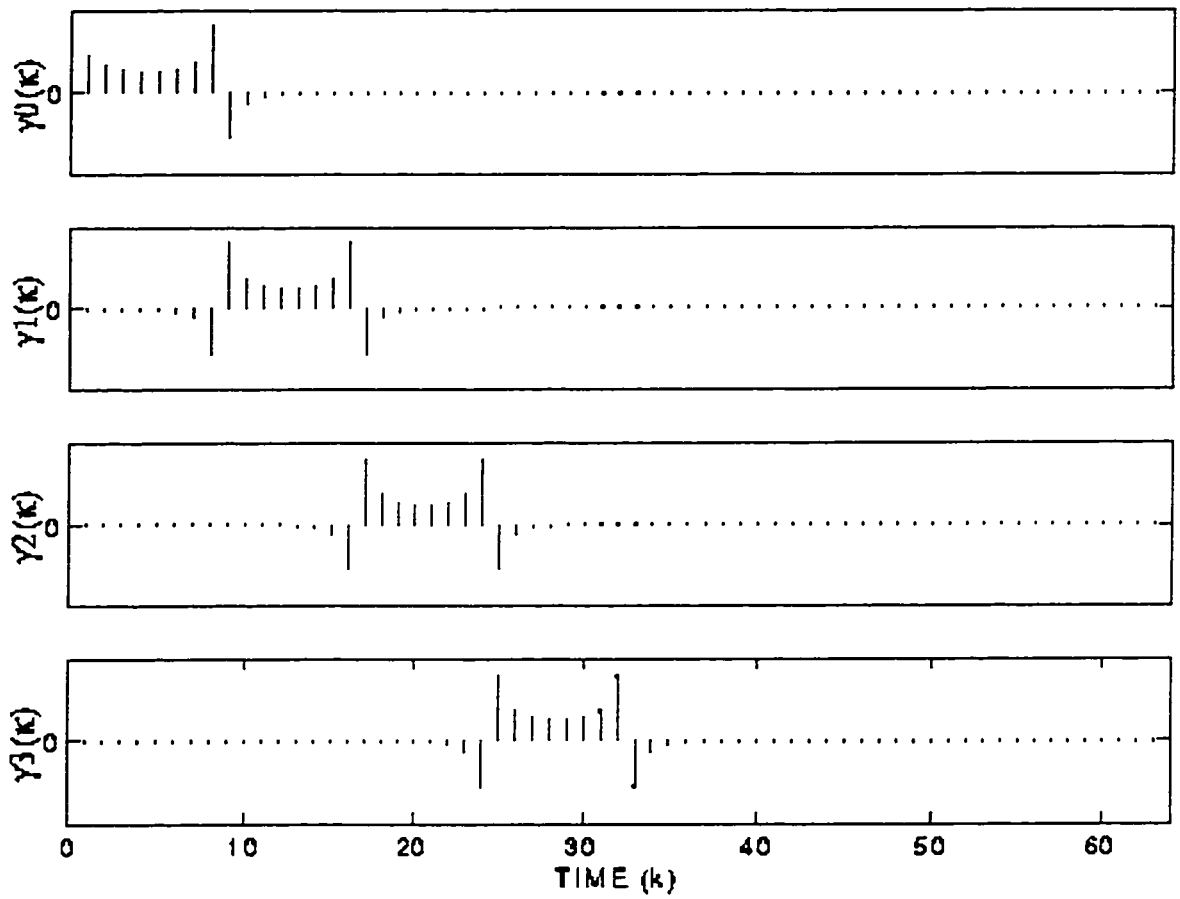


Figure 22: The biorthogonal function, $\gamma_m(k)$, of the aperiodic Real Gabor Transform for $m = 0, 1, 2, 3$.

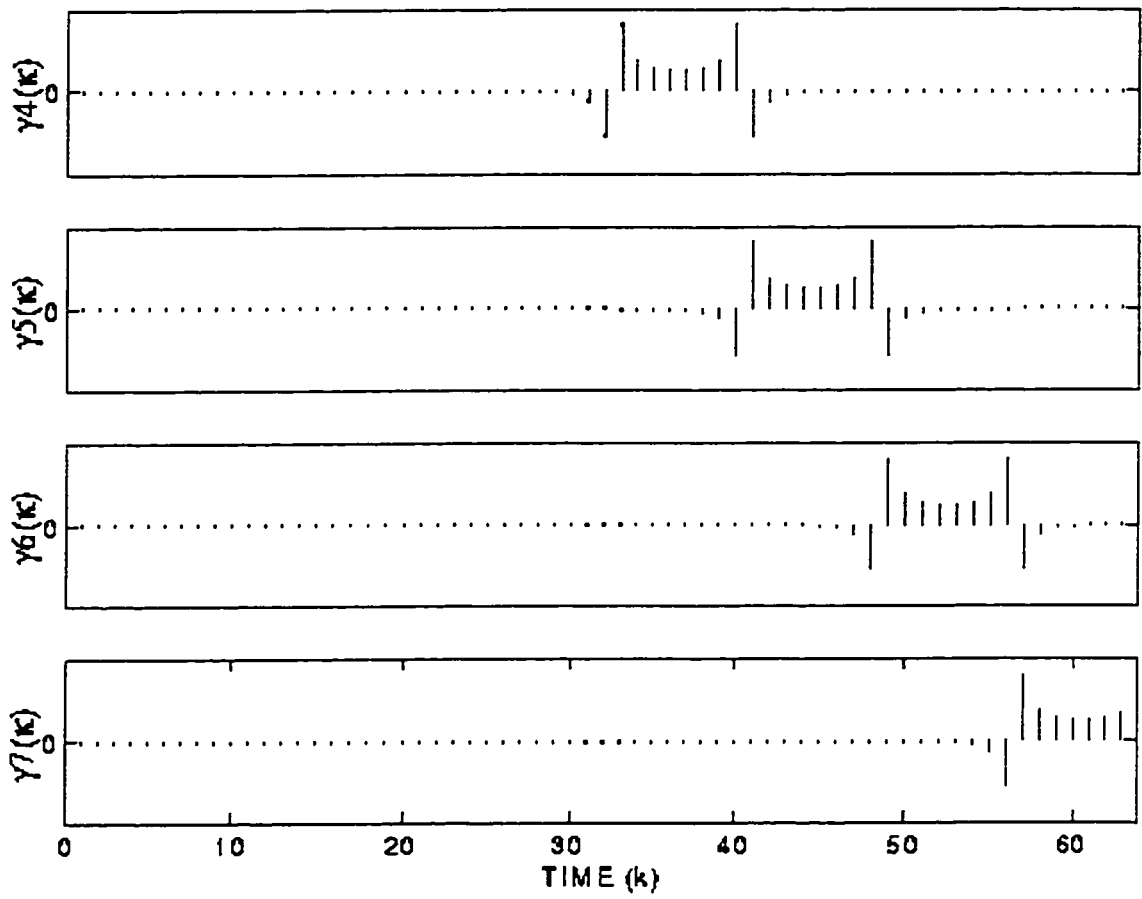


Figure 23: The biorthogonal function, $\gamma_m(k)$, of the aperiodic Real Gabor Transform for $m = 4, 5, 6, 7$.

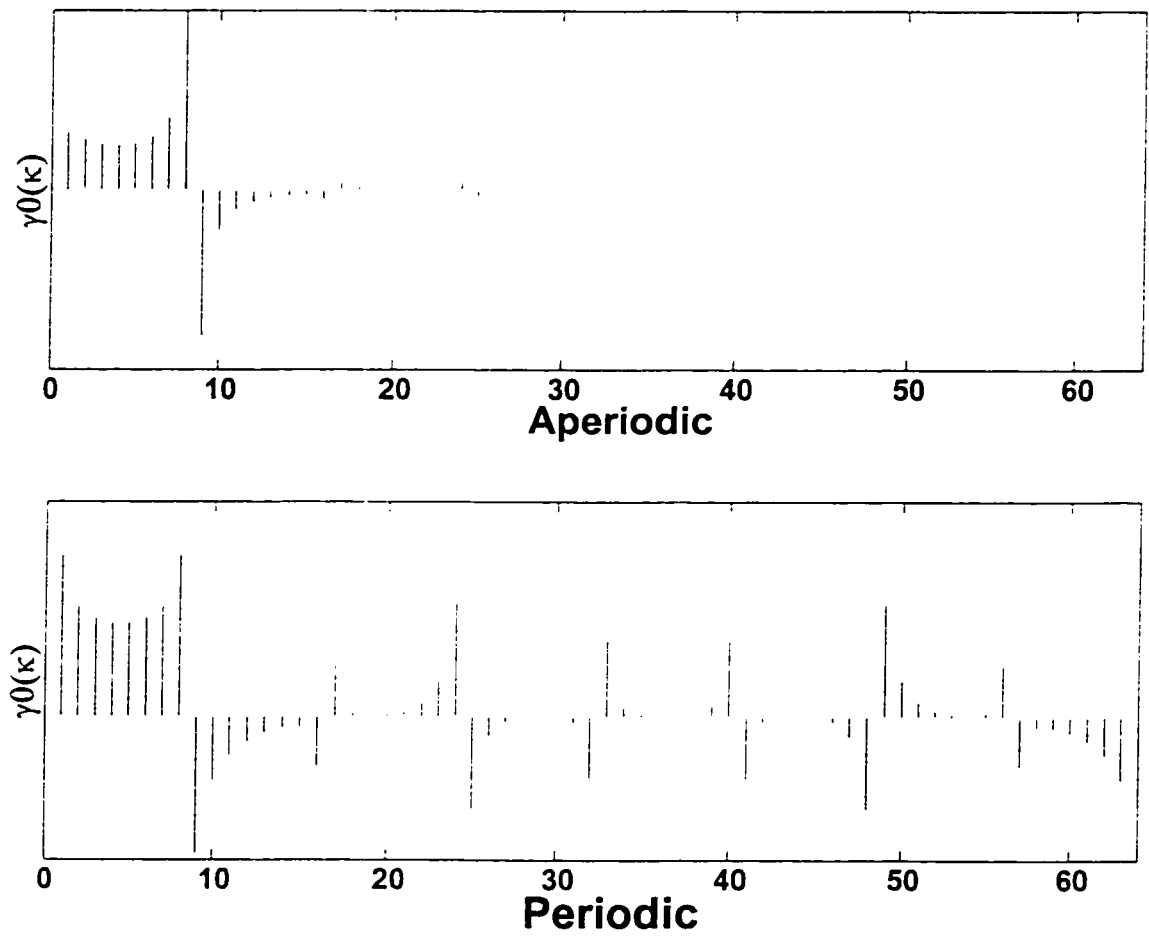


Figure 24: The biorthogonal function of the periodic and the aperiodic Real Gabor Transform for $m = 0$.

in Fig. 60 on page 171 for the periodic complex GT, in Fig. 61-(a) for the aperiodic complex GT, in Fig. 62 on page 175 for the periodic real GT, and in Figures 22 and 23 for the aperiodic real GT. For the over-sampled GT, the resulting discrete biorthogonal functions are shown in Fig. 63. All figures were plotted for $M = N = 8$ and $\sigma = N$. The details are given in Appendix C. It is obvious from these figures that, except for the over-sampling case, the resulting biorthogonal functions, including the above developed implementation, are not localized in the time domain or/and the frequency domain. This severely degrades the performance of the transforms because the Gabor coefficients $a_{m,n}$ will not reflect the signal behavior in the vicinity of $[(m - \frac{1}{2}) \Delta_t, (m + \frac{1}{2}) \Delta_t] \times [(n - \frac{1}{2}) \Delta_f, (n + \frac{1}{2}) \Delta_f]$, i.e., the Gabor coefficients $a_{m,n}$ will fail to describe the signal's local behavior.

In the next two sections, we will deal with another serious problem of any transform that is its numerical stability. Numerical stability is an inherent characteristic of the specified transform which describes how perturbations in the signal in one domain affect the signal in the transformed domain. Perturbations are due to noise, round off error, filter operation, . . . etc. Thus, perturbations are very common in most applications and cannot be ignored. In this work, we are interested to measure the stability in the actual discrete case, not in the continuous case as is the case in the literature. Thus in Section 3.5, we give a definition of the stability in the discrete case which will be applied, in Section 3.6, on various types of the currently available Gabor transform implementations.

3.5 Stability of Discrete Linear Transforms

Any discrete linear transform can be expressed in matrix notation as a transformation matrix \mathbf{A} multiplied by the discrete signal \mathbf{x} . Thus, the transformed signal \mathbf{y} is

$$\mathbf{y} = \mathbf{A} \mathbf{x} \quad (3.22)$$

while the inverse transform is

$$\hat{\mathbf{x}} = \mathbf{A}^{-1} \mathbf{y} \quad (3.23)$$

where \mathbf{A}^{-1} is the inverse of the matrix \mathbf{A} iff \mathbf{A} is a square matrix. If \mathbf{A} is rectangular, \mathbf{A}^{-1} is the Pseudo inverse of \mathbf{A} .

From linear systems theory [30], a precise measure of the sensitivity of this transform to any perturbation of the original signal \mathbf{x} can be defined by the condition number $\kappa_p(\mathbf{A})$

$$\kappa_p(\mathbf{A}) = \frac{\max \left(\|\mathbf{A}\mathbf{x}_1\|_p / \|\mathbf{x}_1\|_p \right)}{\min \left(\|\mathbf{A}\mathbf{x}_2\|_p / \|\mathbf{x}_2\|_p \right)} \quad \text{for all } \mathbf{x}_1 \neq 0 \text{ and } \mathbf{x}_2 \neq 0$$

where $\|\mathbf{x}\|_p$ is the p -norm of the \mathbf{x} . In other words, if the vectors $\Delta\mathbf{x}$ and $\Delta\mathbf{y}$ are regarded as errors correlated by

$$\mathbf{y} + \Delta\mathbf{y} = \mathbf{A} (\mathbf{x} + \Delta\mathbf{x})$$

where \mathbf{x} and \mathbf{y} satisfy (3.22) and (3.23), then

$$\frac{1}{\kappa_p(\mathbf{A})} \leq \frac{\|\Delta \mathbf{x}\|_p / \|\mathbf{x}\|_p}{\|\Delta \mathbf{y}\|_p / \|\mathbf{y}\|_p} \leq \kappa_p(\mathbf{A}) \quad (3.24)$$

This means that a small change $\Delta \mathbf{x}$ in \mathbf{x} causes a change $\Delta \mathbf{y}$ in \mathbf{y} which has a norm that can be $\kappa_p(\mathbf{A})$ times as big as the norm of $\Delta \mathbf{x}$. When \mathbf{A} is a square matrix, $\kappa_p(\mathbf{A})$ could be calculated by

$$\kappa_p(\mathbf{A}) = \|\mathbf{A}\|_p \|\mathbf{A}^{-1}\|_p$$

Here, we will focus on the most common case which is $p = 2$ and the subscript p will be dropped. The condition number $\kappa(\mathbf{A})$ ranges from 1, for orthogonal transformation matrices, to ∞ , for singular matrices. In-between, when $\kappa(\mathbf{A})$ is very large we say that the transformation matrix \mathbf{A} is *ill-conditioned* or the transform is unstable and when $\kappa(\mathbf{A})$ is small we say that \mathbf{A} is *well-conditioned* or the transform is stable.

Note that the 2-norm is invariant under unitary transformation, i.e., for any orthogonal square matrix \mathbf{Q} of appropriate dimension, the condition number $\kappa(\mathbf{A}\mathbf{Q})$ is equal to the condition number $\kappa(\mathbf{A})$.

In the following section, we will test the stability of all the types of Gabor transform in the discrete case.

3.6 Stability of Discrete Gabor Transforms

In all of the Gabor transform implementations discussed in Section 3.2, we have the synthesis equation

$$\mathbf{x} = \mathbf{H} \mathbf{E}^T \mathbf{a}$$

i.e., we have the linear transformation matrix $[\mathbf{H}\mathbf{E}^T]$ with \mathbf{H} and \mathbf{E} are defined according to the JTF transform concerned. To measure the stability of the transform, we calculate the condition number $\kappa(\mathbf{H}\mathbf{E}^T)$ of the transformation matrix $[\mathbf{H}\mathbf{E}^T]$. As we have seen from Section 3.2 the matrix \mathbf{E}^T is an orthogonal matrix in all cases. Thus, $\kappa(\mathbf{H}\mathbf{E}^T)$ is equal to $\kappa(\mathbf{H})$. The condition number $\kappa(\mathbf{H})$ for Gaussian window (for $\sigma = N$) and typical values of M and N for the above mentioned Gabor transforms are listed in Table 1. As seen from the table, Except for the over-sampling case, the condition number is very high and increases unboundedly with increasing N and M which indicates the instability of the various implementations of Gabor transform.

(N, M)	The condition number $\kappa(\mathbf{H})$				$\mathcal{OVS}\mathcal{R}=4$
	Critical-sampling				
	Complex		Real		
	Periodic	Aperiodic	Periodic	Aperiodic	
(8, 32)	12.37	11.34	12.37	12.33	1.40
(16, 16)	24.63	14.42	24.63	24.30	1.47
(16, 32)	24.63	19.38	24.63	24.54	1.47
(32, 16)	49.20	18.52	49.20	48.55	1.50
(32, 32)	49.20	28.77	49.20	49.02	1.50
(64, 64)	98.37	57.43	98.37	98.28	1.52
(128, 64)	196.74	73.64	196.74	196.55	1.53
(256, 128)	393.46	147.05	393.46	393.37	1.54

TABLE 1: Condition number of various Gabor transforms

CHAPTER 4

NON-SEPARABLE SAMPLING OF THE REAL GABOR TRANSFORM

As we have seen in Subsection 2.6.2, the implementation of the Real Gabor Transform led to a concentrated biorthogonal function in time [25]. This permits a truncated version of the biorthogonal function to be used in near lossless signal analysis and synthesis. Its frequency response, however, is not localized. The above-mentioned implementation are based on uniform separable sampling of the time-frequency plane to obtain discrete Real Gabor Transform. In this chapter we propose a simple way to implement the non-separable hexagon sampling and apply it for Real Gabor Transform. This hexagon sampling results in a localized biorthogonal function in both time and frequency domains. The matrix structure for the hexagon sampling set is developed and a computationally efficient algorithm to calculate the biorthogonal function is proposed.

4.1 Non-separable Sampling

For continuous time signal $x(t)$, The inverse Gabor Transform, or the STFT is

$$X(t, \omega) = \int x(\tau) \gamma(\tau - t) \exp(-j\omega\tau) d\tau$$

which is called the complex spectrogram. For periodic signals with period T , we need not to know the entire complex spectrogram. It suffices, however, to know the spectrogram values at points $(t_o = mT, \omega_o = n\Omega)$ where $\Omega = \frac{2\pi}{T}$ and m and n take integer values [5]. The lattice of points $(mT, n\Omega)$ has been first suggested by Gabor [3] as shown in Fig. 25. This sampling, however, was shown later that it leads to an unstable transform as well as a non localized biorthogonal function [14]. The above implementation are based on uniform separable sampling of the time-frequency plane to obtain discrete Gabor Transform. In [31, 32], a generalization for the Complex Gabor Transform was proposed in which the time-frequency plane is *arbitrarily* sampled. One of these general sampling schemes which gives better results, for over-sampled Complex Gabor Transform, is the quincunx-lattice.

For the Real Gabor Transform, the instability came from the fact that the elementary functions $S_{n,m}$ (2.19), in which Gabor expand the signal, are not orthogonal. The dependency among these elementary functions has an inverse relation with the distance between them in the JTF plane. We propose to make a generalization for the Real Gabor Transform in which the time-frequency plane is *arbitrarily* sampled (not just into rectangular lattice or grid) in such a way that the minimum distance in the JTF plane between any two elementary

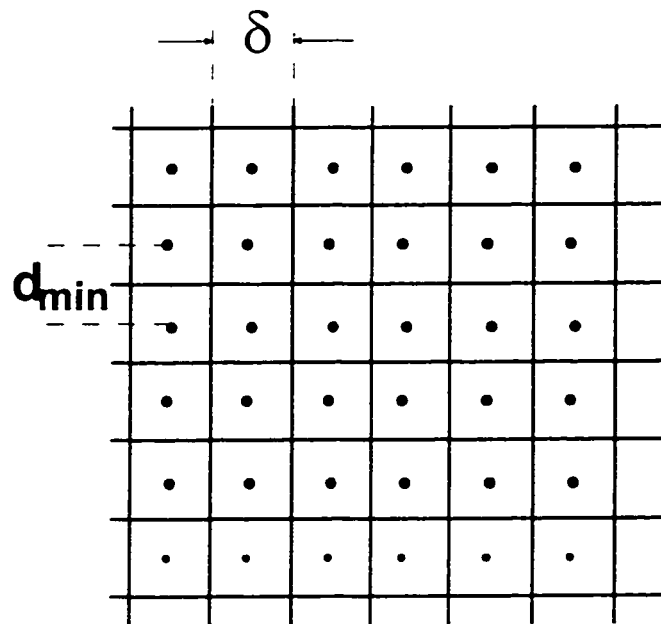


Figure 25: Packing a 2-D space with squares.

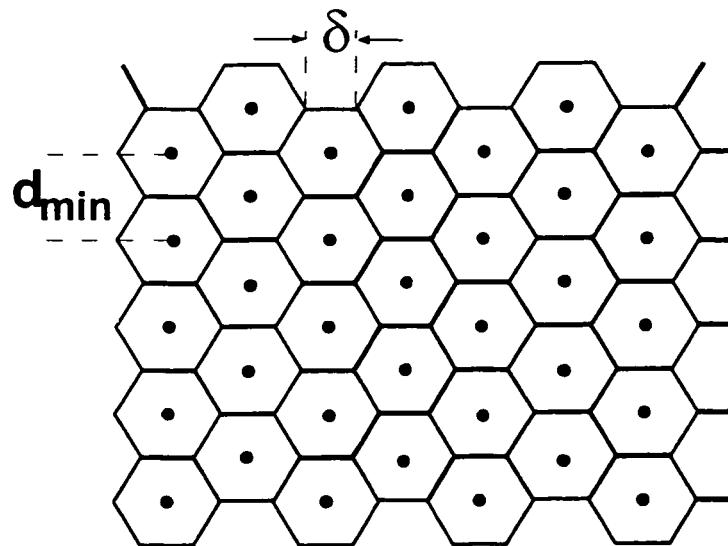


Figure 26: Packing a 2-D space with hexagons.

functions is maximized. It is well known in vector quantization literature that dividing the 2-dimensional plane into hexagon-lattice, Fig. 26, maximizes this minimum distance [33]. In this chapter, we propose a simple way to implement the non-separable hexagon-lattice sampling and apply it for Real Gabor Transform.

4.2 Hexagonal Real Gabor Transform

In the Real Gabor Transform (2.24), the signal is expanded into windowed version of the discrete cosine transform (DCT-II). DCT-II is a sampled version of the discrete-space cosine transform $C_x(\omega)$

$$C_x(\omega) = \sum_{n=0}^{\infty} 2x(n) \cos\left(\omega\left(n + \frac{1}{2}\right)\right) \quad (4.1)$$

at $\omega = \frac{\pi k}{N}$ where $k = 0, 1, \dots, N - 1$. Thus, (2.24) is a uniform sampling of the time-frequency plane at points $(t, \omega) = \left((m + \frac{1}{2})N, \frac{\pi n}{N}\right)$ where $m = 0, 1, \dots, M - 1$ as shown in Fig. 27-(a). To implement this hexagon sampling set, shown in Fig. 27-(b), notice that, for every other column the sampling points are shifted upwards by the amount $\frac{\pi}{2N}$, i.e., the resulting discrete cosine transform is a sampled version of the discrete-space cosine transform at $\omega = \frac{\pi(n + \frac{1}{2})}{N}$. This is exactly what is known as the discrete cosine transform type IV or DCT-IV (Appendix E). Thus, expanding the signal according to the hexagon

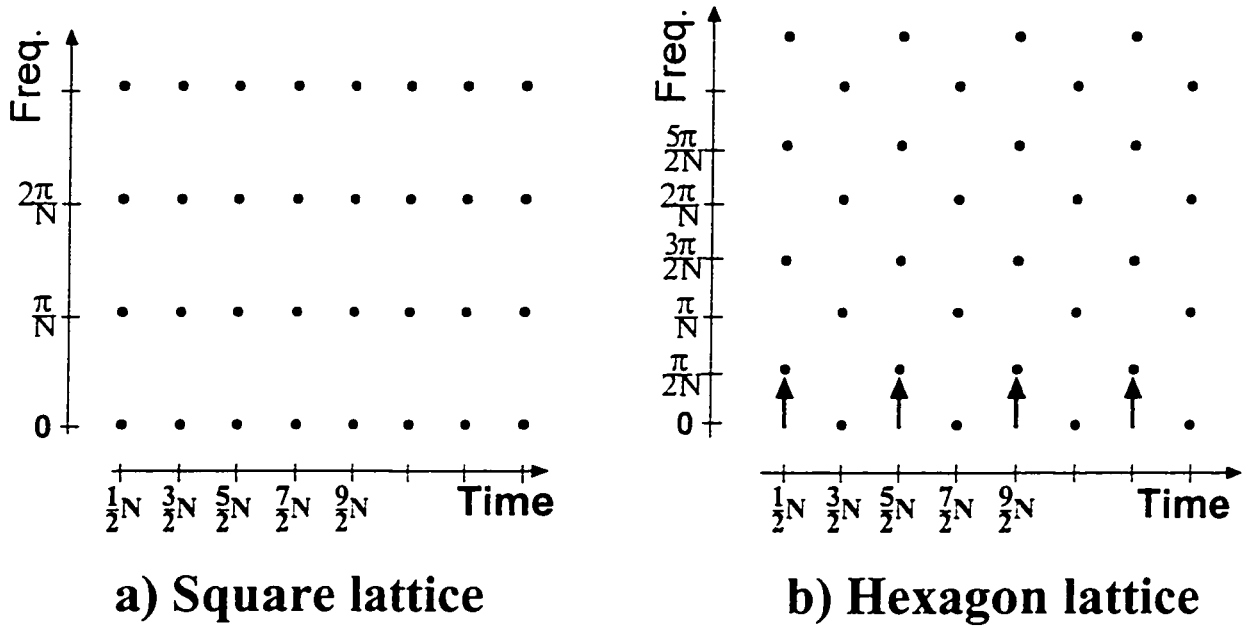


Figure 27: Constructing Hexagon lattice JTF plane sampling set (b) from Square lattice JTF plane sampling set (a)

sampling gives

$$\begin{aligned}
 x(k) = & \sum_{\substack{m=0 \\ m=\text{even}}}^{M-1} h_m(k) \sum_{n=0}^{N-1} a_{m,n} \cos \frac{\pi(k+\frac{1}{2})n}{N} \\
 & + \sum_{\substack{m=0 \\ m=\text{odd}}}^{M-1} h_m(k) \sum_{n=0}^{N-1} a_{m,n} \sqrt{\frac{2}{N}} \cos \frac{\pi(k+\frac{1}{2})(n+\frac{1}{2})}{N}
 \end{aligned} \tag{4.2}$$

where $h_m(k)$ is

$$h_m(k) = h(k - mN) = h\left(t - \left(m + \frac{1}{2}\right)T\right)\big|_{t=k} \tag{4.3}$$

Here, we choose to study the aperiodic discretization of the Real Gabor Transform⁴, and thus neither the signal nor the window are assumed to be periodic.

To put (4.2) in matrix notation, note that

$$\begin{bmatrix} x(0) \\ x(1) \\ \vdots \\ x(N-1) \end{bmatrix} = \sum_{\substack{m=0 \\ m=\text{even}}}^{M-1} h_m(k) C_1^T \begin{bmatrix} a_{m,0} \\ a_{m,1} \\ \vdots \\ a_{m,N-1} \end{bmatrix} + \sum_{\substack{m=0 \\ m=\text{odd}}}^{M-1} h_m(k) C_2^T \begin{bmatrix} a_{m,0} \\ a_{m,1} \\ \vdots \\ a_{m,N-1} \end{bmatrix} \tag{4.4}$$

where $C_1 = [c_{n,k}]_{N \times N}$ is the N -point DCT-II transform matrix defined in (3.15) and $C_2 = [c_{n,k}]_{N \times N}$ is the N -point DCT-IV transform matrix defined in (E-1).

Equation (4.4) can be written as

$$\mathbf{x}_0 = \sum_{\substack{m=0 \\ m=\text{even}}}^{M-1} h_m(k) C_1^T \mathbf{a}_m + \sum_{\substack{m=0 \\ m=\text{odd}}}^{M-1} h_m(k) C_2^T \mathbf{a}_m \tag{4.5}$$

⁴ For Gabor Transform, the assumption of periodicity is a more radical assumption than for the Fourier transform, as it involves a periodization of the window function as well as the signal [19].

where a_m and x_m are as defined in (3.3) and (3.5) respectively. Note that, based on the DCT-IV properties (see Appendix E), one can write

$$\mathbf{x}_1 = \sum_{\text{even}} h_{m-1}(k) C_1^T J \mathbf{a}_m - \sum_{\text{odd}} h_{m-1}(k) C_2 J \mathbf{a}_m \quad (4.6)$$

$$\mathbf{x}_2 = \sum_{\text{even}} h_{m-2}(k) C_1^T \mathbf{a}_m - \sum_{\text{odd}} h_{m-2}(k) C_2 \mathbf{a}_m \quad (4.7)$$

$$\mathbf{x}_3 = \sum_{\text{even}} h_{m-3}(k) C_1^T J \mathbf{a}_m + \sum_{\text{odd}} h_{m-3}(k) C_2 J \mathbf{a}_m \quad (4.8)$$

where J is the $N \times N$ row exchange matrix defined in (A-1).

Based on (4.5), (4.6), (4.7), and (4.8), one can rewrite (4.2) in matrix form as

$$\begin{bmatrix} H_0 C_1^T & + H_{-1} C_2^T & \cdots & + H_{-M+1} C_2^T \\ H_1 J C_1^T & - H_0 J C_2^T & \cdots & - H_{-M+2} J C_2^T \\ H_2 C_1^T & - H_1 C_2^T & \cdots & - H_{-M+3} C_2^T \\ H_3 J C_1^T & + H_2 J C_2^T & \cdots & + H_{-M+4} J C_2^T \\ \vdots & \vdots & \ddots & \vdots \\ H_{M-1} C_1^T & + H_{M-1} J C_2^T & \cdots & + H_0 J C_2^T \end{bmatrix} \begin{bmatrix} \mathbf{a}_0 \\ \mathbf{a}_1 \\ \mathbf{a}_2 \\ \mathbf{a}_3 \\ \vdots \\ \mathbf{a}_M \end{bmatrix} = \begin{bmatrix} \mathbf{x}_0 \\ \mathbf{x}_1 \\ \mathbf{x}_2 \\ \mathbf{x}_3 \\ \vdots \\ \mathbf{x}_{M-1} \end{bmatrix} \quad (4.9)$$

or

$$\mathbf{H} \mathbf{C}^T \mathbf{a} = \mathbf{x} \quad (4.10)$$

where H_m , \mathbf{a} and \mathbf{x} are defined in (3.6), (3.2), and (3.4), respectively with

$$\mathbf{H} = \begin{bmatrix} H_0 & H_{-1} J & \cdots & H_{-M+1} J \\ H_1 J & -H_0 & \cdots & -H_{-M+2} \\ H_2 & -H_1 J & \cdots & -H_{-M+3} J \\ H_3 J & H_2 & \cdots & H_{-M+4} \\ \vdots & \vdots & \ddots & \vdots \\ H_{M-1} J & H_{M-2} & \cdots & H_0 \end{bmatrix} \quad (4.11)$$

and

$$\mathbf{C}^T \triangleq \begin{bmatrix} C_1^T & & & & \\ & JC_2^T & & & \\ & & \ddots & & \\ & & & C_1^T & \\ & & & & JC_2^T \end{bmatrix} \quad (4.12)$$

Equation (4.10) is the synthesis transform in matrix notation. Its inverse, i.e., the analysis transform, is $\mathbf{a} = (\mathbf{C}^T)^{-1} \mathbf{H}^{-1} \mathbf{x}$. Since the \mathbf{C} matrix is unitary, i.e., $(\mathbf{C}^T)^{-1} = \mathbf{C}$, thus,

$$\mathbf{a} = \mathbf{C} \mathbf{H}^{-1} \mathbf{x} \quad (4.13)$$

The matrix \mathbf{H} is block-Toeplitz matrix. Its inverse \mathbf{H}^{-1} is not, in general, block-Toeplitz matrix. Thus, \mathbf{H}^{-1} can be written as

$$\mathbf{H}^{-1} = \begin{bmatrix} \Gamma_0^{(0)} & J\Gamma_1^{(0)} & \Gamma_2^{(0)} & J\Gamma_3^{(0)} & \cdots & J\Gamma_{M-1}^{(0)} \\ J\Gamma_{-1}^{(1)} & -\Gamma_0^{(1)} & -J\Gamma_1^{(1)} & \Gamma_2^{(1)} & \cdots & \Gamma_{M-2}^{(1)} \\ \vdots & \vdots & \vdots & \vdots & \ddots & \vdots \\ J\Gamma_{-M+1}^{(M-1)} & -\Gamma_{-M+2}^{(M-1)} & -J\Gamma_{-M+3}^{(M-1)} & \Gamma_{-M+4}^{(M-1)} & \cdots & \Gamma_0^{(M-1)} \end{bmatrix} \quad (4.14)$$

with $N \times N$ diagonal blocks

$$\Gamma_l^{(m)} \triangleq \begin{bmatrix} \gamma_m(lN) & & & \\ & \gamma_m(lN+1) & & \\ & & \ddots & \\ & & & \gamma_m(lN+N-1) \end{bmatrix} \quad (4.15)$$

where $\gamma_m(k)$ comprises the m -time shift of the biorthogonal function. For Gaussian window, the resulting $\gamma_m(k)$ is plotted, for $m = 3$, in Fig. 28. This figure shows the nice concentration of the resulting $\gamma_m(k)$ in both time and frequency compared with previous work.

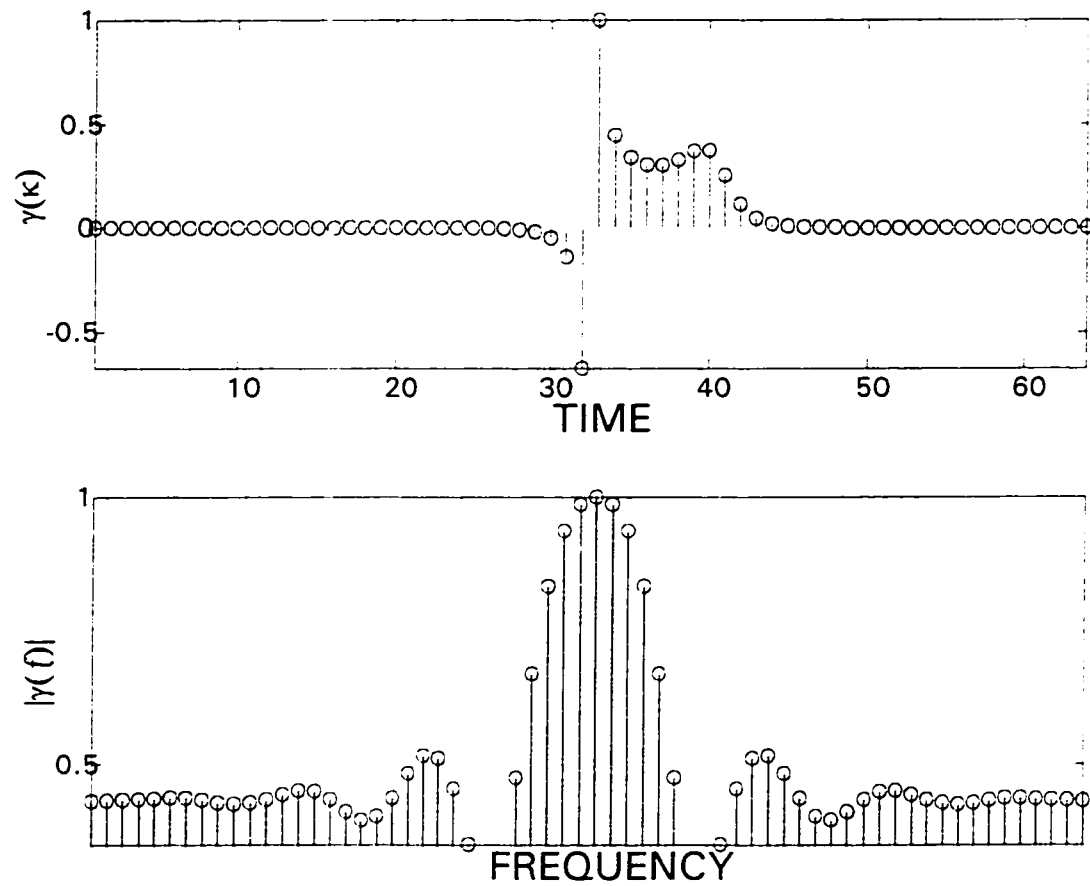


Figure 28: The discrete biorthogonal function of the Hexagonal Real Gabor transform.

As a comparison, the biorthogonal function of Stewart implementation and this implementation in the frequency domain is plotted in Fig. 29.

In the next two sections, we will give a practical implementations of the hexagon sampling Real Gabor Transform.

4.3 Practical Calculation of \mathbf{H}^{-1}

The matrix \mathbf{H} (4.11) is an $MN \times MN$ matrix which is very costly to invert. \mathbf{H} is a block-Toeplitz matrix with diagonal or anti-diagonal blocks. Using row and column permutations, \mathbf{H} can be converted to a block-diagonal matrix with N blocks. Each block is of dimension $M \times M$ which can be inverted separately as follows:

Define (as in Appendix A) a permutation $MN \times MN$ matrix \mathbf{P} whose encoding vector $p(k)$, for $k = 0, \dots, MN - 1$, is given by

$$p(k) = \eta(N - 1) + (-1)^\eta \left\lfloor \frac{k}{M} \right\rfloor + N(k \bmod M) \quad (4.16)$$

where $\eta = k \bmod 2$ and $\lfloor x \rfloor$ means the integer part of x . The matrix \mathbf{PHP} is block-diagonal matrix given by

$$\mathbf{PHP} = \begin{bmatrix} \mathbf{D}_0 & & & \\ & \mathbf{D}_1 & & \\ & & \ddots & \\ & & & \mathbf{D}_{N-1} \end{bmatrix} \quad (4.17)$$

where \mathbf{D}_n is $M \times M$ block-Toeplitz with 2×2 blocks. Efficient methods for inverting

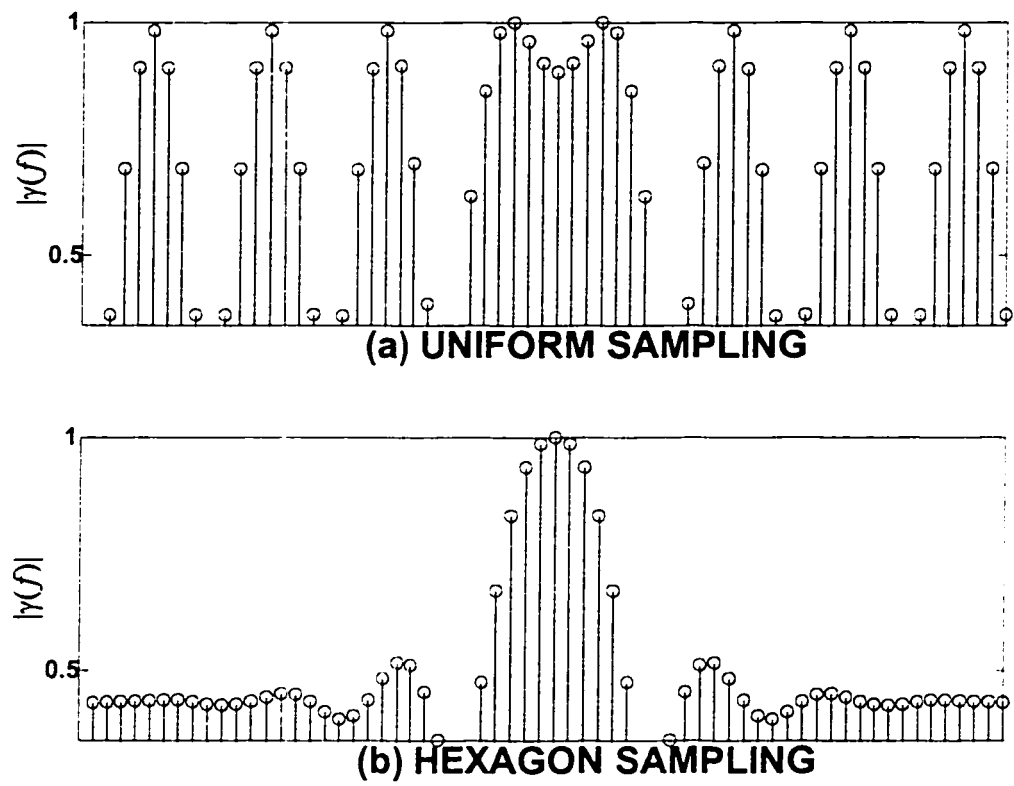


Figure 29: Comparison between the biorthogonal function in the frequency domain in (a) the case of uniform sampling and (b) hexagon sampling.

block-Toeplitz matrices exist [34–37] which can invert this matrix in $\mathcal{O}(M^2)$, or even in $\mathcal{O}(M \log M)$ as some iterative algorithms claim. Thus, the whole inversion process of **PHP** takes $\mathcal{O}(NM^2)$ or $\mathcal{O}(NM \log M)$. Consequently, the inverse \mathbf{H}^{-1} is given by

$$\mathbf{H}^{-1} = \mathbf{P} (\mathbf{PHP})^{-1} \mathbf{P} \quad (4.18)$$

and the Gabor coefficient is given by

$$\mathbf{a} = \mathbf{C} \mathbf{P} (\mathbf{PHP})^{-1} \mathbf{P} \mathbf{x} \quad (4.19)$$

4.4 Practical Calculation of the Hexagonal Real Gabor Transform coefficients

Referring to (4.13), in order to compute the m^{th} N Gabor coefficients:

- Multiply the signal $x(k)$ by the biorthogonal function $\gamma_m(k)$.
- If m is even
 - (a) Add the M sections of length N after flipping⁵the odd numbered sections.
 - (b) Take the DCT transform (3.15) of the resulting vector.
- If m is odd
 - (a) Add the M sections of length N after flipping the odd numbered sections and following the sign order as indicated in (6.49).

⁵ Flipping an N -dimensional vector \mathbf{x} is performed by replacing the element x_i by x_{N-i} .

(b) Take the DCT-IV transform (E-1) of the resulting vector.

Assuming that the N -point DCT or DCT-IV takes $\frac{N}{2} \log_2 N$ multiplications, this operation requires $NM^2 + \frac{MN}{2} \log_2 N = L(M + \frac{1}{2} \log_2 N)$ multiplications. There is still room for significantly reducing this number of operation by truncating the Gaussian function to a length $2N$ (i.e., $h(n)$ is zero outside the interval $[-\frac{N}{2} : \frac{3N}{2} - 1]$) as illustrated in Fig. 30. Under this proposed truncation, D_n (the diagonal blocks of \mathbf{PHP}) will be a block-diagonal matrix given by

$$D_n = \begin{cases} \begin{bmatrix} a_n & & & & \\ & b_n & & & \\ & & b_n & & \\ & & & \ddots & \\ & & & & b_n & \\ & & & & & a_n \end{bmatrix} & \text{for } n = 0, \dots, \frac{N}{2} - 1 \\ \begin{bmatrix} c_n & & & & \\ & c_n & & & \\ & & \ddots & & \\ & & & c_n \end{bmatrix} & \text{for } n = \frac{N}{2}, \dots, N - 1 \end{cases}$$

where a_n is $[h(n)]$ and b_n and c_n are a 2×2 matrices defined by

$$b_n \triangleq \begin{bmatrix} +h(N - n - 1) & -h(-n - 1) \\ -h(N + n) & +h(n) \end{bmatrix} \quad (4.20)$$

$$c_n \triangleq \begin{bmatrix} +h(n) & -h(N - n) \\ -h(2N - n) & +h(N - n) \end{bmatrix} \quad (4.21)$$

If $h(n)$ is symmetric as in the case of Gaussian window, b_n and c_n will be

$$b_n \triangleq \begin{bmatrix} +h(n) & -h(-n - 1) \\ -h(-n - 1) & +h(n) \end{bmatrix} \quad (4.22)$$

$$\mathbf{c}_n \triangleq \begin{bmatrix} +h(n) & -h(N-n) \\ -h(N-n) & +h(n) \end{bmatrix} \quad (4.23)$$

Thus, the inversion of the $MN \times MN$ matrix \mathbf{H} reduces to an N inversions of a 2×2 matrix which takes 5 operations and $\frac{N}{2}$ inversions of a 1×1 matrix which takes 1 operation. In this case the inversion of \mathbf{H} takes only $5.5N$ which is a considerable reduction compared to $\mathcal{O}(NM^2)$ or $\mathcal{O}(NM \log M)$.

Note that, since the inversion of a block-diagonal matrix is also a block-diagonal with the same dimension, it follows that \mathbf{D}_n^{-1} is also a block-diagonal matrix with 2×2 blocks. Thus, $[\mathbf{PHP}]^{-1} = \mathbf{P}^T \mathbf{H}^{-1} \mathbf{P}^T$ is also a block-diagonal matrix. As a consequence, \mathbf{H}^{-1} has the transpose structure of \mathbf{H} . This illustrates why the truncation of the window to a length of $2N$ will give a biorthogonal function which also has a length of exactly $2N$. In this case, the calculation of Gabor coefficients requires only $L(2 + \frac{1}{2} \log_2 N)$ operations which is great reduction especially for large M . This proposed algorithm is faster than the Zak transform based algorithm which takes $L(1 + \log_2 N + \log_2 L)$ operations and is claimed to be the fastest algorithm currently available [17]. Table 2 shows the operational savings of the proposed method over the Zak transform based method.

The only price to be paid is the ripples appearing in the frequency response in the Gaussian window due to truncation. Because it is too small, the ripples do not appear in Fig. 30. The amplitudes of these ripples, however, are far less than the amplitude of the main lobe. The ratio is more than 45 db for any practical values of M and N (For example, for $N = 16$ the ratio is 51.4 db, regardless of the value of M). Thus, for all practical purposes, these ripples have negligible effect.

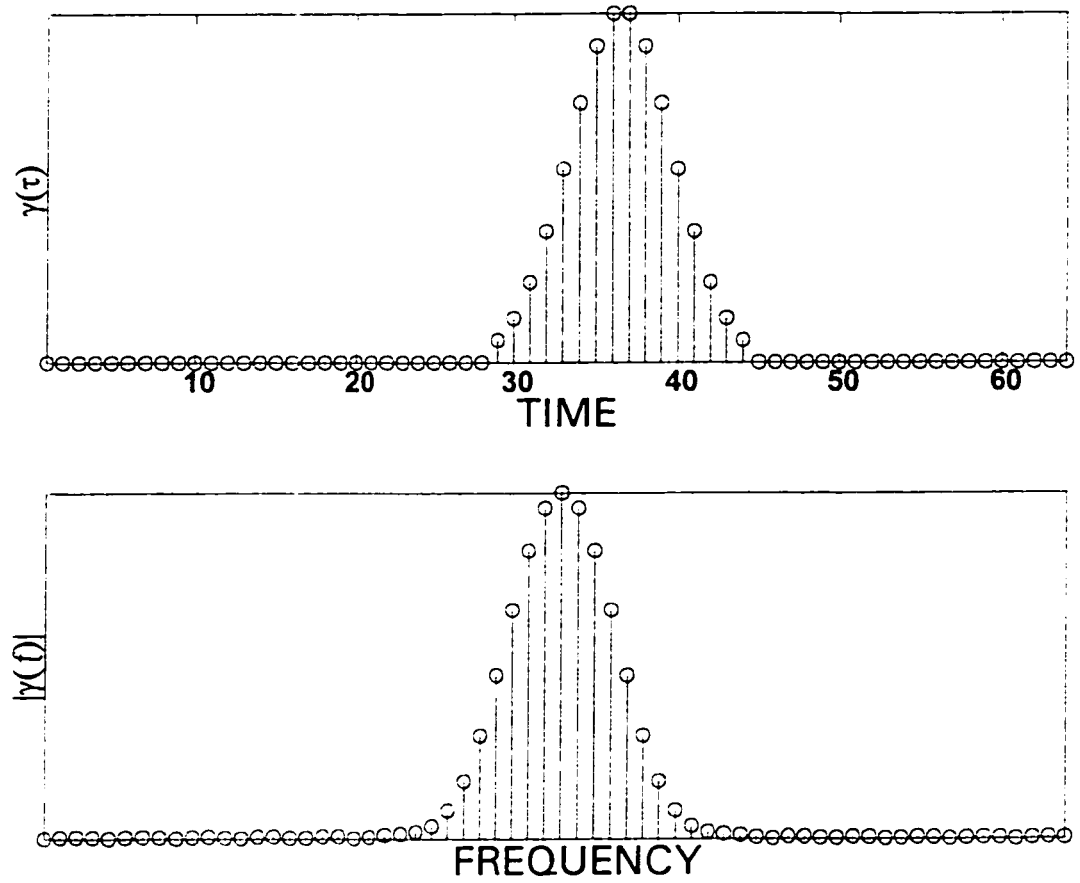


Figure 30: Truncated discrete Gaussian window to a length of $2N$. $M = N = 8$.

N	M	# of multiplications		Saving Ratio
		Proposed	Zak	
8	32	896	1,920	2.14
8	256	7,168	21,504	3.0
8	512	14,336	47,104	3.29
16	32	2,048	4,096	2.0
16	256	16,384	45,056	2.75
16	542	32,768	98,304	3.0

TABLE 2: Operational savings of the truncated hexagon sampling method over the Zak based one

It is worth noting that this is an exact representation of the signal and not just an approximation like the case mentioned in [25].

Example 4.1

To compare the proposed truncated transform with the original hexagon sampling transform, consider a test signal $x(k)$ of length 1024 composed of a concatenation of two sinusoids with the same length and different frequencies and amplitudes, $(f_1 = \frac{1}{4}, f_2 = \frac{1}{2})$ and $(a_1 = 10, a_2 = 20)$ respectively, i.e.,

$$x(k) = \begin{cases} a_1 \cos 2\pi f_1 k & k = 1, \dots, 512 \\ a_2 \cos 2\pi f_2 k & k = 513, \dots, 1024 \end{cases}$$

This signal is plotted in the time domain in Fig. 31 and in the JTF domain in Fig. 33 using the hexagon sampling transform. After coming back to the time domain, the sum-square error between the original signal and the transformed one was $2.2e-024$ (which is the computer round off error) indicating zero error. The same signal is plotted in the JTF domain in Fig. 32 using the proposed truncated hexagon sampling transform. It is obvious that both transforms gives, almost, the same JTF representation. After coming back to the time domain from the truncated method JTF domain, the sum-square error between the original signal and the transformed one was $2.2e-024$ (which is also the computer round off error) indicating zero error.

To compare with the truncated transform proposed in [25], the same signal is plotted in the JTF domain in Figures 34 and 35 using the truncated transform proposed in [25] for truncated window length $2N$ and $3N$ respectively. After coming back to the time domain, the sum-square error between the original signal and the transformed one was 39.19, and 10.59 respectively. Comparing Figures 34 and 35 with Figures 33 and 32, it is obvious that the hexagon transforms (both untruncated and truncated) give more distinctive representation (specially in the frequency direction). This is because the biorthogonal functions of the hexagon sampling transforms have more concentration in the frequency domain than those of the Real Gabor Transform (see Fig. 29).

4.5 Conclusion

In this chapter we have presented an implementation of the critically-sampled Real Gabor Transform for nonseparable JTF plane sampling set. We have shown that the resulting

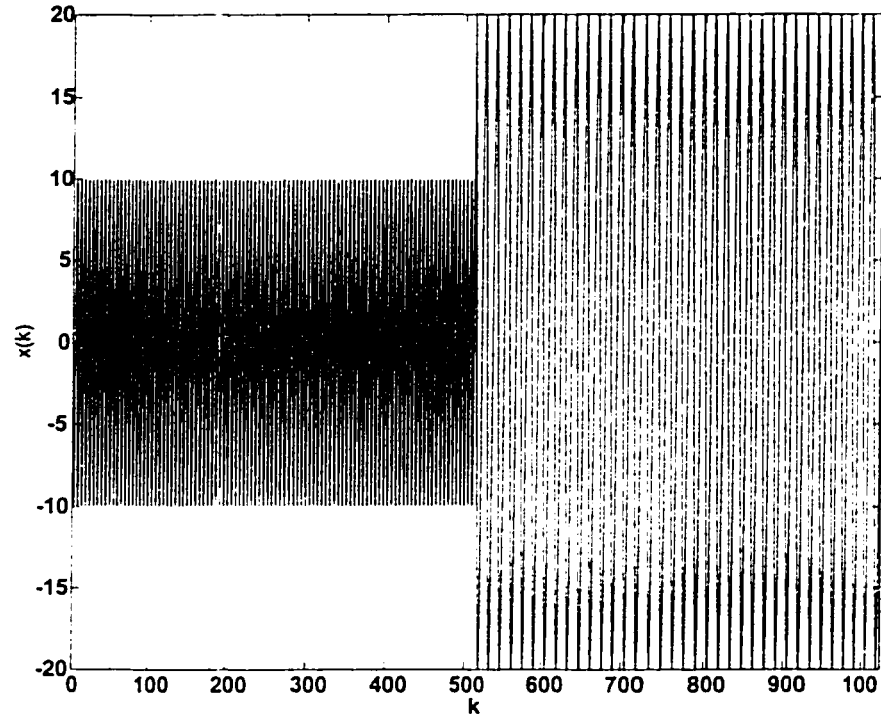


Figure 31: A test signal composed of a concatenation of two sinusoids with different amplitudes and frequencies.

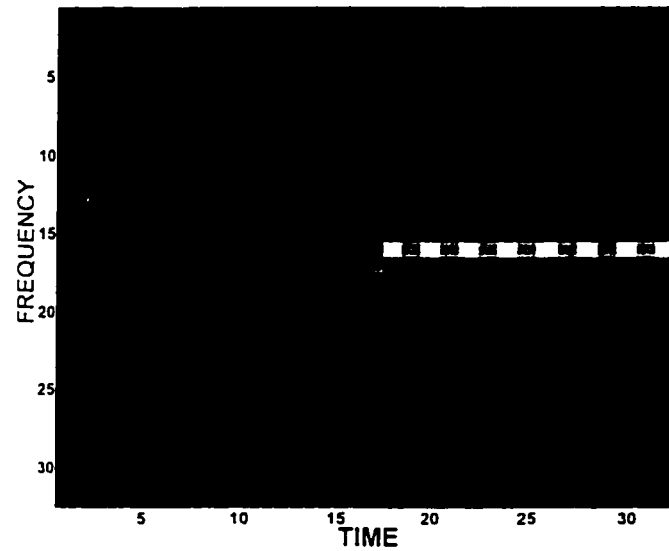


Figure 32: JTF representation of the test signal using the truncated hexagon real Gabor transform with length $2N$.

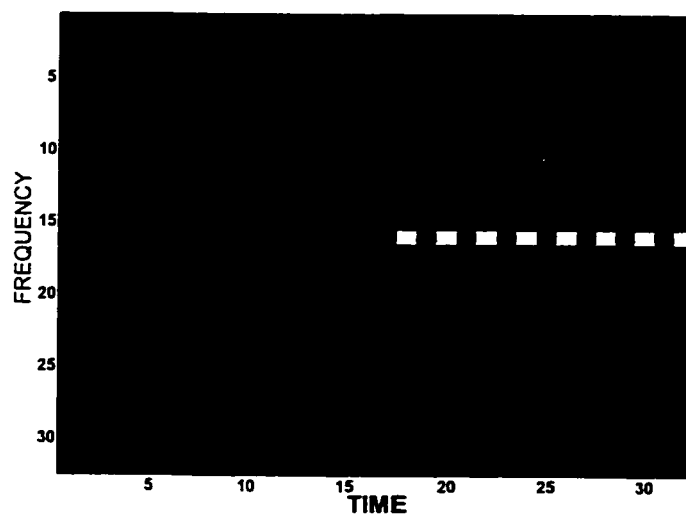


Figure 33: JTF representation of the test signal using the hexagon real Gabor transform.

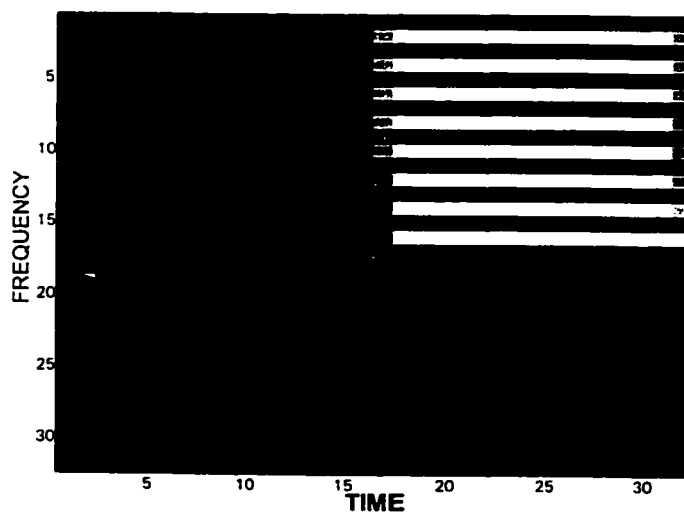


Figure 34: JTF representation of the test signal using the truncated real Gabor transform with length $2N$.

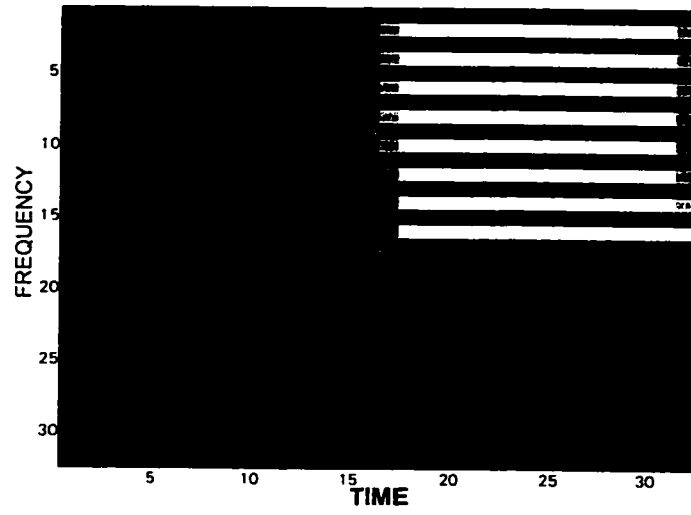


Figure 35: JTF representation of the test signal using the truncated real Gabor transform with length $3N$.

biorthogonal function has better localization in frequency domain. An efficient method to calculate the transform coefficients for any window type is presented. We have also derived a practical implementation of the transform using a truncated version of the analysis window to be of length $2N$. We showed that this truncation has negligible effect on the characteristics of the transform. In addition, it requires only $L \{2 + \frac{1}{2} \log_2 N\}$ operations for computing the transform coefficients and $5.5N$ operations for computing the biorthogonal function. Thus, it is faster than any Gabor transform currently available. Unlike other methods of truncation, this method gives exact reconstruction of the signal.

CHAPTER 5

ORTHOGONAL GABOR-DCT TRANSFORM

In this chapter, another new linear, critical sampled, Real Gabor Transform, Gabor-DCT, is presented. In this implementation, we focus on the stability problem. Our objective is to get an orthogonal transform which is thus stable. In addition to orthogonality, the resulting transform is computationally less demanding than other Gabor Transforms. We prove that for Real Gabor Transform any window function of length $2N$ will lead to a biorthogonal function having exactly a length $2N$. The conditions on this window function to be a candidate of an orthogonal Real Gabor Transform is derived. Two examples of such window function are given.

5.1 Introduction

The discrete cosine transform (DCT) is very popular in image processing. This is due to its decorrelative properties and the existence of fast algorithms for computing the coefficients that can be easily implemented by VLSI. It is, however, not local in the spa-

tial domain. Therefore, it must be calculated over a number of spatial partitioned regions (blocks). On the other hand, Gabor functions have optimal localization in the joint spatial and frequency domain.

As we saw in Section 2.2, Gabor transform expands signals into a time and frequency shifts of the Gabor elementary function which is the product of a window function by Fourier kernels. In [38], an attempt to combine the advantages of both DCT and Gabor transform was made through replacing the Fourier kernels of the Gabor elementary functions by DCT kernels. This was named Gabor-DCT and an iterative algorithm was proposed to calculate its coefficients. Another implementation of the Gabor-DCT was proposed in [21] by maintaining the same biorthogonal function produced in the normal Gabor transform and replacing the DFT transform by the DCT one. As we saw in Subsection 2.6.2, Stewart *et al.* [25] worked out the Real Gabor Expansion (2.18) in rigorous mathematical terms and ended up with another Gabor-DCT (Real Gabor Transform) that has a better biorthogonal function than the original Gabor transform. This biorthogonal function is localized in the time domain.

Unfortunately, the resulting transforms in all the above-mentioned cases are unstable, as will be proved in Section 5.3. This means that errors (due to noise or truncation . . . etc.) may be severely magnified during the transformation process. Thus, finding a stable Gabor-DCT transform is extremely important. *Orthogonal* transforms are the best stable ones since they do not produce any error magnification during the transformation process. Another advantage of *orthogonal* transforms is that there is no need to calculate the biorthogonal function since the same window is used for both analysis and synthesis operations.

In this chapter, an *orthogonal* Gabor-DCT transform is proposed by modifying the analysis window function. Here, the conditions on the analysis window to be a candidate of the orthogonal Gabor-DCT are developed and two members of this window family are given.

The organization of this chapter is as follows. In Section 5.2 we will set the Real Gabor transform in the appropriate matrix format which will be used in our analysis. In Section 5.3, the stability of various Gabor-DCT implementations is calculated. In Section 5.4, the conditions to be satisfied by the window function so that it leads to an orthogonal transform will be derived. Two examples of this window function are demonstrated in Section 5.5.

5.2 Real Gabor Transform: Second Visit

As we showed in Subsection 2.6.2, a discretization and reformulation of the Real Gabor Expansion (2.18) in matrix form led to

$$\begin{bmatrix} H_0(CJ^0)^T & H_{M-1}(CJ^0)^T & \cdots & H_1(CJ^0)^T \\ H_1(CJ^1)^T & H_0(CJ^1)^T & \cdots & H_2(CJ^1)^T \\ \vdots & \vdots & \ddots & \vdots \\ H_{M-1}(CJ^{M-1})^T & H_{M-2}(CJ^{M-1})^T & \cdots & H_0(CJ^{M-1})^T \end{bmatrix} \begin{bmatrix} \mathbf{a}_1 \\ \mathbf{a}_2 \\ \vdots \\ \mathbf{a}_M \end{bmatrix} = \begin{bmatrix} \mathbf{x}_1 \\ \mathbf{x}_2 \\ \vdots \\ \mathbf{x}_M \end{bmatrix} \quad (5.1)$$

Here, (5.1) is put in the following matrix form

$$\begin{bmatrix} H_0 & H_{M-1} & \cdots & H_1 \\ H_1 J & H_0 J & \cdots & H_2 J \\ \vdots & \vdots & \ddots & \vdots \\ H_{M-1} J & H_{M-2} J & \cdots & H_0 J \end{bmatrix} \begin{bmatrix} C^T & \mathbf{0} & \cdots & \mathbf{0} \\ \mathbf{0} & C^T & \cdots & \mathbf{0} \\ \vdots & \vdots & \ddots & \vdots \\ \mathbf{0} & \mathbf{0} & \cdots & C^T \end{bmatrix} \mathbf{a} = \mathbf{x} \quad (5.2)$$

where \mathbf{a} , \mathbf{x} , J , H_m , and C are as defined in (3.2), (3.4), (A-1), (3.6), and (3.15) respectively.

Equation (5.2) can be rewritten as

$$\mathbf{H} \mathbf{C}^T \mathbf{a} = \mathbf{x} \quad (\text{synthesis equation}) \quad (5.3)$$

where the matrix \mathbf{H} provides the desired windowing effect and is given by

$$\mathbf{H} \triangleq \begin{pmatrix} H_0 & H_{M-1} & \cdots & H_1 \\ H_1 J & H_0 J & \cdots & H_2 J \\ \vdots & \vdots & \ddots & \vdots \\ H_{M-1} J & H_{M-2} J & \cdots & H_0 J \end{pmatrix} \quad (5.4)$$

and \mathbf{C} is an $MN \times MN$ block-diagonal matrix which represents the linear transformation and is given by

$$\mathbf{C} \triangleq \begin{pmatrix} C & & & \\ & C & & \\ & & \ddots & \\ & & & C \end{pmatrix} \quad (5.5)$$

It is to be noted that \mathbf{H} and \mathbf{C} as defined here are different from those used in Subsection 2.6.2. Equation (5.3) is the synthesis transform. Its inverse, i.e., the analysis transform, is

$$\mathbf{a} = (\mathbf{C}^T)^{-1} \mathbf{H}^{-1} \mathbf{x}$$

Since the \mathbf{C} matrix is unitary, i.e., $(\mathbf{C}^T)^{-1} = \mathbf{C}$, then

$$\mathbf{a} = \mathbf{C} \mathbf{H}^{-1} \mathbf{x} \quad (5.6)$$

In the next section we will test quantitatively the stability of this Transform.

5.3 Stability of Gabor-DCT Transforms

For the Gabor-DCT transform, we have the synthesis equation (5.3), i.e., we have the linear transformation matrix $[\mathbf{H}\mathbf{C}^T]$. As we have proved in Section 3.5, to measure the stability of the transform, we calculate the condition number of the matrix $[\mathbf{H}\mathbf{C}^T]$. The matrix \mathbf{C}^T is orthogonal. Thus, the condition number of $[\mathbf{H}\mathbf{C}^T]$ is equal to the condition number of \mathbf{H} . The matrix \mathbf{H} is not, in general, orthogonal and its condition number for Gaussian window and typical values of M and N are listed in Table 3. It is clear from this table that the condition number for Gabor-DCT transform is very high and increases without bound as (N, M) increases, thus indicating the instability of the transform. In the next section, we will develop the orthogonal Gabor-DCT where the condition number is exactly *one*. This guarantees no error magnification during the analysis or the synthesis transforms.

5.4 Orthogonal Gabor-DCT Transform

In this section, we will derive an orthogonal type of the Gabor-DCT transform reviewed in Section 5.2. We will show first that, unlike the normal Gabor transform, using any analysis window of length $2N$ for Gabor-DCT will lead to a biorthogonal function of the same length. Then we will derive the necessary and sufficient conditions on $h(n)$ to be a candidate of the Orthogonal Gabor-DCT transform. We start by the following theorem

Theorem 5.1

For any transform that has a structure as defined in (5.3) and (5.4), any window of length $2N$ will lead to a biorthogonal function of the same length.

(N, M)	$\kappa(\mathbf{H}\mathbf{C}^T)$ ref. [21]	$\kappa(\mathbf{H}\mathbf{C}^T)$ ref. [25]
(8, 32)	5.94	6.1025
(16, 16)	9.677	12.204
(16, 32)	11.215	12.204
(32, 16)	14.4	24.408
(32, 32)	19.27	24.408
(64, 64)	38.44	48.817
(128, 64)	57.069	97.633
(256, 128)	133.60	195.27

TABLE 3: Condition number of various implementations of Gabor-DCT transform

Proof. As we saw in Section 5.2, the biorthogonal function can be obtained via the inversion of the matrix \mathbf{H} . The matrix \mathbf{H} (5.4) is a block-Circulant matrix with diagonal or anti-diagonal blocks. If the window function is of length $2N$ (i.e., $h(n)$ is zero outside the interval $[-\frac{N}{2} : \frac{3N}{2} - 1]$), \mathbf{H} will have the structure

$$\mathbf{H} = \begin{bmatrix} \text{---} & \text{---} & \text{---} & \text{---} & \text{---} \\ \text{---} & \text{---} & \text{---} & \text{---} & \text{---} \\ \text{---} & \text{---} & \text{---} & \text{---} & \text{---} \\ \text{---} & \text{---} & \text{---} & \text{---} & \text{---} \\ \text{---} & \text{---} & \text{---} & \text{---} & \text{---} \end{bmatrix} \quad (5.7)$$

which can be transformed to a block-diagonal matrix using row and column permutations. Define the permutation matrices \mathbf{P}_1 and \mathbf{P}_2 whose encoding vectors $p_1(k)$ and $p_2(k)$ are given by

$$p_1(k) = \left\lfloor \frac{k}{M} \right\rfloor + N((k - \delta) \bmod M) \quad (5.8)$$

$$p_2(k) = l(N - 1) + (-1)^l \left\lfloor \frac{k}{M} \right\rfloor + N((k - \delta) \bmod M) \quad (5.9)$$

where $l = (k + \delta) \bmod 2$ and $\delta = (1 - \left\lfloor \frac{k}{MN/2} \right\rfloor)$, with $\lfloor x \rfloor$ being the integer part of x and $y \bmod x$ being the remainder. The matrix $\mathbf{P}_2 \mathbf{H} \mathbf{P}_1$ is block-diagonal

$$\mathbf{P}_2 \mathbf{H} \mathbf{P}_1 = \begin{bmatrix} \mathbf{D}_0 & & & \\ & \mathbf{D}_1 & & \\ & & \ddots & \\ & & & \mathbf{D}_{N-1} \end{bmatrix} \quad (5.10)$$

with $M \times M$ blocks $\mathbf{D}_n, n = 0, \dots, N-1$. Each \mathbf{D}_n is also a block-diagonal matrix

$$\mathbf{D}_n = \begin{bmatrix} \mathbf{d}_n & & & \\ & \mathbf{d}_n & & \\ & & \ddots & \\ & & & \mathbf{d}_n \end{bmatrix} \quad \text{for } n = 0, \dots, N-1 \quad (5.11)$$

where \mathbf{d}_n are a 2×2 matrices given by

$$\mathbf{d}_n \triangleq \begin{cases} \begin{bmatrix} h(N-n-1) & h(-n-1) \\ h(N+n) & h(n) \end{bmatrix} & \text{for } n = 0, \dots, N/2-1 \\ \begin{bmatrix} h(n) & h(n-N) \\ h(2N-n-1) & h(N-n-1) \end{bmatrix} & \text{for } n = N/2, \dots, N-1 \end{cases} \quad (5.12)$$

In this case

$$\begin{aligned} \mathbf{H} &= \mathbf{P}_2^T \mathbf{P}_2 \mathbf{H} \mathbf{P}_1 \mathbf{P}_1^T \\ \mathbf{H} &= \mathbf{P}_2^T (\text{diag}(\mathbf{D}_0, \mathbf{D}_1, \dots, \mathbf{D}_{N-1})) \mathbf{P}_1^T \end{aligned} \quad (5.13)$$

and

$$\begin{aligned} \mathbf{H}^{-1} &= \mathbf{P}_1 (\mathbf{P}_2 \mathbf{H} \mathbf{P}_1)^{-1} \mathbf{P}_2 \\ \mathbf{H}^{-1} &= \mathbf{P}_1 (\text{diag}(\mathbf{D}_0, \mathbf{D}_1, \dots, \mathbf{D}_{N-1}))^{-1} \mathbf{P}_2 \\ \mathbf{H}^{-1} &= \mathbf{P}_1 (\text{diag}(\mathbf{D}_0^{-1}, \mathbf{D}_1^{-1}, \dots, \mathbf{D}_{N-1}^{-1})) \mathbf{P}_2 \\ \mathbf{H}^{-1} &= \left(\mathbf{P}_2^T \left(\text{diag} \left((\mathbf{D}_0^{-1})^T, (\mathbf{D}_1^{-1})^T, \dots, (\mathbf{D}_{N-1}^{-1})^T \right) \right) \mathbf{P}_1^T \right)^T \end{aligned} \quad (5.14)$$

Since the inverse of a block-diagonal matrix is also a block-diagonal matrix with the same dimension, it follows that \mathbf{D}_n^{-1} is, as \mathbf{D}_n , a block-diagonal matrix with 2×2 blocks. As a

consequence, from (5.13) and (5.14), \mathbf{H}^{-1} has the transpose structure of \mathbf{H} (5.7), i.e.,

$$\mathbf{H}^{-1} = \begin{bmatrix} \diagup & & & \\ & \diagdown & & \\ & & \diagup & \\ & & & \diagdown \\ & & & & \diagup \\ & & & & & \diagdown \\ & & & & & & \diagup \\ & & & & & & & \diagdown \\ & & & & & & & & \diagup \\ & & & & & & & & & \diagdown \end{bmatrix} \quad (5.15)$$

The diagonal, or anti-diagonal, elements from each block in any block-row of \mathbf{H}^{-1} comprise the biorthogonal function which has only $2N$ non zero elements. This illustrates why the truncation of the window to a length of $2N$ gives a biorthogonal function which has also a length of exactly $2N$ ■

Theorem 5.2

The necessary and sufficient conditions on the window function $h(n)$ so that it leads to an orthogonal transform are

$$\left\{ \begin{array}{l} h(n) = \pm h(N - n - 1) \\ h(N + n) = \mp h(-n - 1) \\ [h(n)]^2 = 1 - [h(N + n)]^2 \\ h(n) = 0 \quad \text{for } n \notin \left[-\frac{N}{2}, \frac{3N}{2}\right] \end{array} \right\} \quad (5.16)$$

Proof. To have orthogonal transform, the transformation matrix $[\mathbf{HC}]$, must be orthogonal.

- Since the matrix \mathbf{C} (5.5) is orthogonal, then $[\mathbf{HC}]$ is orthogonal *iff* \mathbf{H} (5.4) is orthogonal.
- Since the matrices \mathbf{P}_1 (5.8) and \mathbf{P}_2 (5.9) are orthogonal, then the matrix \mathbf{H} is orthogonal *iff* $[\mathbf{P}_2\mathbf{H}\mathbf{P}_1]$ is orthogonal.
- Since the matrix $\mathbf{P}_2\mathbf{H}\mathbf{P}_1$ (5.10) is block-diagonal with $M \times M$ blocks \mathbf{D}_n , then the matrix $\mathbf{P}_2\mathbf{H}\mathbf{P}_1$ is orthogonal *iff* \mathbf{D}_n is orthogonal for all n .

- Since the matrix \mathbf{D}_n (5.11) is also a block-diagonal matrix with blocks \mathbf{d}_n , then the matrix \mathbf{D}_n is orthogonal *iff* \mathbf{d}_n is orthogonal.
- Now, the necessary and sufficient condition on \mathbf{d}_n (5.12) to be orthogonal is $\mathbf{d}_n \times \mathbf{d}_n^T = \mathbf{I}$,

$$\begin{bmatrix} h(N-n-1) & h(-n-1) \\ h(N+n) & h(n) \end{bmatrix} \begin{bmatrix} h(N-n-1) & h(N+n) \\ h(-n-1) & h(n) \end{bmatrix} = \begin{bmatrix} 1 & 0 \\ 0 & 1 \end{bmatrix}$$

for $n = 0, \dots, N/2 - 1$

$$\begin{bmatrix} h(n) & h(n-N) \\ h(2N-n-1) & h(N-n-1) \end{bmatrix} \begin{bmatrix} h(n) & h(2N-n-1) \\ h(n-N) & h(N-n-1) \end{bmatrix} = \begin{bmatrix} 1 & 0 \\ 0 & 1 \end{bmatrix}$$

for $n = N/2, \dots, N-1$

(5.17)

These two matrix equations (5.17) are satisfied *iff*

$$h(n) = \pm h(N-n-1)$$

$$h(N+n) = \mp h(-n-1)$$

$$[h(n)]^2 = 1 - [h(N+n)]^2$$

for $n = 0, \dots, N/2 - 1$. Under these conditions, \mathbf{H}^{-1} is given by

$$\begin{aligned} \mathbf{H}^{-1} &= \mathbf{P}_1 (\mathbf{P}_2 \mathbf{H} \mathbf{P}_1)^{-1} \mathbf{P}_2 \\ &= \mathbf{P}_1 (\mathbf{P}_2 \mathbf{H} \mathbf{P}_1)^T \mathbf{P}_2 \\ &= \mathbf{P}_1 \mathbf{P}_1^T \mathbf{H}^T \mathbf{P}_2 \mathbf{P}_2^T \\ &= \mathbf{H}^T \end{aligned}$$

and thus \mathbf{H} is orthogonal ■

According to the above theorem, if an orthogonal transform has to be obtained, we have, for each $n, n = 0, \dots, N/2 - 1$, *three* equations in the *four* unknowns $h(n), h(N + n), h(-n - 1), h(N - n - 1)$. This means that we have $N/2$ degrees of freedom which enable us to tailor the window function to satisfy the required characteristics.

Under the above conditions, the coefficient can be calculated using the matrix equation

$$\mathbf{a} = \mathbf{C} \mathbf{H}^T \mathbf{x} \quad (5.18)$$

The following steps are used to compute the m^{th} N coefficients

- Multiply the signal $x(k + mN)$ by the window function $h(k)$. Let the product be denoted by hx which is of length $2N$.
- Divide hx into 4 sections $\{hx_1, hx_2, hx_3, hx_4\}$ each of length $\frac{N}{2}$.
- flip⁶ hx_1 and hx_4 and call the result $\overleftarrow{hx_1}$ and $\overleftarrow{hx_4}$ respectively.
- Apply the N -point the DCT (3.15) to the vector $(hx_2 + \overleftarrow{hx_1} : hx_3 + \overleftarrow{hx_4})$, where $(x_1 : x_2)$ denotes the concatenation of the 2 vectors x_1 and x_2 .

For this algorithm, the multiplication of the signal $x(k + mN)$ by the window function $h(k)$ requires $2N$ multiplications for each m . Assuming that the N point DCT takes $\frac{N}{2} \log_2 N$ multiplications, a total of $2N + \frac{N}{2} \log_2 N$ multiplications is required for each m . Since there are M values of m , the calculation of transform coefficients requires only $L(2 + \frac{1}{2} \log_2 N)$ multiplications.

⁶ Flipping an N -dimensional vector α is performed by replacing the element α_i by α_{N-i+1} .

5.5 Results

In the previous section, we derived the conditions on the analysis window to be a candidate of the orthogonal Gabor-DCT transform (5.16). Two example which satisfy these conditions are plotted in Fig. 36 and 37.

We have the freedom to choose any $\frac{N}{2}$ of the $2N$ window values arbitrarily and the rest $\frac{3N}{2}$ values will be determined according to (5.16). In the first example, the Gaussian function

$$h(n) = \exp\left(\frac{-\pi}{2.27N^2} \left(n - \frac{N-1}{2}\right)^2\right)$$

was chosen for the interval $n = 0, \dots, \frac{N}{2} - 1$. Then, the conditions of (5.16) were applied to determine the remaining window values. This gives

$$h(n) = \begin{cases} -\sqrt{1 - \left(\exp\left(\frac{-\pi}{2.27N^2} \left(n + \frac{N+1}{2}\right)^2\right)\right)^2} & \text{for } n = -\frac{N}{2}, \dots, -1 \\ \exp\left(\frac{-\pi}{2.27N^2} \left(n - \frac{N-1}{2}\right)^2\right) & \text{for } n = 0, \dots, \frac{N}{2} - 1 \\ \exp\left(\frac{-\pi}{2.27N^2} \left(n - \frac{N-1}{2}\right)^2\right) & \text{for } n = \frac{N}{2}, \dots, N - 1 \\ \sqrt{1 - \left(\exp\left(\frac{-\pi}{2.27N^2} \left(n - \frac{3N-1}{2}\right)^2\right)\right)^2} & \text{for } n = N, \dots, \frac{3N}{2} - 1 \end{cases}$$

which is plotted in Fig. 36. In the second example, the function

$$h(n) = \exp\left(\frac{-\pi}{0.5665N^4} \left(n - \frac{N-1}{2}\right)^4\right)$$

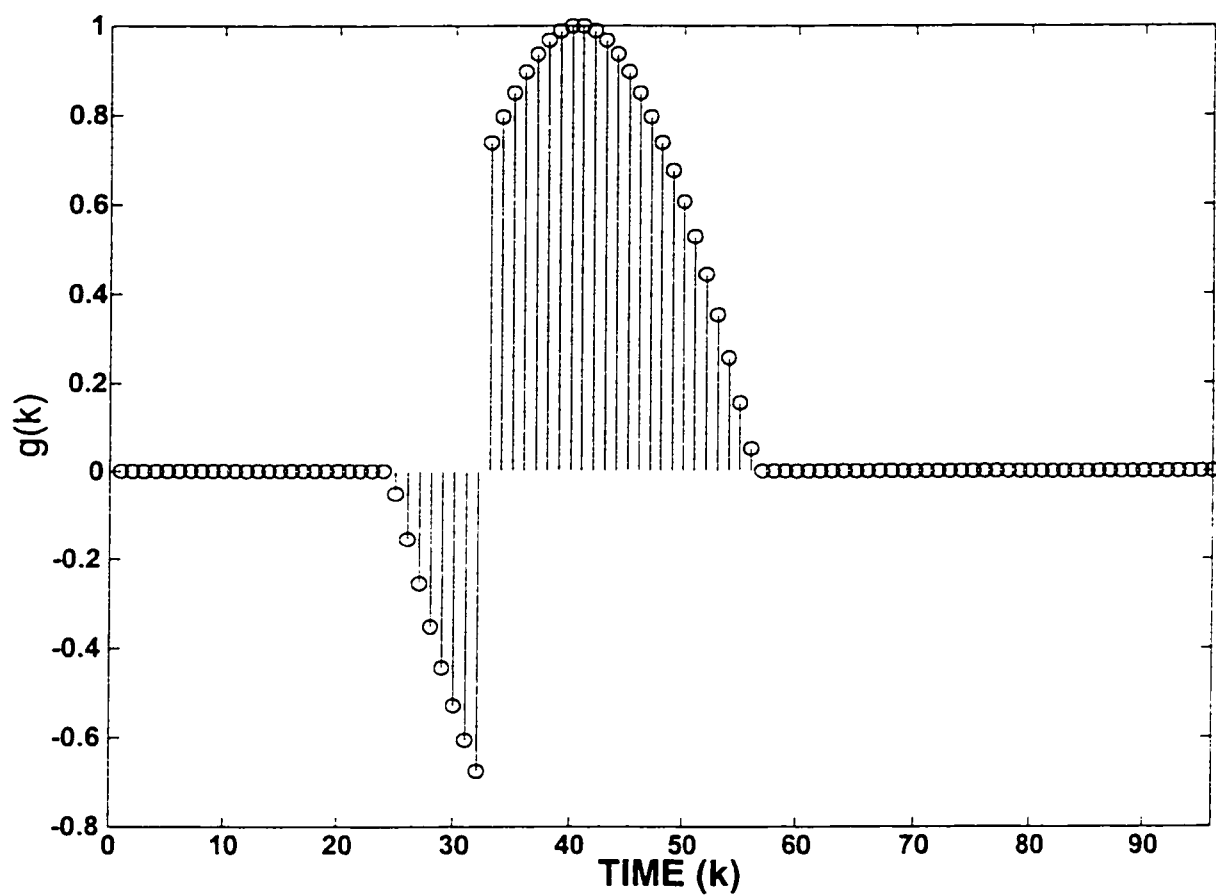


Figure 36: Example of a window function for the orthogonal Gabor-DCT, $M = N = 16$ and $m = 2$.

was used for the same interval as above. Then, the conditions of (5.16) were applied to determine the remaining window values. This gives

$$h(n) = \begin{cases} -\sqrt{1 - \left(\exp \left(\frac{-\pi}{0.5665N^4} \left(n + \frac{N+1}{2} \right)^4 \right) \right)^2} & \text{for } n = -\frac{N}{2}, \dots, -1 \\ \exp \left(\frac{-\pi}{0.5665N^4} \left(n - \frac{N-1}{2} \right)^4 \right) & \text{for } n = 0, \dots, \frac{N}{2} - 1 \\ \exp \left(\frac{-\pi}{0.5665N^4} \left(n - \frac{N-1}{2} \right)^4 \right) & \text{for } n = \frac{N}{2}, \dots, N-1 \\ \sqrt{1 - \left(\exp \left(\frac{-\pi}{0.5665N^4} \left(n - \frac{3N-1}{2} \right)^4 \right) \right)^2} & \text{for } n = N, \dots, \frac{3N}{2} - 1 \end{cases}$$

Accordingly, the window of Fig. 37 was obtained.

5.6 Conclusion

In this chapter we have developed an orthogonal Gabor Transform using the Discrete Cosine Transform. In addition to its nice stability property, the resulting transform is proven to be computationally attractive than any other currently available Gabor transforms. Compared to the Zak Transform based method, the computational saving ratio is $\frac{1+\log M + \frac{1}{2} \log_2 N}{2 + \frac{1}{2} \log_2 N}$. It is worthy to note that, this transform leads to an exact representation of the signal, i.e., using this transform leads to an exact reconstruction of the signal, and not just an approximation as is the case in [25]. The necessary and sufficient conditions for the analysis window to be a candidate of this orthogonal transform are derived. Two examples of this window are given.

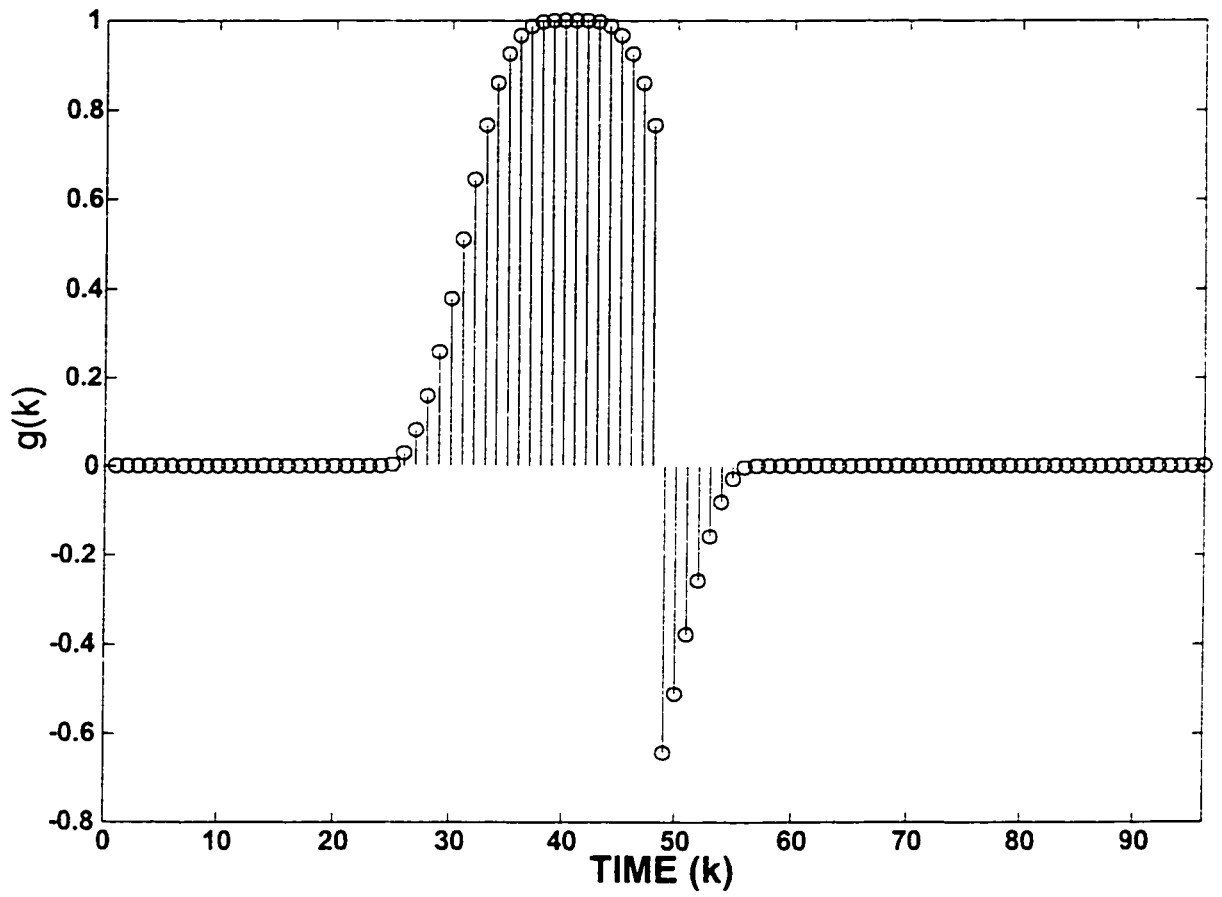


Figure 37: Another window function for the orthogonal Gabor-DCT, $M = N = 16$ and $m = 2$.

CHAPTER 6

STABLE CRITICALLY- SAMPLED JTF TRANSFORM WITH LOCALIZED BIORTHOGONAL FUNCTION

In this chapter, another new linear critical-sampling JTF transform is presented. Here, we concentrate on how to meet all the Universal JTF transform requirements simultaneously. The resulting transform, unlike all currently available Gabor transforms, leads to a *stable* transform. In addition, the resulting biorthogonal function, which is unique in the critical sampling case, is *well localized in both time and frequency*. It thus overcomes the main problems of the previous implementations. A fast algorithm to compute the biorthogonal function and the transform coefficients is presented. Also, an inherent characteristic of this implementation is that a truncated version of the modulating window of length $2N$, leads to a biorthogonal function with the same length. This biorthogonal function is proved to take, at most, $5N$ operations in its calculation irrespective of the signal length. Using this truncation results in an algorithm which gives an exact reconstruction of the signal.

6.1 Introduction

To solve the two problems of the critical-sampled Gabor transform, namely the instability and the nonlocalization of the biorthogonal function, many efforts have been made to replace the Gaussian window function by another suboptimal one to enhance the stability of the transform and/or enhance the biorthogonal function [20, 39], see also Chapter 5. Our objective in this chapter is to maintain the optimal Gaussian window function and choose other harmonic oscillation kernels to achieve better transform properties. We will show how adequate choice of the kernel can lead to a stable transform as well as a localized biorthogonal function in both time and frequency domains. Thus, our proposed technique solves the two major problems associated with Gabor transform.

The organization of the chapter is as follows. In Section 6.2, we develop the new transform and show that it gives a stable transform and that it is a good competitor, without any redundancy, to the over sampling solution. In Section 6.3, the resulting biorthogonal function is shown to be localized in both time and frequency domains. In Section 6.4, a fast method is given to calculate the biorthogonal function and the transform coefficients for the developed implementation. A practical implementation of the proposed transform based on a truncated version of the Gaussian function is given which is faster than any other implementation in the literature.

6.2 The Proposed Transform

Basically, Gabor transform expands time signals into a time and frequency shifts of an elementary function which is the modulation product of a window function by a harmonic oscillation like Fourier kernels. The aim of multiplying the harmonic oscillation by a window is to make the elementary function concentrated in time in addition to being already concentrated in frequency. Gabor defined two expansions. In the Complex Gabor expansion (2.14), Gabor chose the elementary functions to be

$$h_{m,n} = h(t - mT) \exp \frac{2i\pi nt}{T} \quad (6.1)$$

i.e., he chose the harmonic oscillation to be the well-known Fourier kernels. Consequently, the time-frequency plane is divided in the way illustrated in Fig. 11 where $a_{m,n}$ represents the projection of the signal on $h_{m,n}$ which is a shifted version of $h(t)$ in time by mT and in frequency by $\frac{n}{T}$. This expansion leads to the matrix \mathbf{H} as defined in (C-2) and (C-5) for periodic and nonperiodic case respectively. In the Real Gabor expansion (2.18), Gabor expanded the real signal into two real elementary functions

$$h_{m,n}^c = h(t - mT) \cos \frac{2\pi nt}{T} \quad (6.2)$$

$$h_{m,n}^s = h(t - mT) \sin \frac{2\pi(n + \frac{1}{2})t}{T} \quad (6.3)$$

in which he used the cosine and sine kernels to be the harmonic oscillation. Consequently, the time-frequency plane is divided in the way illustrated in Fig. 17 where $a_{m,n}$ and $b_{m,n}$

Head	$n' = 0$	$n' = 1$	$n' = 2$
$m' = 0$	1	0	.04 3214
$m' = 1$.45594	-.20788	.019703
$m' = 2$.04 3214	0	.001 8674

TABLE 4: Correlation between $h_{m,n}$ and $h_{m+m',n+n'}$ in the Real Gabor transform

represent the projection of the signal on $h_{m,n}^c$ and $h_{m,n}^s$ respectively. The implementation of [25] expands the real signal into a one real elementary function

$$h_{m,n} = h(t - mT) \cos \frac{\pi nt}{T} \quad (6.4)$$

and the time-frequency plane is divided as illustrated in Fig. 38 which leads to the matrix \mathbf{H} as defined in (C-8). It is to be noted that in all the above mentioned transforms, the elementary functions are correlated. The maximum correlation occurs between any two neighbor elementary functions in the time direction due to the tail of the window function outside the period T .

As an example, we calculated the correlation between the elementary functions for the last transform with $h(t)$ is a Gaussian window with $T/\sigma = 1$. The correlation between any two neighbor elementary functions in the time direction i.e., between $h_{m,n}$ and $h_{m+1,n}$ is equal to 0.4559 while the correlation between $h_{m,n}$ and $h_{m+2,n}$ reduces to 0.0432 since the tails of the Gaussian function approaches zero outside the period $2T$. In the frequency direction the correlation between $h_{m,n}$ and $h_{m,n+1}$ is zero. This is summarized in Table 4

It will be shown in what follows that by almost eliminating the correlation between the elementary function, the instability and the non-localization problems are solved.

In an effort to reduce the correlation, we exploit the orthogonality between Sine and

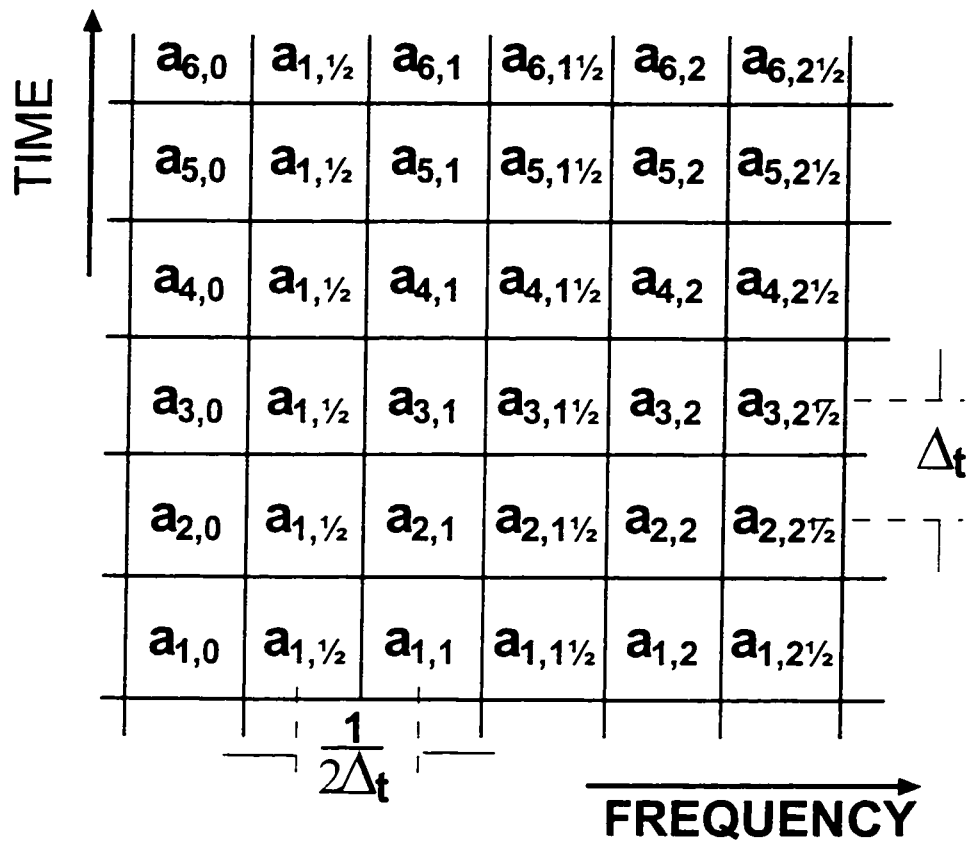


Figure 38: Expansion of a signal in cosine-type elementary signals.

Head	$n' = 0$	$n' = 1$	$n' = 2$
$m' = 0$	1	0	.04 3214
$m = 1$	0	0	0
$m = 2$.04 3214	0	.001 8674

TABLE 5: Correlation between $h_{m,n}$ and $h_{m+m',n+n'}$ in the new transform

Cosine function of the same frequency as follows. In the TF plane, we use alternate rows of two real elementary functions. One is the modulation product of the Gaussian function with the cosine kernel and the other is the modulation product of the Gaussian function with the sine kernel

$$\begin{matrix} h_{m,n}^{odd} \\ h_{m,n}^{even} \end{matrix} = h(t - mT) \begin{matrix} \cos \\ \sin \end{matrix} \frac{\pi \left(n + \frac{1}{2}\right) t}{T} \quad (6.5)$$

for odd and even m consequently as shown in Fig. 39. The correlations between these elementary functions, for Gaussian window with $T/\sigma = 1$, is indicated in Table 5. As shown in this table, the maximum correlation occurs between $h_{m,n}$ and $h_{m+2,n}$ which is equal to .04 3214. This means that we resolve the signal into an elementary functions that has a maximum correlation of 0.0432. which indicates that the elementary functions are almost orthogonal.

Yet, these two elementary functions are optimal in the sense that they occupy the minimal area in the JTF plane, that is $\frac{1}{2}$. As we will show, expanding the signal $x(t)$ into the above two elementary functions leads to a more stable transform.

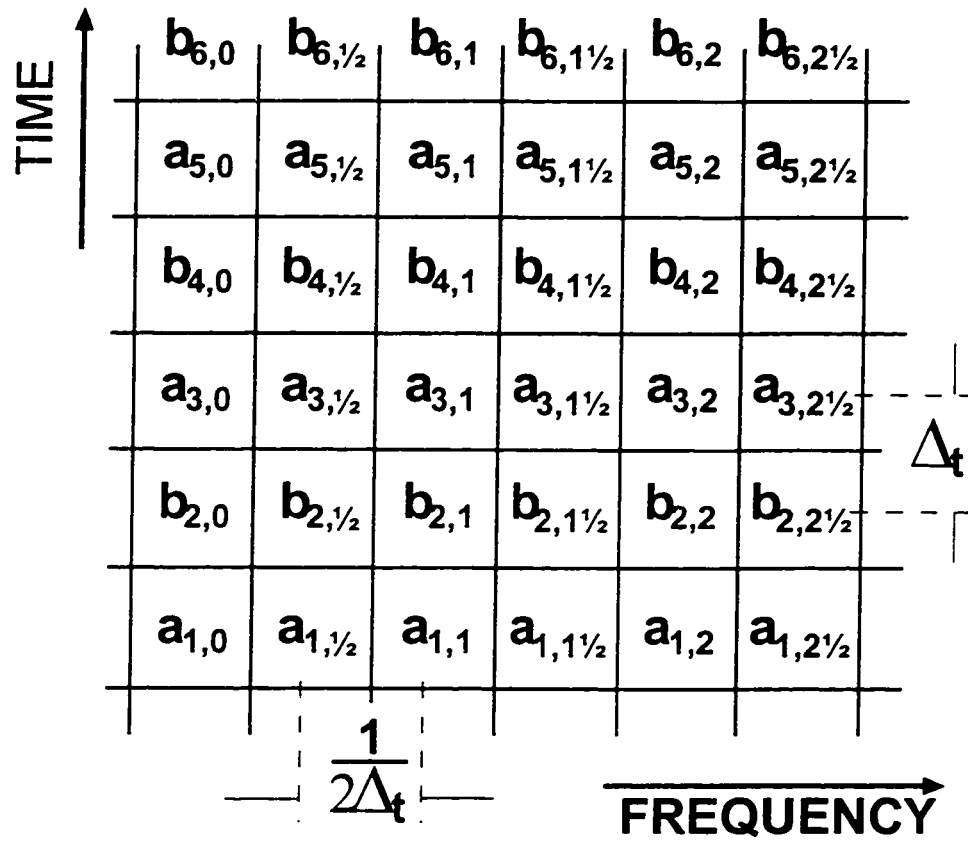


Figure 39: The new JTF distribution. $a_{n,m}$ belongs to $h_{m,n}^{even}(t)$ and $b_{n,m}$ belongs to $h_{m,n}^{odd}(t)$.

Expanding $x(t)$ into $\{h_{m,n}^{odd}, h_{m,n}^{even}\}_{m,n \in Z}$ leads to

$$x(t) = \sum_{\substack{m=-\infty \\ m=even}}^{m=\infty} h\left(t - \left(m + \frac{1}{2}\right)T\right) \sum_{n=0}^{n=\infty} a_{m,n} \cos \frac{\pi \left(n + \frac{1}{2}\right)t}{T} \\ + \sum_{\substack{m=-\infty \\ m=odd}}^{m=\infty} h\left(t - \left(m + \frac{1}{2}\right)T\right) \sum_{n=0}^{n=\infty} b_{m,n} \sin \frac{\pi \left(n + \frac{1}{2}\right)t}{T}$$

Let $x(k)$ be the periodized and sampled version of the continuous signal $x(t)$ with period L . The Transform coefficients of $x(k)$ will be periodic in time with period M and periodic in frequency with period N . Thus, the transform is reduced to discrete linear mapping that relates the periodic L samples of $x(k)$ to a periodic $M \times N$ array of transform coefficients. Thus,

$$x(k) = \sum_{\substack{m=0 \\ m=even}}^{M-1} h_m(k) \sum_{n=0}^{N-1} a_{m,n} \sqrt{\frac{2}{N}} \cos \left(\frac{\pi \left(k + \frac{1}{2}\right) \left(n + \frac{1}{2}\right)}{N} \right) \\ + \sum_{\substack{m=0 \\ m=odd}}^{M-1} h_m(k) \sum_{n=0}^{N-1} a_{m,n} \sqrt{\frac{2}{N}} \sin \left(\frac{\pi \left(k + \frac{1}{2}\right) \left(n + \frac{1}{2}\right)}{N} \right) \quad (6.6)$$

where $h_m(k)$ is

$$h_m(k) = h(k - mN) = h\left(t - \left(m + \frac{1}{2}\right)T\right) \Big|_{t=k} \quad (6.7)$$

To put (6.6) in matrix notation, note that

$$\begin{bmatrix} x(0) \\ x(1) \\ \vdots \\ x(N-1) \end{bmatrix} = \sum_{\substack{m=0 \\ m=even}}^{M-1} h_m(k) C \begin{bmatrix} a_{m,0} \\ a_{m,1} \\ \vdots \\ a_{m,N-1} \end{bmatrix} + \sum_{\substack{m=0 \\ m=odd}}^{M-1} h_m(k) S \begin{bmatrix} a_{m,0} \\ a_{m,1} \\ \vdots \\ a_{m,N-1} \end{bmatrix} \quad (6.8)$$

where $C = [c_{n,k}]_{N \times N}$ is the N point DCT-IV transform matrix with $c_{n,k}$ given by

$$c_{n,k} = \sqrt{\frac{2}{N}} \cos \frac{\pi (n + \frac{1}{2}) (k + \frac{1}{2})}{N} \quad n, k = 0, \dots, N-1 \quad (6.9)$$

and $S = [s_{n,k}]_{N \times N}$ is the N point DST-IV matrix with $s_{n,k}$ given by

$$s_{n,k} = \sqrt{\frac{2}{N}} \sin \frac{\pi (n + \frac{1}{2}) (k + \frac{1}{2})}{N} \quad n, k = 0, \dots, N-1 \quad (6.10)$$

Both C and S are orthogonal and symmetric i.e.,

$$C^{-1} = C^T = C$$

$$S^{-1} = S^T = S$$

Equation. (6.8) can be written as

$$\mathbf{x}_0 = \sum_{\substack{m=0 \\ m=\text{even}}}^{M-1} h_m(k) (C \mathbf{a}_m) + \sum_{\substack{m=0 \\ m=\text{odd}}}^{M-1} h_m(k) (S \mathbf{a}_m) \quad (6.11)$$

where a_m and x_m are as defined in (3.3) and (3.5), respectively. For $k = 0, 1, \dots, N-1$

$$\begin{aligned} x(k+N) = & \sum_{\substack{m=0 \\ m=\text{even}}}^{M-1} h_{m-1}(k) \sum_{n=0}^{N-1} a_{m,n} \sqrt{\frac{2}{N}} \cos \left(\frac{\pi ((k+N) + \frac{1}{2})(n + \frac{1}{2})}{N} \right) \\ & + \sum_{\substack{m=0 \\ m=\text{odd}}}^{M-1} h_{m-1}(k) \sum_{n=0}^{N-1} a_{m,n} \sqrt{\frac{2}{N}} \sin \left(\frac{\pi ((k+N) + \frac{1}{2})(n + \frac{1}{2})}{N} \right) \end{aligned} \quad (6.12)$$

Noting that, for $n, k = 0, \dots, N - 1$

$$\frac{\cos}{\sin} \left(\frac{\pi((k + N) + \frac{1}{2})(n + \frac{1}{2})}{N} \right) = \frac{-\cos}{+\sin} \left(\frac{\pi((N - 1 - k) + \frac{1}{2})(n + \frac{1}{2})}{N} \right) \quad (6.13)$$

Equation. (6.12) can be put in matrix notation as

$$\mathbf{x}_1 = - \sum_{\substack{m=0 \\ m=\text{even}}}^{M-1} h_{m-1}(k) (JC^T \mathbf{a}_m) + \sum_{\substack{m=0 \\ m=\text{odd}}}^{M-1} h_{m-1}(k) (JS^T \mathbf{a}_m) \quad (6.14)$$

Noting, also, that for $n, k = 0, \dots, N - 1$

$$\frac{\cos}{\sin} \left(\frac{\pi((k + 2N) + \frac{1}{2})(n + \frac{1}{2})}{N} \right) = \frac{-\cos}{-\sin} \left(\frac{\pi(k + \frac{1}{2})(n + \frac{1}{2})}{N} \right) \quad (6.15)$$

Thus, the equation

$$\begin{aligned} x(k + 2N) = & \sum_{\substack{m=0 \\ m=\text{even}}}^{M-1} h_{m-2}(k) \sum_{n=0}^{N-1} a_{m,n} \sqrt{\frac{2}{N}} \cos \left(\frac{\pi((k + 2N) + \frac{1}{2})(n + \frac{1}{2})}{N} \right) \\ & - \sum_{\substack{m=0 \\ m=\text{odd}}}^{M-1} h_{m-2}(k) \sum_{n=0}^{N-1} a_{m,n} \sqrt{\frac{2}{N}} \sin \left(\frac{\pi((k + 2N) + \frac{1}{2})(n + \frac{1}{2})}{N} \right) \end{aligned} \quad (6.16)$$

can be rewritten as

$$\mathbf{x}_2 = - \sum_{\substack{m=0 \\ m=\text{even}}}^{M-1} h_{m-2}(k) (C^T \mathbf{a}_m) - \sum_{\substack{m=0 \\ m=\text{odd}}}^{M-1} h_{m-2}(k) (S^T \mathbf{a}_m) \quad (6.17)$$

Similarly, one can show that

$$\mathbf{x}_3 = + \sum_{\substack{m=0 \\ m=even}}^{M-1} h_{m-3}(k) (JC^T \mathbf{a}_m) - \sum_{\substack{m=0 \\ m=odd}}^{M-1} h_{m-3}(k) (JS^T \mathbf{a}_m) \quad (6.18)$$

Based on (6.11), (6.14), (6.17) and (6.18), rewriting (6.6) in matrix form gives

$$\begin{bmatrix} \mathbf{x}_0 \\ \mathbf{x}_1 \\ \mathbf{x}_2 \\ \mathbf{x}_3 \\ \vdots \\ \mathbf{x}_{M-1} \end{bmatrix} = \begin{bmatrix} +H_0C & +H_{M-1}S & \cdots & +H_1S \\ -H_1JC & +H_0JS & \cdots & +H_2JS \\ -H_2C & -H_1S & \cdots & -H_3S \\ +H_3JC & -H_2JS & \cdots & -H_4JS \\ \vdots & \vdots & \ddots & \vdots \\ +H_{M-1}JC & -H_{M-1}JS & \cdots & -H_0JS \end{bmatrix} \cdot \begin{bmatrix} \mathbf{a}_0 \\ \mathbf{a}_1 \\ \mathbf{a}_2 \\ \mathbf{a}_3 \\ \vdots \\ \mathbf{a}_{M-1} \end{bmatrix}$$

where H_m is as defined in (3.6). The above equation can be written as

$$\mathbf{x} = \mathbf{H} \mathbf{E} \mathbf{a} \quad (6.19)$$

where \mathbf{a} and \mathbf{x} are as defined in (3.2) and (3.4), respectively, with

$$\mathbf{E} = \begin{bmatrix} C & & & & & \\ & S & & & & \\ & & -C & & & \\ & & & -S & & \\ & & & & \ddots & \\ & & & & & C \\ & & & & & & S \end{bmatrix} \quad (6.20)$$

and

$$\mathbf{H} = \begin{bmatrix} +H_0 & +H_{M-1} & -H_{M-2} & \cdots & +H_1 \\ -H_1J & +H_0J & +H_{M-1}J & \cdots & +H_2J \\ -H_2 & -H_1 & +H_0 & \cdots & -H_3 \\ +H_3J & -H_2J & -H_1 & \cdots & -H_4J \\ \vdots & \vdots & \vdots & \ddots & \vdots \\ +H_{M-1}J & -H_{M-2}J & -H_{M-3}J & \cdots & -H_0J \end{bmatrix} \quad (6.21)$$

If we ignore the J matrix, the matrix \mathbf{H} is block-circulant matrix. Thus, we call the matrix \mathbf{H} the generalized block-circulant. Equation (6.19) is the synthesis transform in matrix notation. Its inverse, i.e., the analysis transform, is

$$\mathbf{a} = \mathbf{E}^{-1} \mathbf{H}^{-1} \mathbf{x}$$

Since the matrix \mathbf{E} is orthogonal and symmetric, i.e., $\mathbf{E}^{-1} = \mathbf{E}$, then

$$\mathbf{a} = \mathbf{E} \mathbf{H}^{-1} \mathbf{x} \quad (6.22)$$

To show the stability of this implementation compared with other critical-sampling implementations, we calculate the condition number $\kappa(\mathbf{H}\mathbf{E})$ for typical values of M and N . The results are in Table 6. It is worth noting that while the condition number increases unboundedly with increasing N in all previous methods it converges to 1.19 in the proposed transform for very large values of N and M . This indicates that the proposed transform is stable and is very close to be orthogonal. Note that orthogonal matrices have condition number equal to *one* exactly. Table 7 gives a comparison between the proposed transform and the over-sampling solution. The proposed implementation outperforms the over-sampling

(N, M)	Complex		Real		Proposed
	Periodic	Aperiodic	Periodic	Aperiodic	
(8, 32)	12.37	11.34	12.37	12.33	1.18
(16, 16)	24.63	14.42	24.63	24.30	1.19
(16, 32)	24.63	19.38	24.63	24.54	1.19
(32, 16)	49.20	18.52	49.20	48.55	1.19
(32, 32)	49.20	28.77	49.20	49.02	1.19
(64, 64)	98.37	57.43	98.37	98.28	1.19
(128, 64)	196.74	73.64	196.74	196.55	1.19
(256, 128)	393.46	147.05	393.46	393.37	1.19

TABLE 6: Condition number of the proposed method compared to critically-sampled Gabor Transforms

(N, M)	OVSR=4	Proposed
(8, 32)	1.4	1.18
(16, 16)	1.47	1.19
(32, 32)	1.50	1.19
(64, 64)	1.52	1.19
(256, 128)	1.54	1.19

TABLE 7: Condition number of the proposed transform compared to the over-sampled gabor Transform

solution regarding stability without any of the redundancies of the over-sampling solution.

In the next section, the resulting biorthogonal function will be studied in detail.

6.3 The Resulting Biorthogonal Function

If the set of the elementary functions $\{h_{m,n}\}_{m,n \in \mathbb{Z}}$ is *linearly independent* and *complete*, there will exist a *dual (biorthogonal)* set $\{\gamma_{m,n}\}_{m,n \in \mathbb{Z}}$ such that the expansion coefficients can be computed by some regular inner product [1], such as

$$a_{m,n} \triangleq \langle \mathbf{x}, \gamma_{m,n}^* \rangle = \sum_k x[k] \gamma_{m,n}^*[k] \quad (6.23)$$

In the proposed transform, $a_{m,n}$ will be

$$a_{m,n} = \begin{cases} \sum_{k=0}^{L-1} \sqrt{\frac{2}{N}} x(k) \gamma_m(k) \cos\left(\frac{\pi(k+\frac{1}{2})(n+\frac{1}{2})}{N}\right) & m \text{ even} \\ \sum_{k=0}^{L-1} \sqrt{\frac{2}{N}} x(k) \gamma_m(k) \sin\left(\frac{\pi(k+\frac{1}{2})(n+\frac{1}{2})}{N}\right) & m \text{ odd} \end{cases}$$

where $\gamma_m(k) = \gamma(k - mN)$.

For even m ,

$$a_{m,n} = \sum_{k=0}^{L-1} \sqrt{\frac{2}{N}} x(k) \gamma_m(k) \cos\left(\frac{\pi(k+\frac{1}{2})(n+\frac{1}{2})}{N}\right)$$

$$a_{m,n} = \left\{ \begin{array}{l} \sum_{k=0}^{N-1} \sqrt{\frac{2}{N}} x(k) \gamma_m(k) \cos\left(\frac{\pi(k+\frac{1}{2})(n+\frac{1}{2})}{N}\right) \\ + \sum_{k=N}^{2N-1} \sqrt{\frac{2}{N}} x(k) \gamma_m(k) \cos\left(\frac{\pi(k+\frac{1}{2})(n+\frac{1}{2})}{N}\right) \\ + \sum_{k=2N}^{3N-1} \sqrt{\frac{2}{N}} x(k) \gamma_m(k) \cos\left(\frac{\pi(k+\frac{1}{2})(n+\frac{1}{2})}{N}\right) \\ + \sum_{k=3N}^{4N-1} \sqrt{\frac{2}{N}} x(k) \gamma_m(k) \cos\left(\frac{\pi(k+\frac{1}{2})(n+\frac{1}{2})}{N}\right) \\ + \dots \end{array} \right. \quad (6.24)$$

The above equation can be written as

$$a_{m,n} = \left\{ \begin{array}{l} \sum_{k=0}^{N-1} \sqrt{\frac{2}{N}} x(k) \gamma_m(k) \cos\left(\frac{\pi(k+\frac{1}{2})(n+\frac{1}{2})}{N}\right) \\ + \sum_{k=0}^{N-1} \sqrt{\frac{2}{N}} x(k+N) \gamma_{m-1}(k) \cos\left(\frac{\pi((k+N)+\frac{1}{2})(n+\frac{1}{2})}{N}\right) \\ + \sum_{k=0}^{N-1} \sqrt{\frac{2}{N}} x(k+2N) \gamma_{m-2}(k) \cos\left(\frac{\pi((k+2N)+\frac{1}{2})(n+\frac{1}{2})}{N}\right) \\ + \sum_{k=0}^{N-1} \sqrt{\frac{2}{N}} x(k+3N) \gamma_{m-3}(k) \cos\left(\frac{\pi((k+3N)+\frac{1}{2})(n+\frac{1}{2})}{N}\right) \\ + \dots \end{array} \right. \quad (6.25)$$

Similar to the above steps of Section 6.2 and depending on the DCT properties (6.13) and (6.15), the above equation can be put in matrix formulation, for $n = 0, 1, \dots, N-1$, as

$$\mathbf{a}_m = C (\Gamma_0 \mathbf{x}_0 - J \Gamma_1 \mathbf{x}_1 - \Gamma_2 \mathbf{x}_2 + J \Gamma_3 \mathbf{x}_3 + \dots + J \Gamma_{M-1} \mathbf{x}_{M-1})$$

where $\Gamma_m = \text{diag}(\gamma_m(0), \gamma_m(1), \dots, \gamma_m(N-1))$. Similarly, for odd m , and depending on the DST properties (6.13) and (6.15)

$$\mathbf{a}_m = S(\Gamma_0 \mathbf{x}_0 + J\Gamma_1 \mathbf{x}_1 - \Gamma_2 \mathbf{x}_2 - J\Gamma_3 \mathbf{x}_3 + \dots - J\Gamma_{M-1} \mathbf{x}_{M-1})$$

Thus, for $m = 0, 1, \dots, M-1$

$$\begin{bmatrix} \mathbf{a}_1 \\ \mathbf{a}_2 \\ \vdots \\ \mathbf{a}_M \end{bmatrix} = \begin{bmatrix} C\Gamma_0 & -CJ\Gamma_1 & -C\Gamma_2 & CJ\Gamma_3 & \cdots & CJ\Gamma_{M-1} \\ S\Gamma_{M-1} & SJ\Gamma_0 & -S\Gamma_1 & -SJ\Gamma_2 & \cdots & -SJ\Gamma_{M-2} \\ \vdots & \vdots & \vdots & \vdots & \ddots & \vdots \\ S\Gamma_1 & SJ\Gamma_2 & -S\Gamma_3 & -SJ\Gamma_4 & \cdots & -SJ\Gamma_0 \end{bmatrix} \begin{bmatrix} \mathbf{x}_1 \\ \mathbf{x}_2 \\ \vdots \\ \mathbf{x}_M \end{bmatrix} \quad (6.26)$$

which can be rewritten as

$$\mathbf{a} = \mathbf{E}\Gamma \mathbf{x} \quad (6.27)$$

where \mathbf{a} , \mathbf{E} , and \mathbf{x} are as defined in (3.2), (6.20), and (3.4), respectively. The matrix Γ is given by

$$\Gamma = \begin{bmatrix} +\Gamma_0 & -J\Gamma_1 & -\Gamma_2 & +J\Gamma_3 & \cdots & +J\Gamma_{M-1} \\ +\Gamma_{M-1} & +J\Gamma_0 & -\Gamma_1 & -J\Gamma_2 & \cdots & -J\Gamma_{M-2} \\ -\Gamma_{M-2} & +J\Gamma_{M-1} & +\Gamma_0 & -J\Gamma_1 & \cdots & -J\Gamma_{M-3} \\ -\Gamma_{M-3} & -J\Gamma_{M-2} & +\Gamma_{M-1} & +J\Gamma_0 & \cdots & +J\Gamma_{M-4} \\ \vdots & \vdots & \vdots & \vdots & \ddots & \vdots \\ -\Gamma_1 & -J\Gamma_2 & +\Gamma_3 & +J\Gamma_4 & \cdots & +J\Gamma_0 \end{bmatrix} \quad (6.28)$$

Noting the similarity between (6.22) and (6.27), the relation between \mathbf{H}^{-1} and Γ is what

remains to be established. The matrix \mathbf{H} (6.21) has the special structure to be referred to as "zigzag structure". In the following theorem, we prove that its inverse has also another special structure which is the transpose of this zigzag structure.

Theorem 6.1

Let \mathbf{A} be an $MN \times MN$ block matrix with each block being $N \times N$ diagonal or anti-diagonal matrix according to the zigzag structure

$$\mathbf{A} = \left[\begin{array}{c} \text{Zigzag pattern of } N \times N \text{ blocks} \end{array} \right]$$

The inverse matrix, \mathbf{A}^{-1} , has a structure which is the transpose of zigzag structure of, \mathbf{A} , i.e.,

$$\mathbf{A}^{-1} = \left[\begin{array}{c} \text{Transposed zigzag pattern of } N \times N \text{ blocks} \end{array} \right]$$

Proof. The zigzag structured matrix \mathbf{A} can be transformed into block-diagonal matrix via row column permutation. To do so, define a permutation $MN \times MN$ matrices \mathbf{P}_1 and \mathbf{P}_2 whose MN encoding vector p_1 and p_2 are given by

$$p_1(k) = \left\lfloor \frac{k}{M} \right\rfloor + N(k \bmod M) \quad (6.29)$$

$$p_2(k) = l(N-1) + (-1)^l \left\lfloor \frac{k}{M} \right\rfloor + N(k \bmod M) \quad (6.30)$$

where

- $k = 0, \dots, MN - 1,$
- $l = k \bmod 2,$
- $\left\lfloor \frac{x}{y} \right\rfloor$ is the integer part of x/y
- $(y \bmod x)$ is the remainder of x/y .

The matrix $[\mathbf{P}_2 \mathbf{A} \mathbf{P}_1]$ is a block-diagonal matrix

$$\mathbf{P}_2 \mathbf{A} \mathbf{P}_1 = \text{diag} (\mathbf{D}_0, \mathbf{D}_1, \dots, \mathbf{D}_{N-1}) \quad (6.31)$$

where \mathbf{D}_n is $M \times M$ matrix which is, in general, full matrix. Since \mathbf{P}_1 and \mathbf{P}_2 are orthogonal,

$$\begin{aligned} \mathbf{A} &= \mathbf{P}_2^T \mathbf{P}_2 \mathbf{A} \mathbf{P}_1 \mathbf{P}_1^T \\ &= \mathbf{P}_2^T (\text{diag} (\mathbf{D}_0, \mathbf{D}_1, \dots, \mathbf{D}_{N-1})) \mathbf{P}_1^T \end{aligned} \quad (6.32)$$

In this case the inverse, \mathbf{A}^{-1} , is given by

$$\begin{aligned} \mathbf{A}^{-1} &= \mathbf{P}_1 (\mathbf{P}_2 \mathbf{A} \mathbf{P}_1)^{-1} \mathbf{P}_2 \\ \mathbf{A}^{-1} &= \mathbf{P}_1 (\text{diag} (\mathbf{D}_0, \mathbf{D}_1, \dots, \mathbf{D}_{N-1}))^{-1} \mathbf{P}_2 \\ \mathbf{A}^{-1} &= \mathbf{P}_1 (\text{diag} (\mathbf{D}_0^{-1}, \mathbf{D}_1^{-1}, \dots, \mathbf{D}_{N-1}^{-1})) \mathbf{P}_2 \\ \mathbf{A}^{-1} &= \left(\mathbf{P}_2^T \left(\text{diag} \left((\mathbf{D}_0^{-1})^T, (\mathbf{D}_1^{-1})^T, \dots, (\mathbf{D}_{N-1}^{-1})^T \right) \right) \mathbf{P}_1^T \right)^T \end{aligned} \quad (6.33)$$

Comparing (6.33) with (6.32) and since $(\mathbf{D}_n^{-1})^T$ is also $M \times M$ full matrix, the inverse matrix \mathbf{A}^{-1} has the transpose structure of \mathbf{A} ■

From (6.21), the matrix \mathbf{H} , in addition to having a zigzag structure, is generalized block-circulant

Corollary 6.1

The inverse of the generalized block-circulant matrix \mathbf{H} is also generalized block-circulant.

Proof. From (6.32),

$$\mathbf{H} = \mathbf{P}_2^T (\text{diag}(\mathbf{D}_0, \mathbf{D}_1, \dots, \mathbf{D}_{N-1})) \mathbf{P}_1^T \quad (6.34)$$

\mathbf{D}_n in case of generalized block-circulant matrices, \mathbf{H} , is a block-circulant matrix with 2×2 blocks. Hence, its inverse, \mathbf{D}_n^{-1} , is also block-circulant matrix with 2×2 blocks [40]. Thus from (6.33), \mathbf{H}^{-1} is also generalized block-circulant ■

Thus by Theorem 6.1 and its corollary, we have proved that the inverse of \mathbf{H} has the structure

$$\mathbf{H}^{-1} = \begin{bmatrix} \Lambda_0 & J\Lambda_1 & \Lambda_2 & J\Lambda_3 & \cdots & J\Lambda_{M-1} \\ \Lambda_{M-1} & J\Lambda_0 & \Lambda_1 & J\Lambda_2 & \cdots & J\Lambda_{M-2} \\ \vdots & \vdots & \vdots & \vdots & \ddots & \vdots \\ \Lambda_1 & J\Lambda_2 & \Lambda_3 & J\Lambda_4 & \cdots & J\Lambda_0 \end{bmatrix} \quad (6.35)$$

where Λ_m is diagonal $N \times N$ matrix given by

$$\Lambda_m = \text{diag}(\lambda(mN), \lambda(mN+1), \dots, \lambda(mN+N-1)) \quad (6.36)$$

Comparing (6.35) and (6.28), it follows that

$$\Gamma_m = (-1)^{\lfloor \frac{m+1}{2} \rfloor} \cdot \Lambda_m \quad (6.37)$$

Thus, the biorthogonal function $\gamma(k)$ is

$$\gamma(k) = (-1)^q \cdot \lambda(k) \quad (6.38)$$

where

$$q = \left\lfloor \frac{\lfloor k/N \rfloor + 1}{2} \right\rfloor$$

For the Gaussian window, the resulting biorthogonal function is plotted in Fig. 40 for $M = N = 8$, and $\sigma = N$. This figure shows the good concentration of the resulting biorthogonal function in both time and frequency. The following example is given to illustrate the effects of this biorthogonal function on the performance of the transform.

Example 6.1

The same signal of example 4.1 was plotted in the JTF domain in Fig. 41 using the above JTF transform. Comparing Fig. 41 with Figures 33, 32, 33, and 32, it is obvious that the above transform gives the most distinctive representation (specially in the frequency direction).

6.4 Practical Calculation of the Transform Coefficients

Using equations (6.22) and (6.19) directly to calculate the transform coefficients is impractical. equations (6.22) and (6.19) involves inversion of the $L \times L$ matrix \mathbf{H} which takes $\mathcal{O}(L^3)$ and a multiplication of an $L \times L$ matrix \mathbf{H} , or \mathbf{H}^{-1} , by a vector of length L which takes $\mathcal{O}(L^2)$. In the following subsections, we show how to perform these operations with considerable computational saving by exploiting the special structure of these matrices.

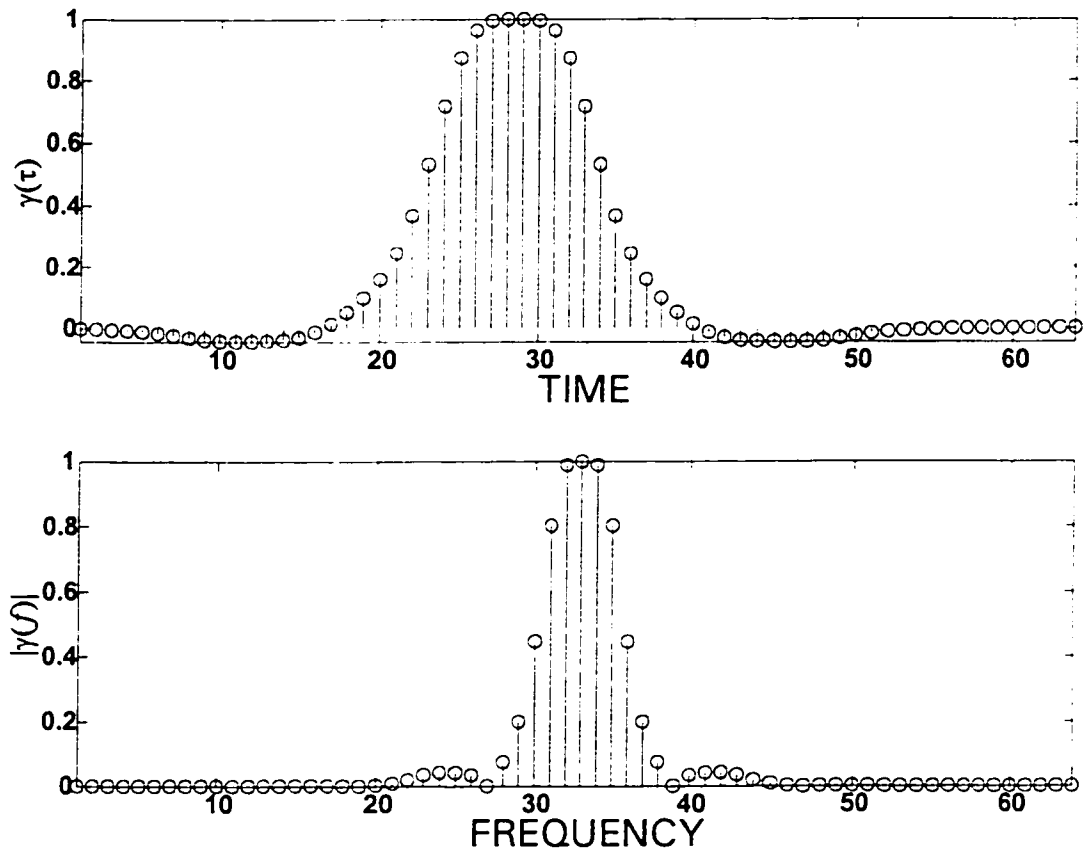


Figure 40: The biorthogonal function of the proposed transform.

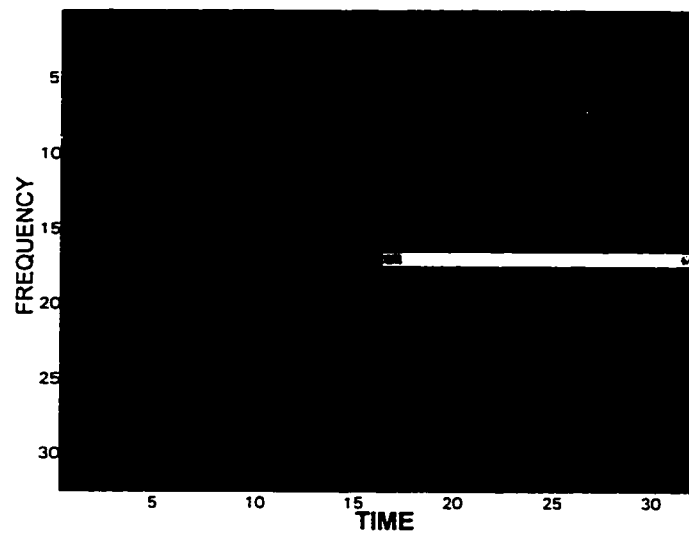


Figure 41: JTF representation of the test signal using the proposed transform.

6.4.1 Calculation of \mathbf{H}^{-1}

The matrix \mathbf{H} is an $MN \times MN$ matrix (6.21) which is very costly to invert. \mathbf{H} can be transformed into block-diagonal matrix via row column permutation as has been shown in Theorem 6.1. The matrix $\mathbf{P}_2 \mathbf{H} \mathbf{P}_1 = \text{diag}(\mathbf{D}_0, \mathbf{D}_1, \dots, \mathbf{D}_{N-1})$ is a block-diagonal matrix. Therefore, each \mathbf{D}_n can be inverted separately. \mathbf{D}_n is $M \times M$ block-circulant matrix with 2×2 blocks $D_{n,m'}$, for $m' = 0, 1, \dots, \frac{M}{2} - 1$. That is,

$$\mathbf{D}_n = \begin{pmatrix} D_{n,0} & D_{n,M/2-1} & \cdots & D_{n,1} \\ D_{n,1} & D_{n,0} & \cdots & D_{n,2} \\ \vdots & \vdots & \ddots & \vdots \\ D_{n,M/2-1} & D_{n,M/2-2} & \cdots & D_{n,0} \end{pmatrix} \quad (6.39)$$

\mathbf{D}_n can be converted to block-diagonal matrices \mathbf{B}_n by

$$\begin{aligned} \mathbf{B}_n &= (E_{M/2} \otimes I_2) \cdot \mathbf{D}_n \cdot (E_{M/2} \otimes I_2)^T \\ &= \text{diag}(B_{n,0}, B_{n,1}, \dots, B_{n,M/2-1}) \end{aligned} \quad (6.40)$$

where

- $B_{n,m'}$ is a 2×2 matrix
- \otimes is the Kronecker tensor product
- I_2 is the identity matrix of size 2×2
- E_N is the N -point Discrete Fourier Transform matrix defined in (B-1a).

This is a simplified form of Theorem 5.6.4 of [40], in which we discarded the unnecessary operations. Since \mathbf{B}_n is a block-diagonal matrix with 2×2 blocks, its inversion reduces to

an $\frac{M}{2}$ inversions of 2×2 matrices $B_{n,m'}$. Therefore, the inverse of D_n is given by

$$\begin{aligned} D_n^{-1} &= (E_{M/2} \otimes I_2)^T \cdot B_n^{-1} \cdot (E_{M/2} \otimes I_2) \\ D_n^{-1} &= (E_{M/2} \otimes I_2)^T \begin{bmatrix} B_{n,0}^{-1} & & & \\ & B_{n,1}^{-1} & & \\ & & \ddots & \\ & & & B_{n,M/2-1}^{-1} \end{bmatrix} (E_{M/2} \otimes I_2) \end{aligned} \quad (6.41)$$

There is more efficient way to calculate the inverse of D_n , than using (6.40) and (6.41) to calculate B_n and D_n^{-1} , Alternatively, one can calculate the $\{B_{n,0}, B_{n,1}, \dots, B_{n,M/2-1}\}$ directly using

$$\begin{bmatrix} B_{n,0} \\ B_{n,1} \\ \vdots \\ B_{n,M/2-1} \end{bmatrix} = \sqrt{m'} (E_{M/2} \otimes I_2) \begin{bmatrix} D_{n,0} \\ D_{n,1} \\ \vdots \\ D_{n,M/2-1} \end{bmatrix} \quad (6.42)$$

and

$$\begin{bmatrix} ID_{n,0} \\ ID_{n,1} \\ \vdots \\ ID_{n,M/2-1} \end{bmatrix} = \frac{1}{\sqrt{m'}} (E_{M/2} \otimes I_2)^T \begin{bmatrix} B_{n,0}^{-1} \\ B_{n,1}^{-1} \\ \vdots \\ B_{n,M/2-1}^{-1} \end{bmatrix} \quad (6.43)$$

D_n^{-1} can be directly obtained as

$$D_n^{-1} = \begin{pmatrix} ID_{n,0} & ID_{n,M/2-1} & \cdots & ID_{n,1} \\ ID_{n,1} & ID_{n,0} & \cdots & ID_{n,2} \\ \vdots & \vdots & \ddots & \vdots \\ ID_{n,M/2-1} & ID_{n,M/2-2} & \cdots & ID_{n,0} \end{pmatrix} \quad (6.44)$$

Equation (6.42) can be more simplified as follows. The $M \times M$ matrix $(E_{M/2} \otimes I_2)$ can be converted to block-diagonal matrix with $\frac{M}{2} \times \frac{M}{2}$ blocks using the permutation matrix P_3

whose encoding vector is given by

$$p_3(m) = \left\lfloor \frac{m}{M/2} \right\rfloor + 2(m \bmod M/2) \quad (6.45)$$

where $m = 0, 1, \dots, M - 1$. Using this permutation matrix leads to

$$\mathbf{P}_3 (E_{M/2} \otimes I_2) \mathbf{P}_3^T = \begin{bmatrix} E_{M/2} & \\ & E_{M/2} \end{bmatrix} \quad (6.46)$$

Thus, (6.42) will be

$$\begin{bmatrix} B_{n,0} \\ B_{n,1} \\ \vdots \\ B_{n,M/2-1} \end{bmatrix} = \sqrt{m'} \mathbf{P}_3^T \begin{bmatrix} E_{M/2} & \\ & E_{M/2} \end{bmatrix} \mathbf{P}_3 \begin{bmatrix} D_{n,0} \\ D_{n,1} \\ \vdots \\ D_{n,M/2-1} \end{bmatrix} \quad (6.47)$$

Similarly, (6.44) reduces to

$$\begin{bmatrix} ID_{n,0} \\ ID_{n,1} \\ \vdots \\ ID_{n,M/2-1} \end{bmatrix} = \frac{1}{\sqrt{m'}} \mathbf{P}_3^T \begin{bmatrix} E_{M/2}^T & \\ & E_{M/2}^T \end{bmatrix} \mathbf{P}_3 \begin{bmatrix} B_{n,0}^{-1} \\ B_{n,1}^{-1} \\ \vdots \\ B_{n,M/2-1}^{-1} \end{bmatrix} \quad (6.48)$$

Note that the two terms $\sqrt{m'}$ and $\frac{1}{\sqrt{m'}}$ in (6.47) and (6.48) can be discarded simultaneously

without loss of generality. Thus, using (6.47) and (6.48), calculating \mathbf{D}_n^{-1} reduces to

- four times of $\frac{M}{2}$ -point FFT operation,
- four times of $\frac{M}{2}$ -point inverse FFT operation,
- $\frac{M}{2}$ times inversion of a 2×2 matrix.

Assuming that N -point FFT takes $\frac{N}{2} \log_2 N$ multiplications and $N \log_2 N$ additions and the inversion of a 2×2 matrix takes 3 multiplications and 1 addition, the whole inversion process of \mathbf{D}_n takes $2 * 4 \left(\frac{M/2}{2} \log_2 \frac{M}{2} \right) + \frac{M}{2} * 3 = M \left(2 \log_2 M - \frac{1}{2} \right)$ multiplications and $M \left(4 \log_2 M - \frac{3}{2} \right)$ additions.

The inverse of \mathbf{H} is given by

$$\mathbf{H}^{-1} = \mathbf{P}_1 (\mathbf{P}_2 \mathbf{H} \mathbf{P}_1)^{-1} \mathbf{P}_2 \quad (6.49)$$

where $\mathbf{P}_2 \mathbf{H} \mathbf{P}_1 = \text{diag} (\mathbf{D}_0, \mathbf{D}_1, \dots, \mathbf{D}_{N-1})$. Thus, to save time and memory requirements, instead of establishing the matrix $\mathbf{P}_2 \mathbf{H} \mathbf{P}_1$, one can, directly, get $D_{n,m'}$ in (6.39), for any given window function $h(k)$, by

$$D_{n,m'} = \begin{bmatrix} h_{2m}(n) & h_{(2m-1) \bmod M}(n) \\ -h_{2m+1}(N-1-n) & h_{2m}(N-1-n) \end{bmatrix} \quad (6.50)$$

for $m' = 0, 1, \dots, M/2 - 1$ and $n = 0, 1, \dots, N - 1$.

Using (6.50), (6.47), (6.48), (6.44) the whole inversion process of \mathbf{H} takes $L \left(2 \log_2 M - \frac{1}{2} \right)$ multiplications and $L \left(4 \log_2 M - \frac{3}{2} \right)$ additions.

6.4.2 Calculation of the Transform Coefficients

In this section, two methods to calculate the proposed transform coefficients are given

6.4.2.1 Method 1: Referring to (6.22), one proceeds for computing the m^{th} N transform coefficients as follows:

- Multiply the signal $x(k)$ by the biorthogonal function $\gamma(k - mN)$. Let the product be denoted by z which is of length MN .
- Divide z into M sections $\{z_0, z_1, z_2, z_3, \dots\}$ each of length N .
- Flip⁷ the odd numbered sections of z .
- If m is even
 - (a) Add the M sections as $z = \{z_0 - z_1 - z_2 + z_3 + \dots + z_M\}$.
 - (b) Take the N -point DCT-IV transform (5.5) of the resulting vector z .
- If m is odd
 - (a) Add the M sections as $z = \{z_0 + z_1 - z_2 - z_3 + \dots - z_M\}$.
 - (b) Take the N -point DST-IV transform (6.10) of the resulting vector z .

Assuming that the N point DCT or DST takes $\frac{N}{2} \log_2 N$ multiplications, this operation requires $NM^2 + \frac{MN}{2} \log_2 N = L(M + \frac{1}{2} \log_2 N)$ multiplications.

6.4.2.2 Method 2: Referring to (6.49), The transform coefficients, \mathbf{a} , is given by

$$\begin{aligned} \mathbf{a} &= \mathbf{E} \mathbf{P}_1 (\mathbf{P}_2 \mathbf{H} \mathbf{P}_1)^{-1} \mathbf{P}_2 \mathbf{x} \\ \mathbf{a} &= \mathbf{E} \mathbf{P}_1 \begin{bmatrix} \mathbf{D}_0^{-1} & & & \\ & \mathbf{D}_1^{-1} & & \\ & & \ddots & \\ & & & \mathbf{D}_{N-1}^{-1} \end{bmatrix} \mathbf{P}_2 \mathbf{x} \end{aligned} \quad (6.51)$$

Using $B_{n,m}^{-1}$, instead of \mathbf{D}_n^{-1} as in (6.41) and ignoring the multiplication of the permutation matrices \mathbf{P}_1 and \mathbf{P}_2 (this represents only change of row or column indices), the above

⁷ Flipping an N -dimensional vector \mathbf{x} is performed by replacing the element x_i by x_{N-i} .

equation includes

1. N times of
 - (a) $M/2$ multiplication of an 2×2 matrix by an 2×1 vector and
 - (b) two times taking the $\frac{M}{2}$ -point FFT and two times of $\frac{M}{2}$ -point inverse FFT operation
2. M times taking the N -point DCT-IV or DST-IV transforms.

This requires $N \left(4 \frac{M}{2} + 4 \frac{M/2}{2} \log_2 M/2 \right) + M \frac{N}{2} \log_2 N = L(\log_2 M + \frac{1}{2} \log_2 N + 1) = L(\log_2 L - \frac{1}{2} \log_2 N + 1)$ multiplication which is, still, an expensive computation.

6.4.3 Truncated Gaussian Function

The above operation requires $L(\log_2 L - \frac{1}{2} \log_2 N + 1)$ multiplications to calculate the transform coefficients and $L(2 \log_2 M - \frac{1}{2})$ to calculate \mathbf{H}^{-1} . There is still room for significantly reducing this number of operation by truncating the Gaussian function to a length $2N$. Following the same derivation as above, the resulting biorthogonal function (unlike the complex case) will be exactly of length $2N$ as will be seen in the following theorem.

Theorem 6.2

For any transform that has a structure as defined in (6.27), (6.28), (6.19), and (6.21), any window of length $2N$ leads to a biorthogonal function of the same length.

Proof. As we have seen in Section 6.3, the biorthogonal function can be obtained via the inversion of the matrix \mathbf{H} . If the window function is of length $2N$ (i.e., $h(n)$ is zero outside

the interval $[-\frac{N}{2} : \frac{3N}{2} - 1]$, \mathbf{H} of (6.21) will have the structure

$$\mathbf{H} = \left[\begin{array}{c} \text{Diagram of a grid with zigzag arrows} \end{array} \right] \quad (6.52)$$

which can be transformed to a block-diagonal matrix using the permutation matrices \mathbf{P}_4 and \mathbf{P}_5 whose encoding vectors p_4 and p_5 are given by

$$p_4(k) = \left\lfloor \frac{k}{M} \right\rfloor + N((k - a) \bmod M) \quad (6.53)$$

$$p_5(k) = l(N - 1) + (-1)^l \left\lfloor \frac{k}{M} \right\rfloor + N((k - a) \bmod M) \quad (6.54)$$

where

- $l = (k + a) \bmod 2$,
- $a = (1 - \left\lfloor \frac{k}{MN/2} \right\rfloor)$.

Note that, the previous permutation matrices \mathbf{P}_1 and \mathbf{P}_2 , still, could be used, while we introduce \mathbf{P}_4 and \mathbf{P}_5 to treat the edges. The matrix $[\mathbf{P}_2 \mathbf{H} \mathbf{P}_1]$ is block-diagonal

$$\mathbf{P}_5 \mathbf{H} \mathbf{P}_4 = \text{diag}(\mathbf{D}_0, \mathbf{D}_1, \dots, \mathbf{D}_{N-1}) \quad (6.55)$$

\mathbf{D}_n , in this case, is a block-diagonal matrix

$$\mathbf{D}_n = \text{diag}(\mathbf{d}_n, \mathbf{d}_n, \dots, \mathbf{d}_n) \quad \text{for } n = 0, \dots, N - 1 \quad (6.56)$$

where \mathbf{d}_n are a 2×2 matrices given by

$$\mathbf{d}_n \triangleq \begin{cases} \begin{bmatrix} +h(N-n-1) & +h(-n-1) \\ -h(N+n) & +h(n) \end{bmatrix} & \text{for } n = 0, \dots, N/2 - 1 \\ \begin{bmatrix} +h(n) & +h(n-N) \\ -h(2N-n-1) & +h(N-n-1) \end{bmatrix} & \text{for } n = N/2, \dots, N-1 \end{cases} \quad (6.57)$$

According to Theorem 6.1, Since the inverse of a block-diagonal matrix is also a block-diagonal with the same dimension, it follows that \mathbf{D}_n^{-1} is also a block-diagonal matrix with 2×2 blocks. Thus, $[\mathbf{P}_5 \mathbf{H} \mathbf{P}_4]^{-1} = \mathbf{P}_4^T \mathbf{H}^{-1} \mathbf{P}_5^T$ is also a block-diagonal matrix. As a consequence, \mathbf{H}^{-1} has the transpose structure of \mathbf{H} , i.e.,

$$\mathbf{H}^{-1} = \begin{bmatrix} \diagdown & & & & \\ & \diagdown & & & \\ & & \diagdown & & \\ & & & \diagdown & \\ & & & & \diagdown \\ \hline & & & & \\ & & & & \\ & & & & \\ & & & & \\ & & & & \end{bmatrix} \quad (6.58)$$

The diagonal, or anti-diagonal, elements from each block in any block row of \mathbf{H}^{-1} is the biorthogonal function, according to (6.38), which has only $2N$ non zero elements. This illustrates why the truncation of the window to a length of $2N$ gives a biorthogonal function which has also a length of exactly $2N$ ■

Corollary 6.2

For any window of length $2N$, the inversion of the matrix \mathbf{H} takes $5N$ operations irrespective of the length of the signal.

Proof. from the above theorem, the matrix \mathbf{H} can be transformed via row and column permutations into a block-diagonal matrix with 2×2 blocks. We have N distinct 2×2 blocks. Assuming that the inversion of 2×2 matrix takes 5 operations. the whole inversion

of \mathbf{H} takes $5N$ operations. ■

According to the above corollary, the inversion of \mathbf{H} takes only $5N$ operations which is a great reduction compared with the standard inversion $\mathcal{O}(N^3M^3)$. In this case, the calculation of transform coefficients requires only $L(2 + \frac{1}{2} \log_2 N)$ which is great reduction especially for large M . Comparing with Gabor transform, the fastest method currently available to calculate Gabor coefficients is the Zak-transform based method which takes $L(1 + \log_2 N + \log_2 M)$ multiplications. Table 8 shows the operational savings of the proposed method over the Zak-transform based method.

It is worth noting that this is an exact representation of the signal, i.e., using this method leads to an exact reconstruction of signal, and not just an approximation like the case mentioned in [25]. The only price to be paid is the ripples appearing in the frequency response in the Gaussian window due to truncation (see Fig. 42). The amplitudes of these ripples, however, are far less than the amplitude of the main lobe. The ratio is more than 43 db for any practical values of M and N . Thus, for all practical purposes, these ripples have negligible effect.

6.5 Conclusion

In this chapter we have presented a new linear critically-sampled JTF transform and showed that the resulting biorthogonal function is well localized in both time and frequency. In addition the resulting transform is stable which overcomes the main problem of the other implementations. An efficient method to calculate the biorthogonal function for any type of

N	M	# of multiplications		Saving Ratio
		Proposed	Zak	
8	32	896	1,920	2.14
8	256	7,168	21,504	3.0
8	512	14,336	47,104	3.29
16	32	2,048	4,096	2.0
16	256	16,384	45,056	2.75
16	542	32,768	98,304	3.0

TABLE 8: Operational savings of the proposed method over the Zak based one.

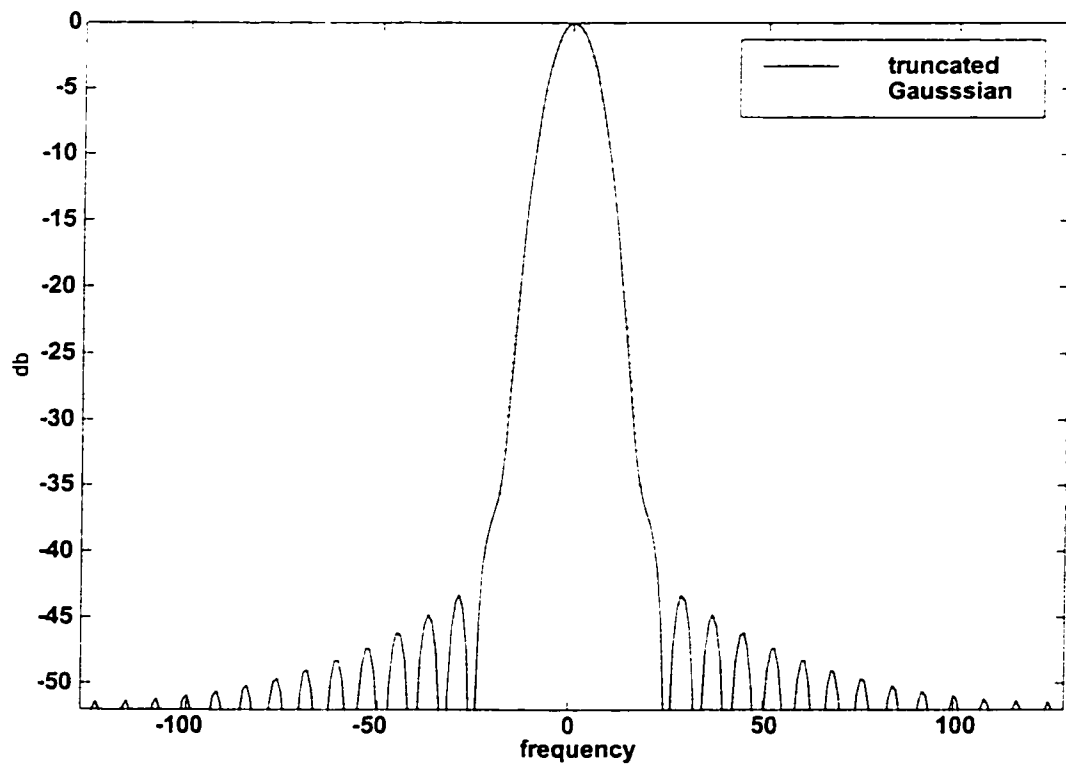


Figure 42: Effect of truncating the Gaussian window into a length of $2N$ in the frequency domain.

window is presented. An inherent characteristic of this implementation is that a truncated version of the modulating window to a length of $2N$ leads to a biorthogonal function with the same length. Using this truncated Gaussian window and its biorthogonal function results in an algorithm which requires $L(2 + \frac{1}{2} \log_2 N)$ operations for computing transform coefficients and $5N$ operations for computing the biorthogonal function. This is faster than any other algorithm currently available in the literature. The effect of this truncation on the transform coefficients has been studied. It is worthy to note that, this truncated window function transform leads to an exact representation of the signal, i.e., using this transform leads to an exact reconstruction of the signal, and not just an approximation as is the case in [25].

CHAPTER 7

APPLICATION: NOISE REDUCTION FOR NUCLEAR MAGNETIC RESONANCE FREE INDUCTION DECAY SIGNALS

In this chapter we will demonstrate the usefulness of the developed transforms in practical life. Here, it will be applied to the traditional, yet difficult, problem of noise reduction of the nuclear magnetic resonance signals. It will be shown that the proposed transform gives far better results with lower computational requirements than other transforms.

7.1 Introduction

Nuclear Magnetic Resonance (NMR) Free Induction Decay (FID) signals are very popular in chemical and biomedical applications and research. In medicine, NMR is the physical basis of magnetic resonance imaging (MRI) which plays to everyone's fascination with the expanding capabilities of medical imaging technology. Another important use of NMR

is spectroscopy, a technique that can determine a material's chemical decomposition.

The main obstacle of the NMR is its very low signal to noise ratio (SNR). Increasing the SNR can be achieved by any of the following:

- Increasing the magnetic flux which will increase the signal energy, or
- Taking large number of repetitive signals, or
- Decreasing the noise energy, or
- Applying an Intelligent Discrete Signal Processing (I-DSP) technique to reduce the noise.

Increasing the magnetic flux means a bigger magnet which is the most expensive part of any NMR device (about \$1 million per tesla). Besides, a bigger magnet needs bigger weight (1.5-tesla magnet weighs 15,000 kg), high shielding, . . .etc. On the other hand, taking large number of signals lengthens imaging time. Decreasing the noise energy is done by enhancing the receiver coil since most of the noise is thermal noise coming from the receiver coil. In some expensive NMR devices, conventional copper receiver coil is replaced by a superconductor one. The area of applying I-DSP technique to NMR signals is attractive because of the rapid drop in the prices of the hardware. Besides, the noise and the signal have special characteristics (to be discussed below) which can be advantageously exploited using I-DSP.

For automatic processing of NMR data, various model-fitting techniques are used to estimate the model parameters[41]. It is, however, a difficult job because the model is nonlinear and the noise is relatively high. Thus, it is extremely beneficial to reduce the noise either as preprocessing step before the model-fitting technique or to visualize the data

in a form easy to be interpreted by the experts.

The importance of joint Time-Frequency domain methods in NMR was proved earlier via the use of Wigner Distribution [42], Zak Transform [43], and Gabor Transform [44]. In this work, we propose to use our JTF transform proposed in Chapter 6 to reduce the noise in the NMR-FID signal. In [44], a Generalized Gabor Transform (GGT) was used to do the same job and good results were reported. Since our goal in this chapter is to show the advantage of the proposed transform, we follow exactly the same method used in [44] except that the GGT is replaced by our transform. Moreover, we use the same data which was used in [44] for fair comparison. Other simulated data which has been extensively used as test data in the NMR literature [42, 43] was also tested.

The organization of the chapter is as follows. In section II, a brief introduction to the physics behind the NMR-FID signals is given. In section III, the technique used to reduce the noise is discussed. In section IV, we mathematically analyze the behavior of the transform on the NMR-FID signals. Section V&VI give results on NMR-FID signals.

7.2 Basic Theory of NMR

The theory of NMR has been extensively discussed in the literature [45]. A brief discussion of the basic theory which is sufficient for our purpose is given here.

The basis for nuclear magnetic resonance is that protons precess when placed in a magnetic field \mathbf{B} . Nuclear precession occurs with a frequency directly proportional to the strength of the magnetic field, with a proportionality constant called the gyromagnetic ratio

γ , of about 42.6 megahertz per tesla.

$$\Delta E = \frac{\gamma h}{2\pi} B$$

Typical frequencies range from 300 to 800 MHz for magnetic field B of about 4 tesla.

The precessional axis lies along the direction of the magnetic field. If an oscillating magnetic field at the precessional frequency is applied perpendicular to the static field, the protons will precess about the axis of the oscillating field, as well as that of the static field. The condition is known as nutation. The oscillating field is generated by a tuned RF coil which usually surrounds the sample. The magnetic field of the precessing protons induces, in turn, an oscillating voltage in the RF coil, which is detected when the RF field is gated off. This voltage, after gating the RF coil off, has exponential decay with time. Therefore, it is named *free induction decay*. This voltage is then amplified and demodulated to baseband, as in a normal superheterodyne receiver, and digitized using an analog-to-digital converter. The oscillating RF pulse is repeated and the FID's are added coherently.

To factor out the signal's dependence on the static magnetic field, NMR measurements are often given in a unitless quantity called the chemical shift, δ , which is typically measured in parts per million. It is the difference between the precession frequency of protons that are part of a particular molecular group and that of protons in a reference compound, divided by the latter, that is

$$\delta = \frac{f_{\text{sample}} - f_{\text{reference}}}{f_{\text{reference}}} \times 10^6 \text{ ppm}$$

This application of magnetic resonance is generally referred to as high-resolution NMR spectroscopy, and is widely used in the pharmaceutical and chemical industries.

In MRI, it is the protons in the water molecules of a patient's tissue that are the source of the signal. The spatial information needed to form images from magnetic resonance is obtained by placing magnetic field gradient coils on the inside of the magnet. These coils, constructed from copper wire, create additional magnetic fields that vary in strength as a linear function of distance along the three spatial axes. Thus, the resonant frequencies of the water protons within the patient's body are now spatially encoded. The contrast in MRI images arises from differences in the number of protons in a given volume and in their relaxation times (the time taken for the magnetization of sample to return to equilibrium after the RF pulse is turned off), which are related to the molecular environment of the protons.

7.3 Noise Removal of NMR-FID Signals

Any NMR-FID signal $x(t)$ is well modeled as a finite mixture of modulated exponential functions plus noise [46], i.e.,

$$x(t) = \sum_{m=1}^M b_m e^{-\pi d_m t} e^{j(2\pi f_m t + \phi_m)} + n(t)$$

where b_m , f_m , ϕ_m , and d_m is the amplitude, frequency, phase and exponent constant (in

NMR terminology, $T_2 = \frac{1}{\pi d}$) of the m^{th} component. $x(t)$ can be written as

$$x(t) = \sum_{m=1}^M b_m e^{-\pi d_m t} e^{j2\pi f_m t} + n(t)$$

where ϕ_m is absorbed in b_m , i.e., b_m is now a complex quantity. In the discrete case, $x(t)$ is

$$x(k) = \sum_{m=1}^M b_m e^{-\pi d_m \Delta_t k} e^{j2\pi f_m \Delta_t k} + n(k)$$

where Δ_t is the sampling period. The signal is supposed to have a positive time support, i.e., $x(k) = 0, k < 0$. The signal $x(k)$ is a time varying signal which means that the frequency components of the signal are function of time. Consequently, an easily applied JTF representation is needed for mathematically describing both the time and frequency characteristics of the signal simultaneously. The noise term, $n(k)$, is mainly thermal noise due the receiver coil. Thus, it is well approximated by an additive white Gaussian noise (AWGN) with zero mean and standard deviation σ .

By representing the NMR-FID signal in a JTF domain, the true signal energy will be concentrated in a small area (the signal contains few frequencies in short times) while the noise will span the entire domain. Thus, the SNR, in terms of the JTF coefficients, will be significantly enhanced in the area where the signal's JTF coefficients are nonzero. In addition, there will be two distinct areas in the JTF domain: one contains noise only and the other contains signal plus noise. Thus, separating the two areas by a suitable thresholding technique would enhance the signal significantly. A *linear critically-sampled* JTF transform is needed such that getting back the signal from the JTF domain is easy.

In [44], a GGT (which is a linear critically sampled JTF Transform) was used to present the NMR-FID signal and hence reduce the noise using a simple thresholding technique. It is shown in Appendix G that this GGT is unstable. Also, it is very sensitive to the chosen parameters (as was stated in [44]).

In this work, we will use the *same* method of [44] after replacing the GGT by the one proposed in Chapter 6. Its good stability and its nice biorthogonal function have the advantages that no error magnification during the transformation process occurs and that the signal will be represented by fewer number of coefficients. The *same data* used in [44] will be used in demonstrating the superiority of our transform.

Before getting into the details of our technique to reduce the noise, an explanation of how a single modulated exponent will appear in the transformed domain is given.

7.4 Behavior of the Transform Coefficients for Modulated Exponent.

Let us take only one component of the noise-free NMR-FID signal in the discrete case which is a modulated exponent

$$x_1(k) = be^{-\pi d \Delta_t k} e^{j2\pi f \Delta_t k} \quad (7.1)$$

where $x_1(k) = 0, k < 0$.

Referring to Fig. 43, $x_1(k)$ in the time domain (e) is composed of a cosine function (a) multiplied by an exponential decaying function (c). The frequency response of the cosine

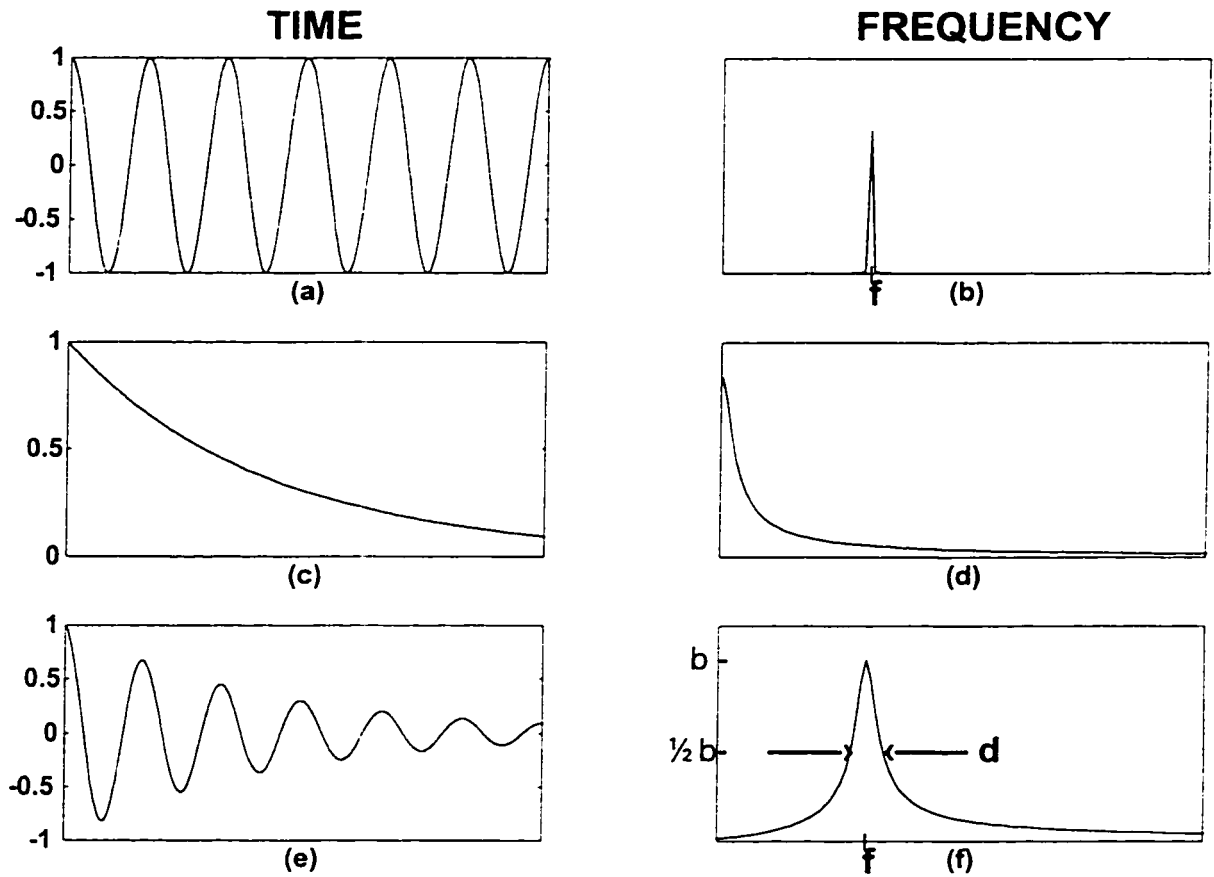


Figure 43: Modulated exponent in time (e) is the multiplication of non-decaying complex exponent (a) with the exponential decay function (c). In frequency, modulated exponent (f) is the convolution of the non-decaying complex exponent (b) with the exponential decay function (d).

function is a delta function (b) and the frequency response of the exponential decaying function is another exponential decaying function (d). In the frequency domain, $x_1(f)$ (f) is the result of the convolution process of (b) and (d). From (f), we can determine the most important three parameters of the modulated exponent, that is

1. the magnitude of b , which is proportional to the height of the spike.
2. the frequency f , which is the location of the spike in the frequency axis.
3. the damping rate d , which is the width of the line at half-height.

Note that determining the damping rate d from the frequency domain is not precise at all.

In the JTF domain, the transform coefficients of $x_1(k)$, using (6.23), is plotted in Fig. 44, as an intensity plot and in Fig. 45 as a surface plot. Here, Δ_t , b , d , f , ϕ are taken as $166.2\mu s$, 32000 , $\frac{1}{22}$ ms, -1450 Hz, 55° , respectively. As we see from the graphs, the modulated exponent is represented in the JTF domain by a spike centered at f in the frequency axis and has a decaying exponent in the time axis. In the following theorem, the relationship of this decay with the envelope of the modulated exponent in the time domain (the $e^{-\pi d \Delta_t k}$ term) is determined.

Theorem 7.1

The rate of decay of the spike of the modulated exponent in the time direction in the proposed JTF domain is equal to $d \cdot N$ where d is the damping rate of the modulated exponent and N is the number of frequency components in each shift.

Proof. The transform coefficients can be calculated from the analysis equation

$$a_{m,n} = \sum_{k=0}^{L-1} \gamma^*(k - mN) x(k) \sqrt{\frac{2}{N}} \begin{cases} \cos\left(\frac{\pi(k+\frac{1}{2})(n+\frac{1}{2})}{N}\right) & \text{for even } m \\ \sin\left(\frac{\pi(k+\frac{1}{2})(n+\frac{1}{2})}{N}\right) & \text{for odd } m \end{cases} \quad (7.2)$$

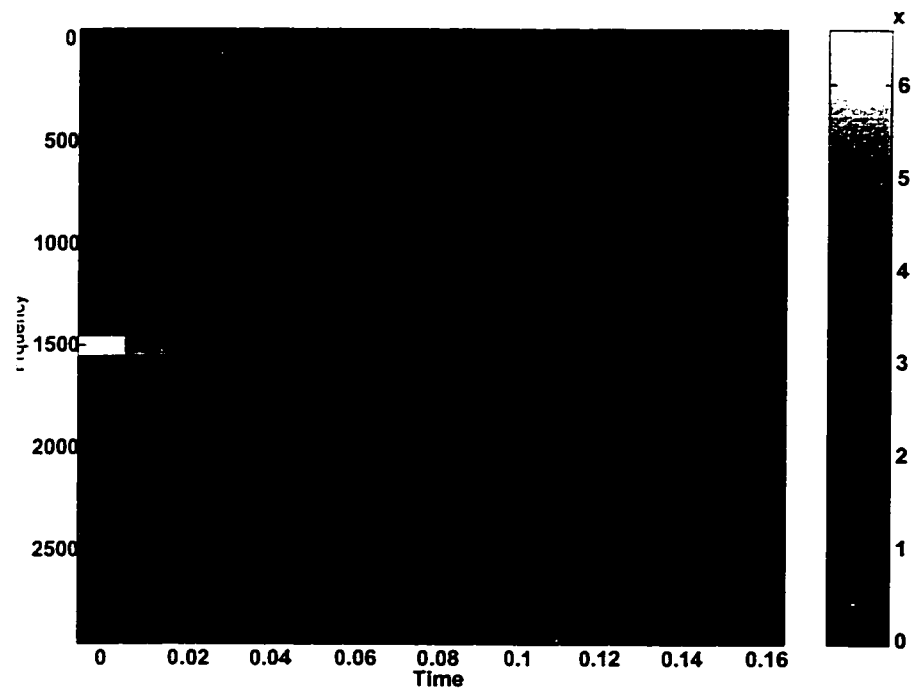


Figure 44: The transform coefficients, magnitudes, of the modulated exponent.

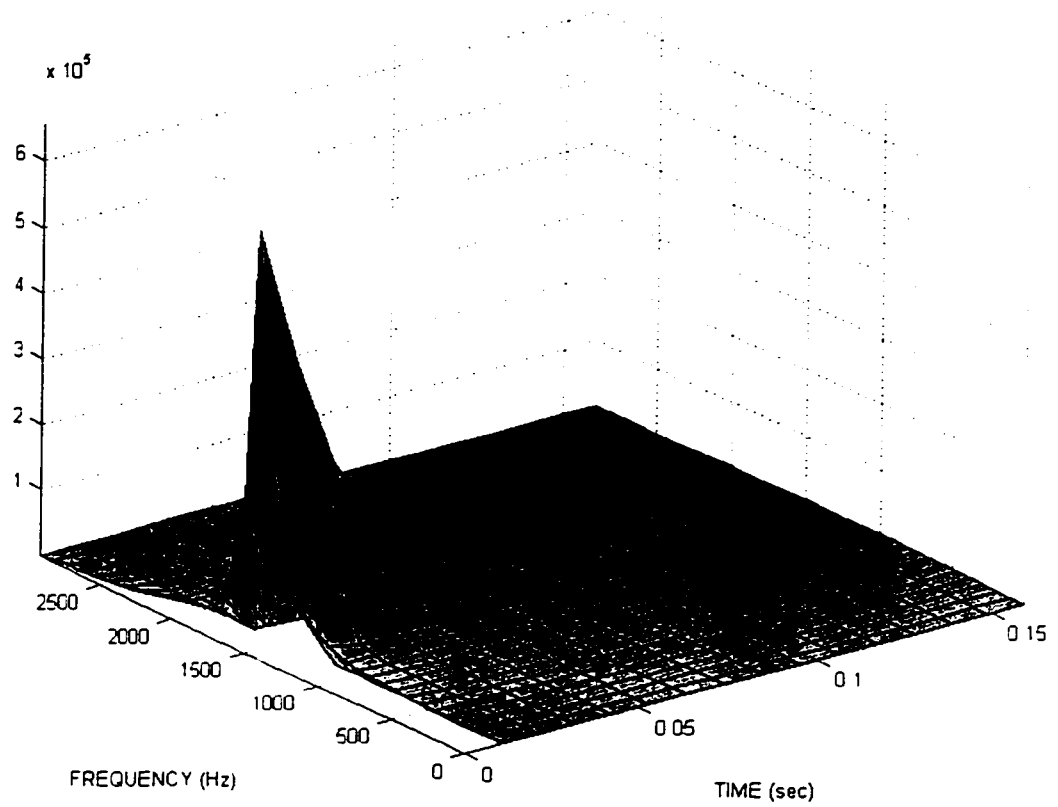


Figure 45: The transform coefficients of the modulated exponent. (surface plot)

For even m , the transform coefficient $a_{m,n}$ of $x_1(k)$ is given by

$$a_{m,n} = b \sum_{k=0}^{L-1} \gamma^*(k - mN) e^{-\pi d \Delta_t k} \times e^{j2\pi f \Delta_t k} \sqrt{\frac{2}{N}} \cos\left(\frac{\pi(k+\frac{1}{2})(n+\frac{1}{2})}{N}\right) \quad (7.3)$$

while the transform coefficient $a_{m+2l,n}$, where l is an integer, is given by

$$a_{m+2l,n} = b \sum_{k=0}^{L-1} \gamma^*(k - (m+2l)N) e^{-\pi d \Delta_t k} \times e^{j2\pi f \Delta_t k} \sqrt{\frac{2}{N}} \cos\left(\frac{\pi(k+\frac{1}{2})(n+\frac{1}{2})}{N}\right) \quad (7.4)$$

Substituting $k' = k - 2lN$

$$\begin{aligned} a_{m+2l,n} &= b \sum_{k'=-2lN}^{L-2lN-1} \gamma^*(k' - mN) e^{-\pi d \Delta_t (k'+2lN)} \\ &\quad e^{j2\pi f \Delta_t (k'+2lN)} \sqrt{\frac{2}{N}} \cos\left(\frac{\pi(k'+2lN+\frac{1}{2})(n+\frac{1}{2})}{N}\right) \\ &= b e^{-\pi \Delta_t 2lN(d+j2f)} \sum_{k'=-2lN}^{L-2lN-1} \gamma^*(k' - mN) \exp(-\pi d \Delta_t k') \\ &\quad e^{j2\pi f \Delta_t k'} \sqrt{\frac{2}{N}} \cos\left(\frac{\pi(k'+2lN+\frac{1}{2})(n+\frac{1}{2})}{N}\right) \end{aligned} \quad (7.5)$$

From trigonometric identities

$$\cos\left(\frac{\pi(k'+2lN+\frac{1}{2})(n+\frac{1}{2})}{N}\right) = (-1)^l \cos\left(\frac{\pi(k'+\frac{1}{2})(n+\frac{1}{2})}{N}\right)$$

Thus, (7.5) can be written as

$$a_{m+2l,n} = (-1)^l b e^{-\pi \Delta_t 2lN(d+j2f)} \sum_{k'=-2lN}^{L-2lN-1} \gamma^*(k' - mN) e^{-\pi d \Delta_t k'} e^{j2\pi f \Delta_t k'} \sqrt{\frac{2}{N}} \cos\left(\frac{\pi(k' + \frac{1}{2})(n + \frac{1}{2})}{N}\right) \quad (7.6)$$

Since we have periodic transformation, i.e., both the signal and the biorthogonal are assumed to be periodic with period L , The summation from $-2lN$ to $L - 1 - 2lN$ is exactly equal to the summation from 0 to $L - 1$. Thus, (7.6) can be rewritten as

$$\begin{aligned} a_{m+2l,n} &= (-1)^l b e^{-\pi \Delta_t 2lN(d+j2f)} \sum_{k'=0}^{L-1} \gamma^*(k' - mN) e^{-\pi d \Delta_t k'} e^{j2\pi f \Delta_t k'} \sqrt{\frac{2}{N}} \cos\left(\frac{\pi(k' + \frac{1}{2})(n + \frac{1}{2})}{N}\right) \\ &= (-1)^l e^{-\pi \Delta_t 2lN(d+j2f)} a_{m,n} \\ &= e^{-\pi \Delta_t 2lNd - j\pi l(\Delta_t 4Nf + 1)} a_{m,n} \end{aligned}$$

Thus, the magnitude of the coefficients value is given by

$$|a_{m+2l,n}| = e^{-\pi \Delta_t 2lNd} |a_{m,n}|$$

A similar proof could be done for odd m . This indicates that the transform coefficients are exponentially decaying in the time direction, time is represented by the index m , with the decaying constant equal to $d \cdot N$. ■

From the above discussion, one can directly and precisely determine the three parameters of the modulated exponents from the JTF domain, that is the amplitude, frequency, and

the damping rate. Next, to illustrate the effect of the noise on this domain, additive white Gaussian noise with zero mean and Standard Deviation $\sigma = 2000$ is added to the signal. The resulting coefficients are plotted in Fig. 46. From the figure, it is obvious that in contrast to the signal components which are concentrated in a very few number of the transform coefficients, the noise is fairly distributed among all the transform coefficients. In the next two sections, the proposed transform is applied to a real NMR signals to remove the noise.

7.5 Removing Noise from Phosphorus FID Signal.

As an example which was used in many papers as a test data [42, 43], consider a simulated phosphorus FID sequence (distorted to explore a wider range of values of the parameters). This simulated phosphorus FID signal composed of six peaks: a reference signal, P_i , PCr, γ , α , and β . The frequencies, damping factors, amplitudes, and phases are given in Table 9. The dwell time (sampling period Δ_t) is $166.2 \mu s$ and the FID sequence is 1024 points long. Figures 47 and 48 show the real and imaginary parts of this signal. The corresponding spectrum is shown in Fig. 49. A zero mean white Gaussian noise with standard deviation $\sigma = 2000$ is added to the FID sequence which results in the spectrum shown in Fig. 50. The resulting SNR is -1.7954 db. Here, since this is a time varying signal, the SNR is defined as the signal energy⁸ over the energy of the noise in the observation period. This is exactly the same examples used in [42, 43] but with realistic noise variance. From Fig. 50, it is clear that the P_i , γ , α , and β components are totally distorted by the noise.

⁸ The reference signal is not included.

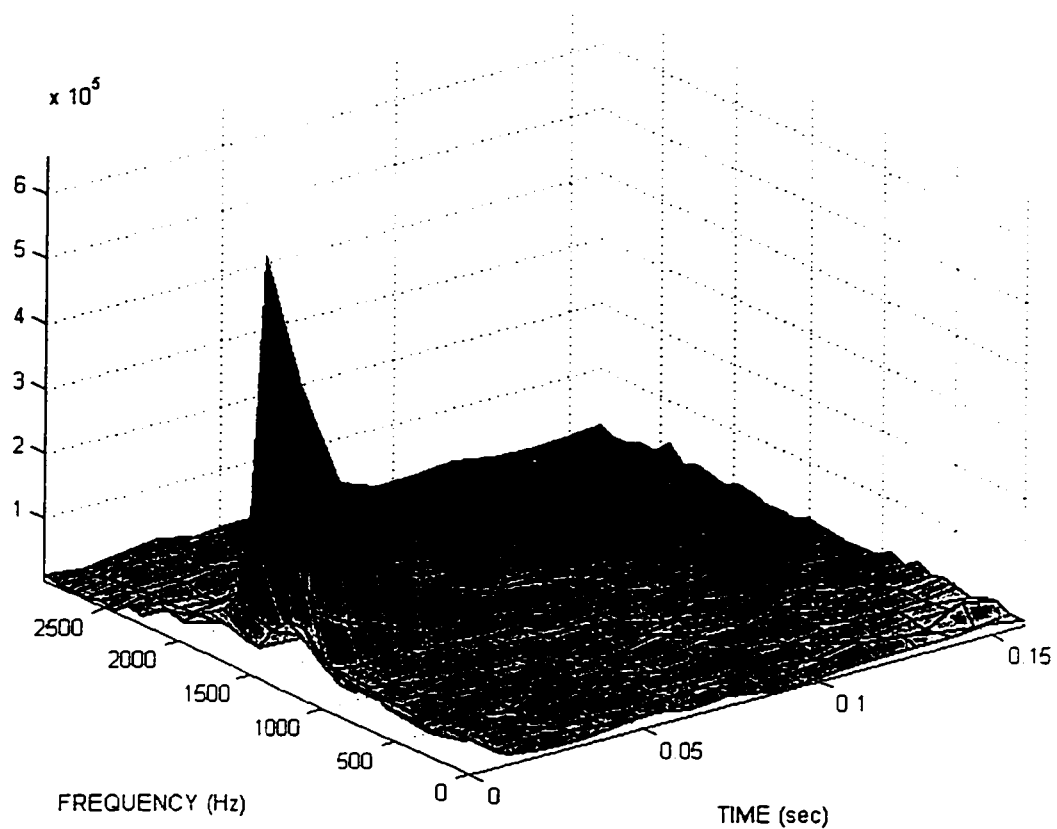


Figure 46: The transform coefficients of the modulated exponent after adding AWGN.

Peak	Frequency (Hz)	Time const. (ms)	Amplitude	Phase (°)
Reference	-1590	11	32,000	55
P _i	-600	2	10,000	83
PCr	-60	20	6,000	98.5
γ	240	6	9,000	107.5
α	860	3	8,000	122.5
β	1900	5	4,000	153

TABLE 9: Parameters of Simulated Phosphorus FID

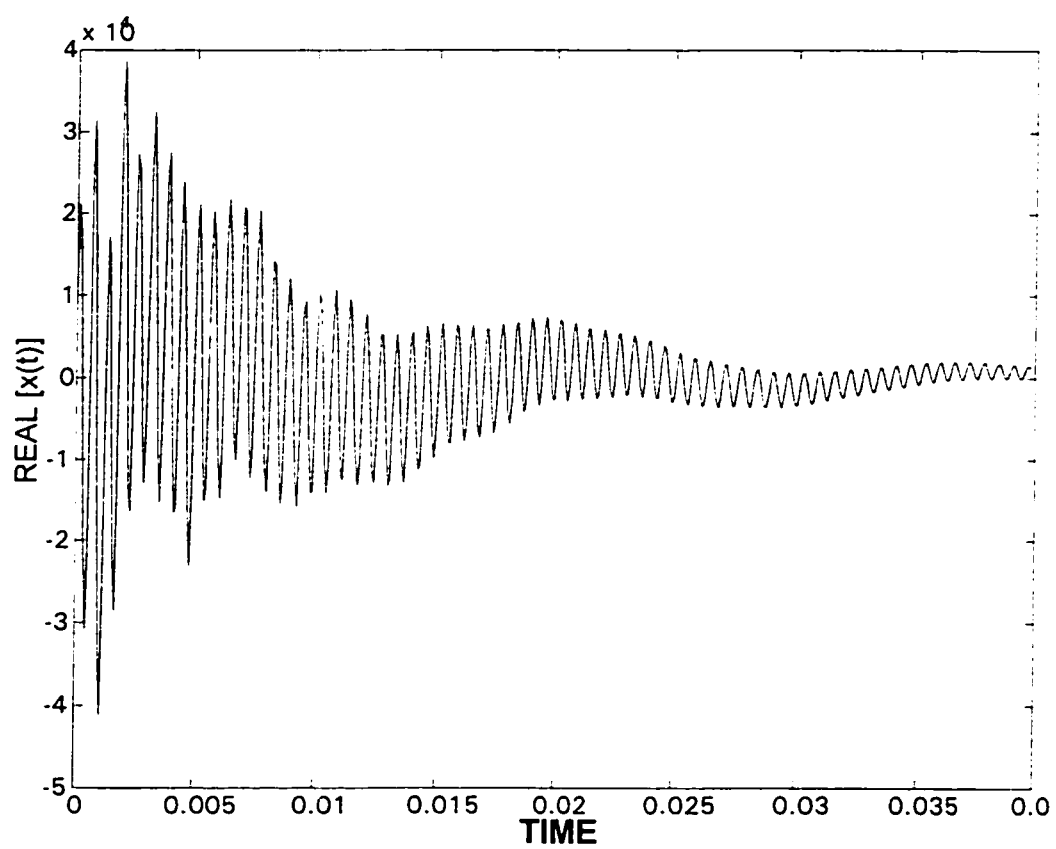


Figure 47: Real part of the Phosphorus FID signal without noise.

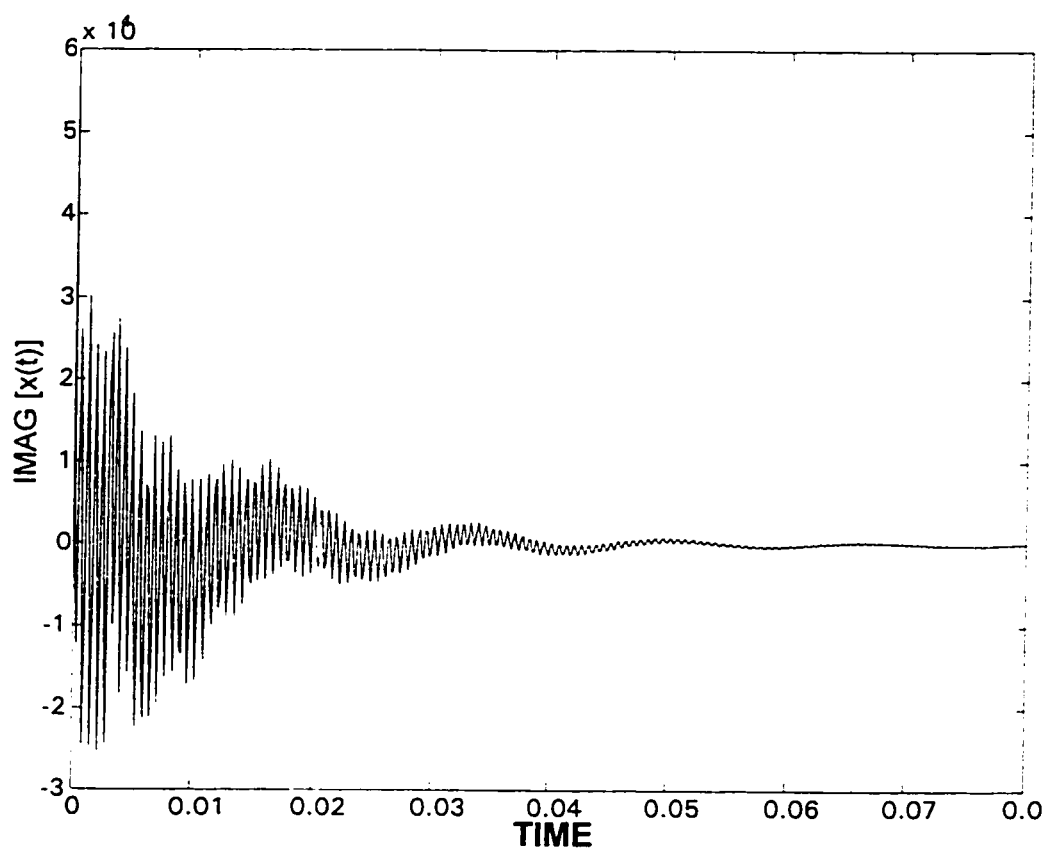


Figure 48: Imaginary part of the Phosphorus FID signal without noise.

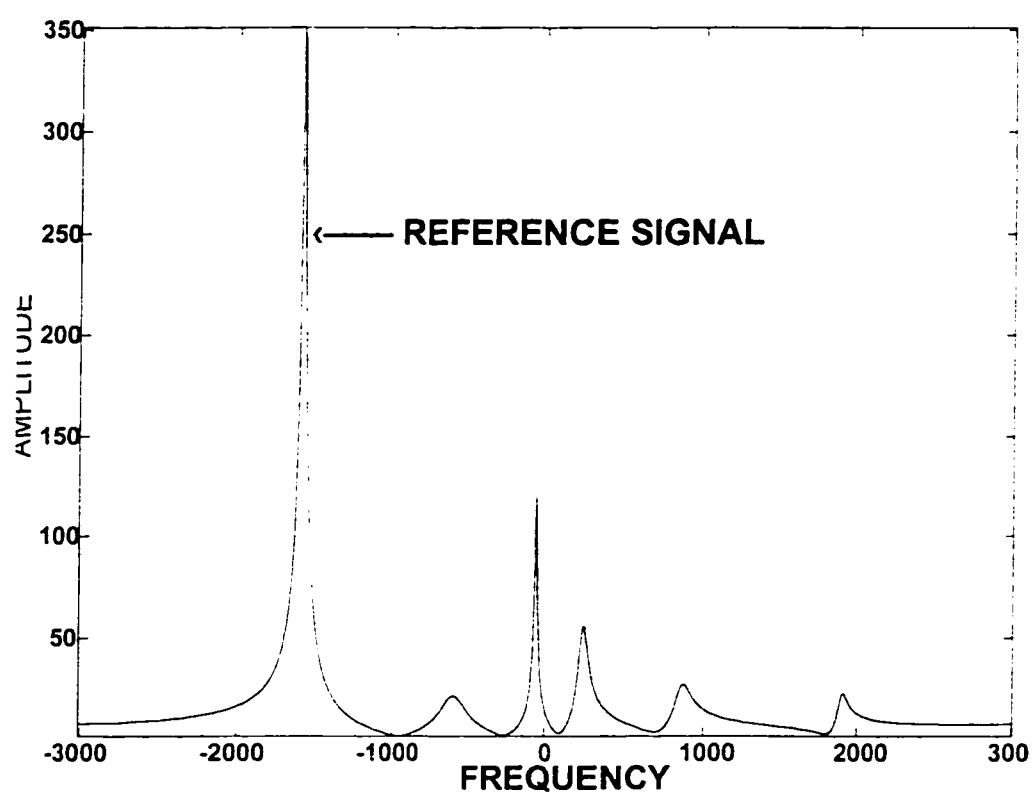


Figure 49: Spectrum of the Phosphorus FID without noise.

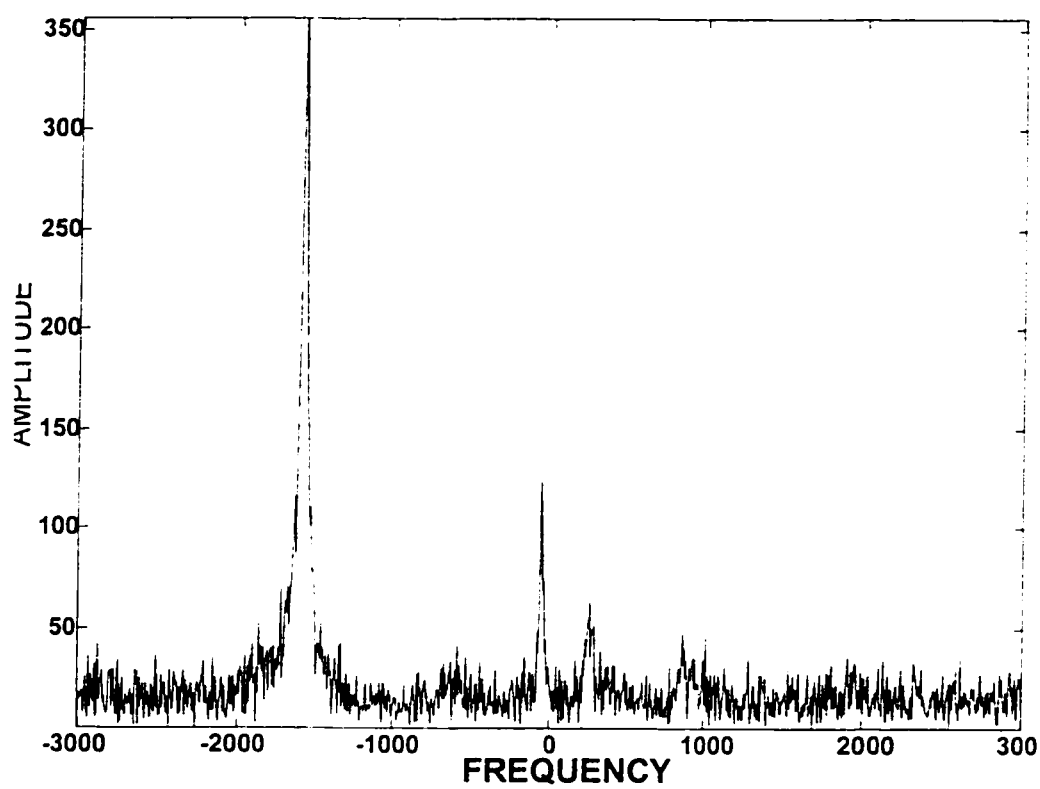


Figure 50: Spectrum of the Phosphorus FID with added zero mean Gaussian noise with St. Dev. = 2000.

A simple algorithm is proposed to reduce the noise as follows: Perform the Time-Frequency transform (6.23) for the NMR_FID sequence and retain only the coefficients which their magnitudes are above a certain threshold. Then, perform the inverse Time-Frequency transform (2.24) on the retained coefficients to get the noise-reduced NMR-FID sequence. Fig. 51, shows the spectrum of the noise-reduced NMR-FID signal sequence. It is now easy to notice the six peaks: a reference signal, P_i , PCr, γ , α , and β . The square error sequence between the noise-free signal and the noisy signal is shown in Fig. 52 (a), while the square error sequence between noise-free signal and the noise-reduced signal is shown in Fig. 52 (b). One can notice the great reduction of the noise after removing the noise by the proposed technique. The SNR increased from -1.7954 db to 10.3837 db. (a gain of 12.18 db in the SNR).

As a comparison, the same procedure is applied using the GGT proposed in [44]. Fig. 53 shows the spectrum of the noise-reduced NMR-FID signal sequence. The square error sequence between the noise-free signal and the noise-reduced signal is shown in Fig. 52 (c). The signal to noise ratio increased to 5.49 db. This indicates a gain of 4.888 db in the SNR between this method and our method. This gain is due to the stability of our transform which ensures no magnification of the noise during the transformation process. Another more important difference appears in the resulting spectrums. While one can recognize the six peaks easily in our spectrum, it is not so in the other spectrum. This is because its biorthogonal function is not localized in the frequency domain and hence the signal energy is distributed among more JTF coefficients. This worsen the effect of the thresholding technique on the signal itself.

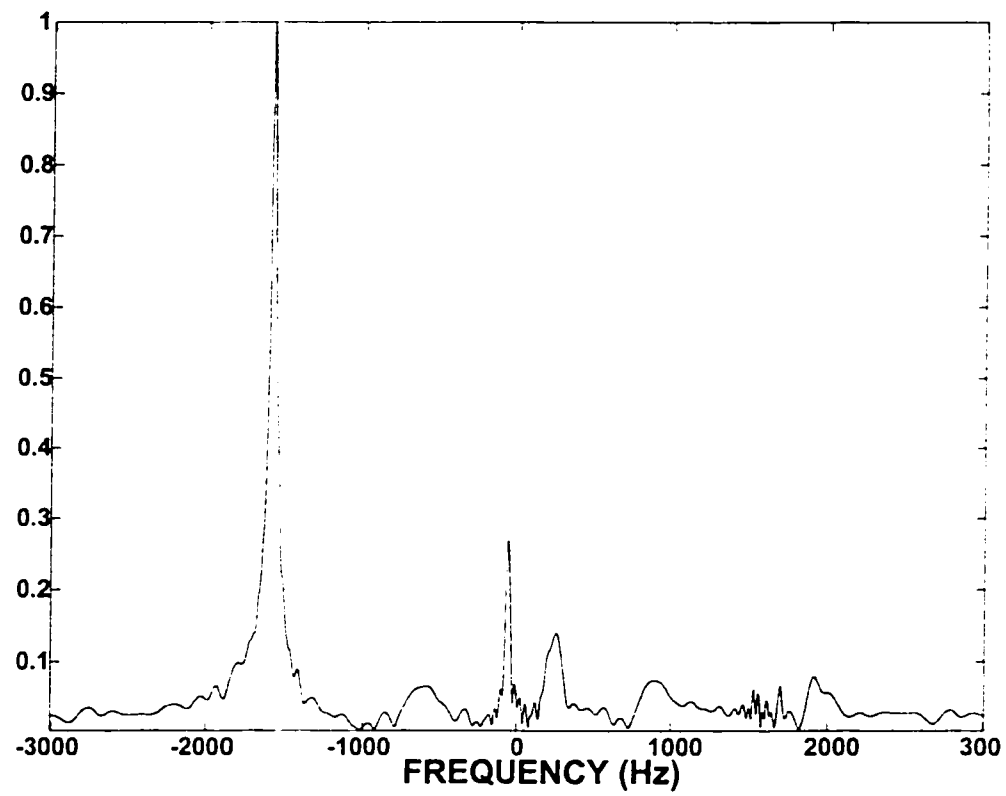


Figure 51: Same spectrum after removing the noise by the proposed method.

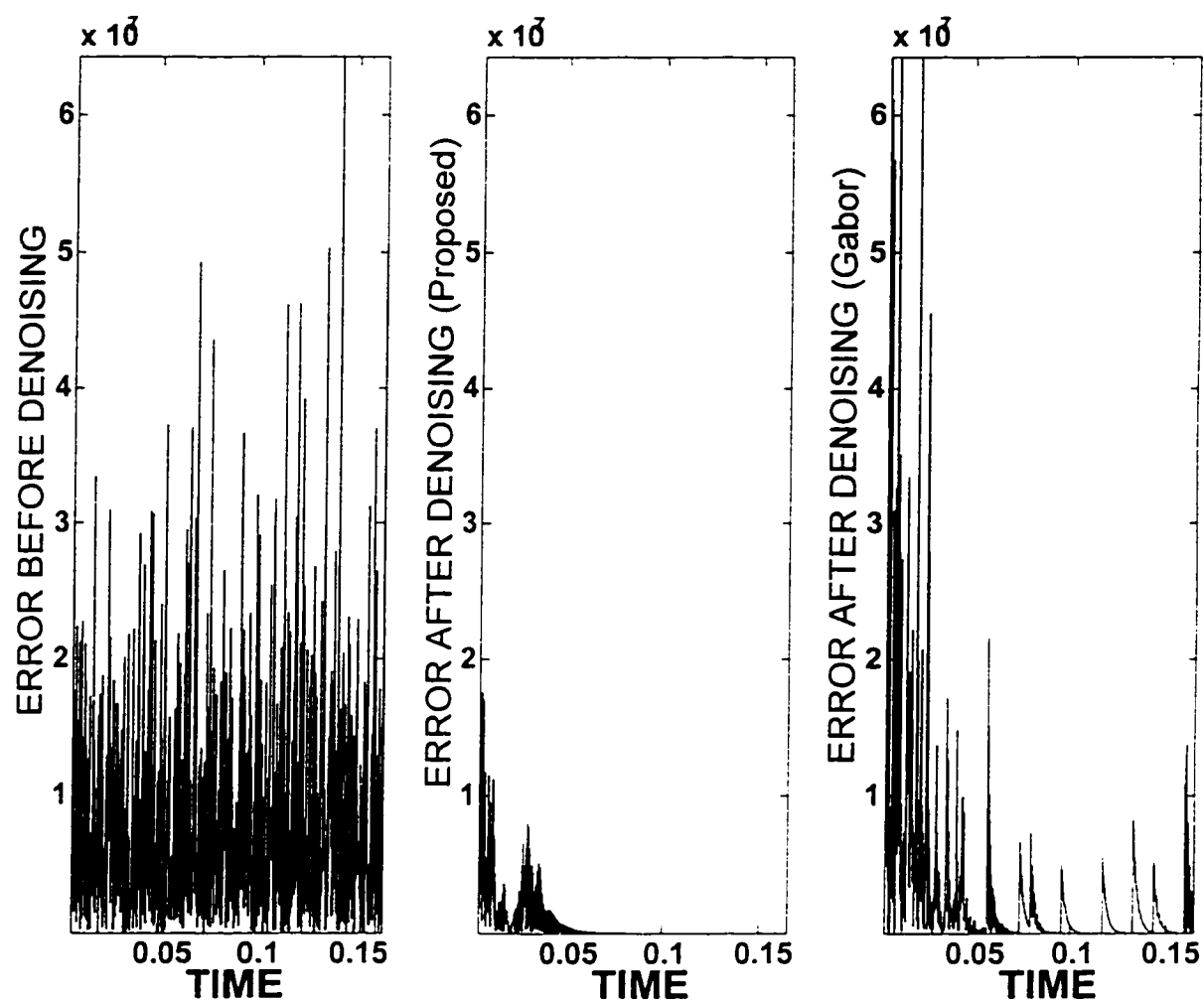


Figure 52: The square error in the original signal (a), after removing the noise with the proposed transform (b) , and after removing the noise with GGT (c).

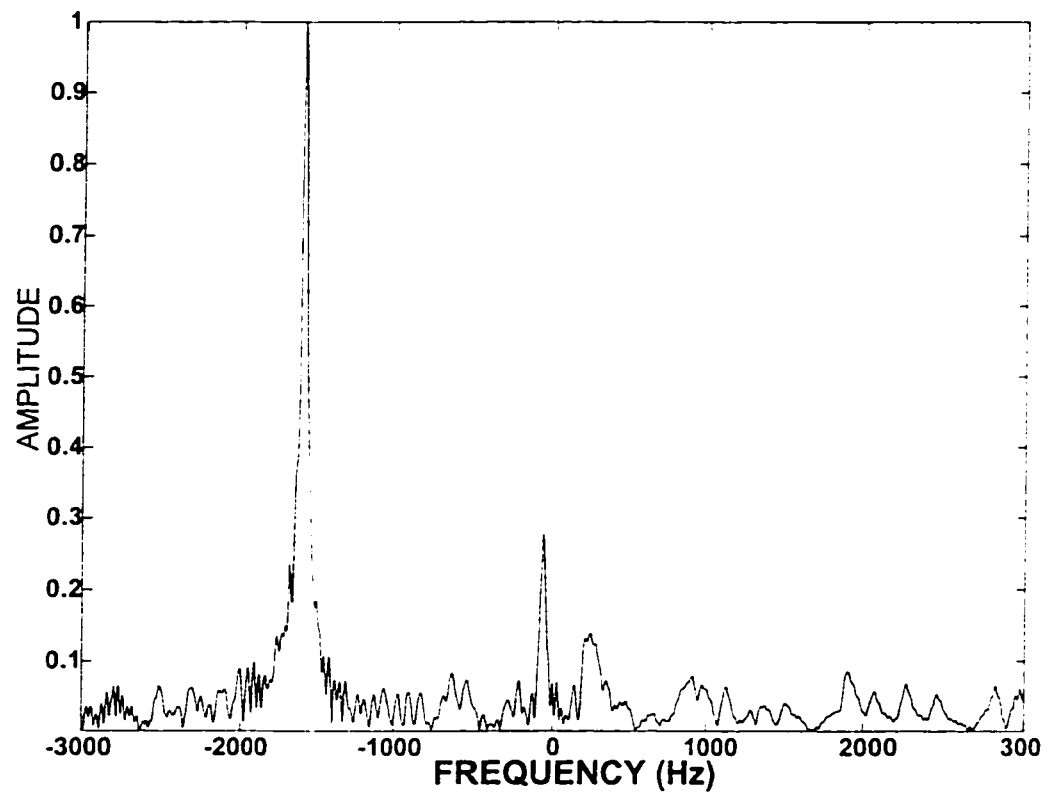


Figure 53: Same spectrum after removing the noise by the GGT method.

7.6 Removing Noise from a Real-life FID Signal

A real NMR-FID signal was provided by Dr. Joel M. Morris, Chairman, Electrical Engineering Department at University of Maryland, Baltimore County, which was used in [44] to reduce the noise in NMR-FID signals. This signal was provided to Dr. Morris by K. Wear of the Food and Drug Administration. The data was sampled at 2 kHz (i.e., $\Delta_t = 0.5ms$) for a static magnetic field of 1.5T with a repetition rate of 3 sec. The FID is 512 points long. Fig. 54 shows the real part of the signal. The corresponding spectrum is shown in Fig. 55. From the figure, it is clear that the spectrum is totally distorted by the noise. Fig. 56 is the mesh plot of the magnitudes of the proposed transform coefficient for $N = 32$. In the JTF plane it is obvious that the signal components are concentrated in a very few number of the proposed transform coefficients. Thus, the magnitudes of the signal-free coefficients are at a much lower level than the magnitudes of the coefficients containing the pure signal. Thus, they can be easily discriminated by using thresholding techniques.

A simple thresholding technique is implemented by applying a threshold to the proposed transform coefficient magnitudes and equating the coefficients which have values lower than this threshold to zero. The retained transform coefficients define the JTF expansion of the noise-reduced NMR-FID signal. Fig. 57 shows the mesh plot of the magnitude of the proposed transform coefficients after thresholding with threshold value be 66. The corresponding spectrum is shown in Fig. 58. In this figure, the NMR peaks become more obvious than they are in the original spectrum.

As a comparison, the resulting JTF coefficients of the same signal using the GGT are

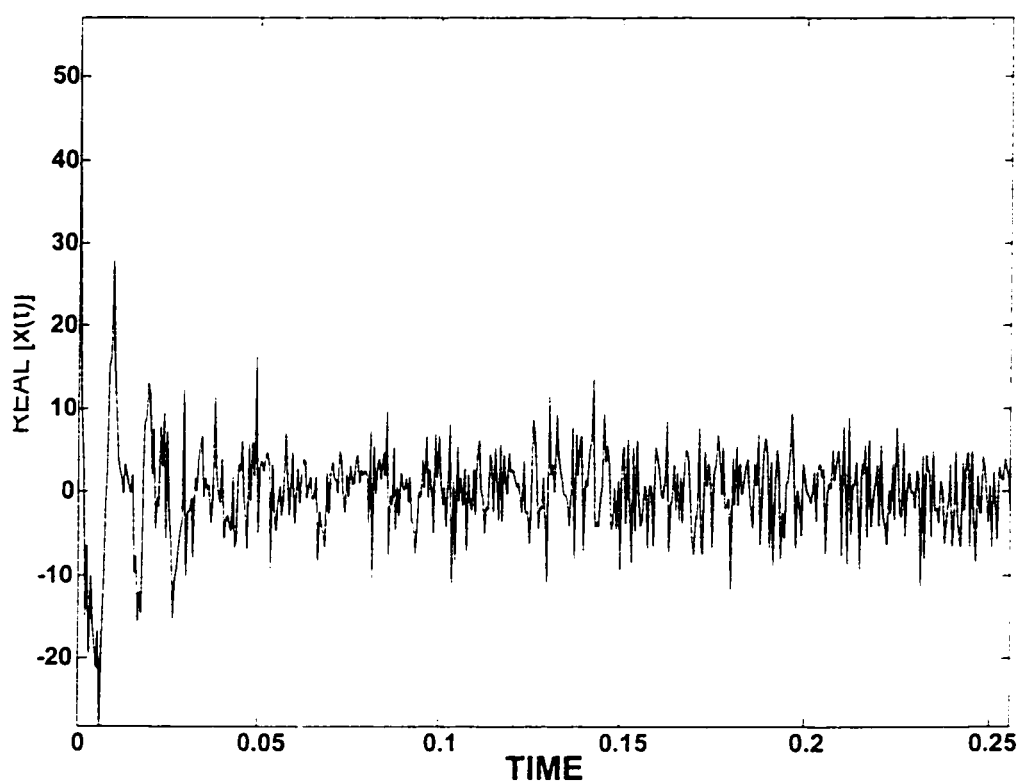


Figure 54: Real part of the real-life NMR-FID signal.

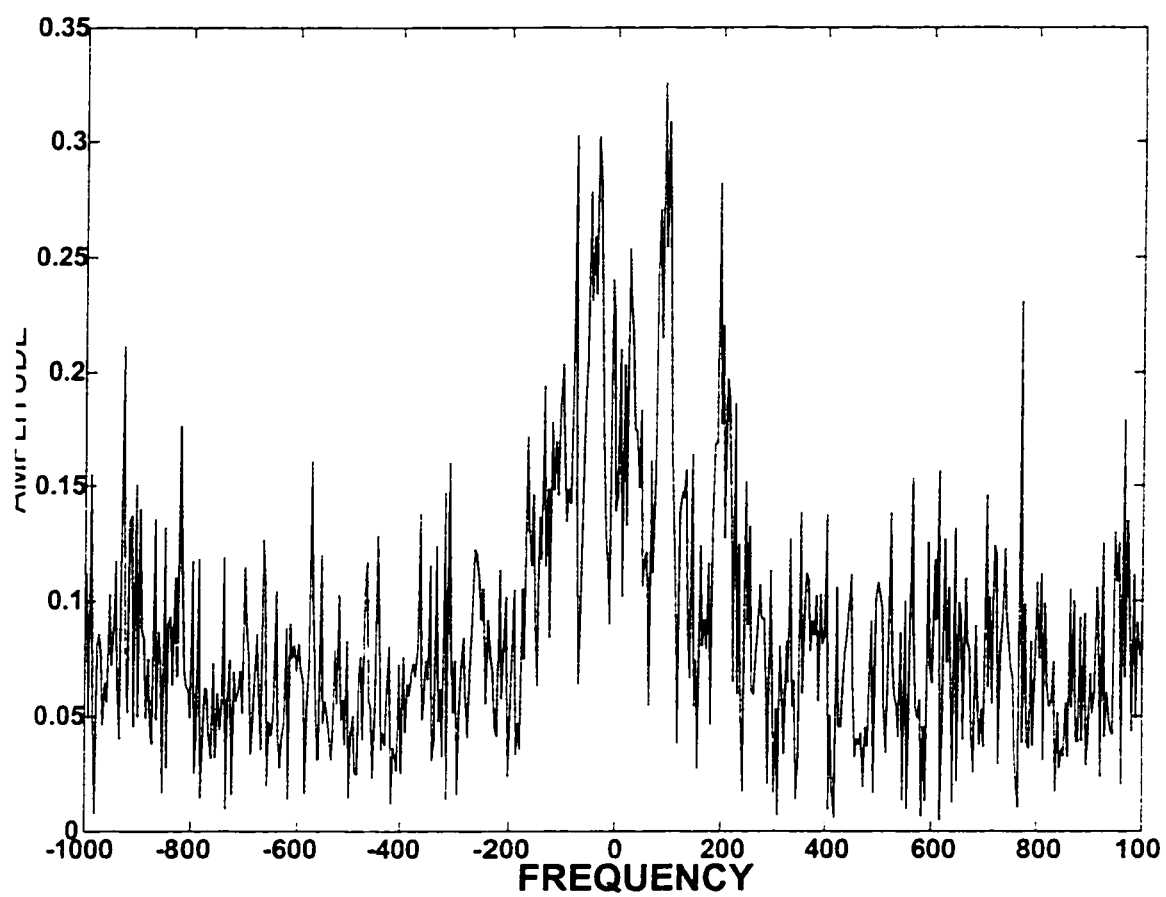


Figure 55: The spectrum of the real-life NMR-FID signal.

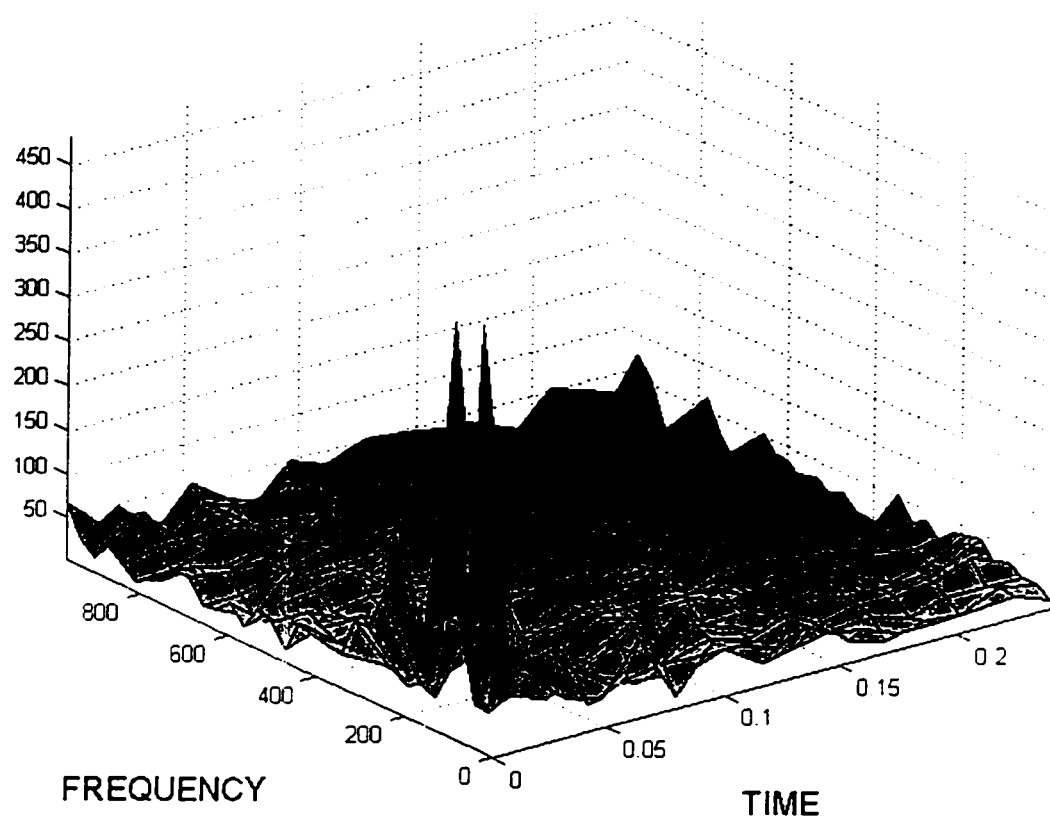


Figure 56: The transform coefficients (magnitude) for the same signal.

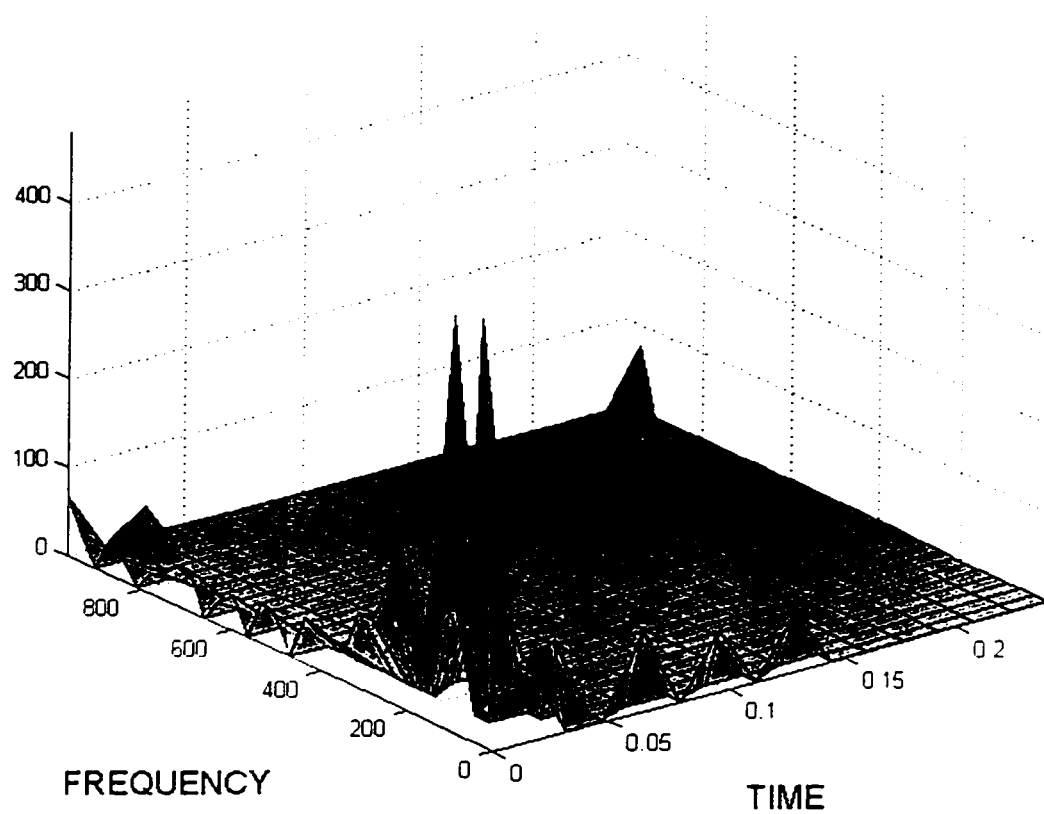


Figure 57: The transform coefficients of the same signal after thresholding with $thr = 66$.

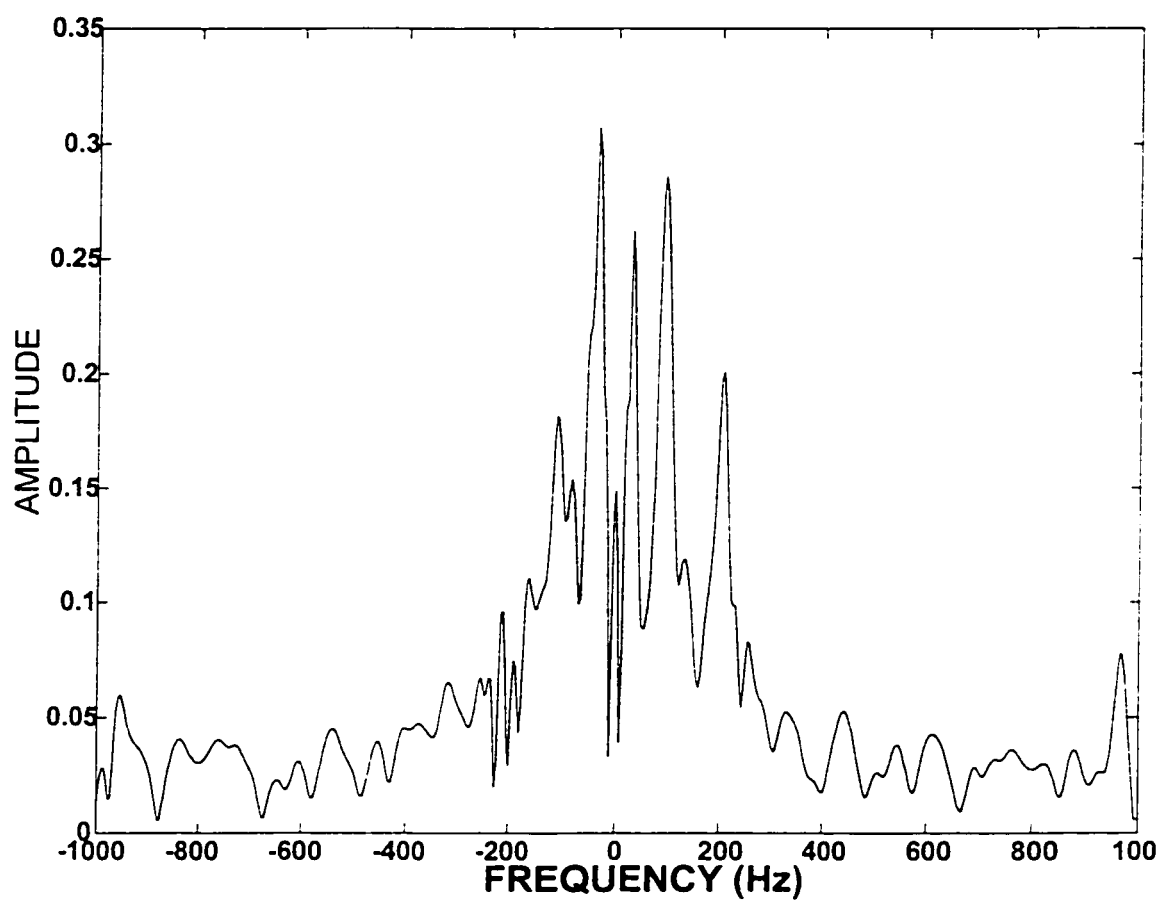


Figure 58: The resulting spectrum of the same signal after thresholding.

plotted in Fig. 59. Comparing this figure with Fig. 56, it is clear that in the case of our transform the coefficients which contains signal plus noise are more discriminable from the coefficients which contain noise only than in the case of the transform proposed in [44].

7.7 Conclusion

Noise reduction of NMR-FID signals using JTF transforms is a promising area since the nature of the signal makes a distinguished difference between the signal level and the noise level in the JTF coefficients. In particular, using the proposed JTF transform has the following substantial advantages like:

- The transform is linear. This means that getting back the signal from the transformed domain is straight forward. Recall that bilinear transforms share the problem of not being able to easily get the signal back from the transformed domain.
- The coefficients of the proposed transform are independent: This leads to the inverse transform being only a matter of matrix multiplication. This is in contrast to the over-sampled transforms where iterative methods are used for the inverse transform. This phenomena is discussed in details in subsubsection 2.6.1.1.
- The transform is stable: This ensures that no amplification of noise occurs during the forward or backward transformation. This is discussed in details in Section 3.5.
- The transform leads to a well-localized biorthogonal function, discussed in detail in Section 2.3. Consequently, the coefficients $a_{m,n}$ truly reflect the signal behavior in the

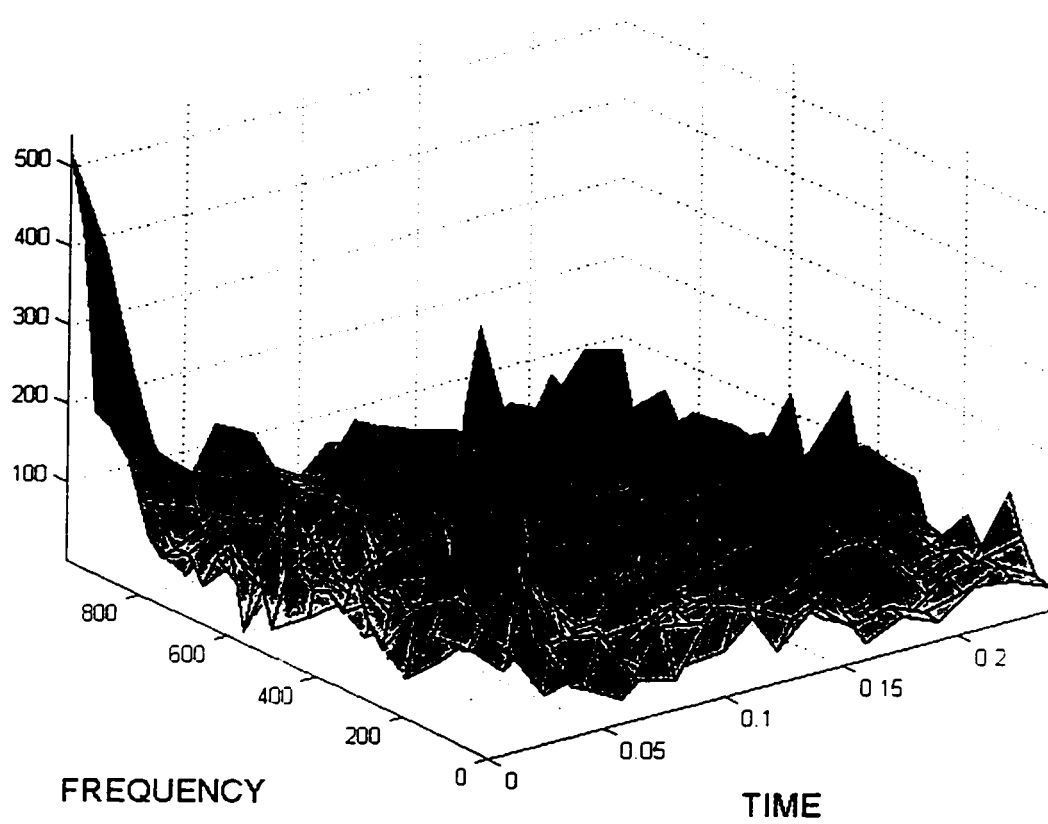


Figure 59: GGT coefficients of the NMR-FID signal.

vicinity of $[(m - \frac{1}{2}) \Delta_t, (m + \frac{1}{2}) \Delta_t] \times [(n - \frac{1}{2}) \Delta_f, (n + \frac{1}{2}) \Delta_f]$ in the JTF domain.

This, in turn, has two implications:

- (a) Signals which have few frequency components, like NMR signals, will be represented by fewer number of coefficients and hence the energy in these coefficients will be high. Thus, the difference between the energy of coefficients which contains signal plus noise and the energy of coefficients which contains noise only will be large.
- (b) When concluding that certain coefficients contain only noise, removing these coefficients will not have any effect on other coefficients which may contain a part of the required signal.

The proposed method has noticeable improvements over the method proposed in [44] regarding the SNR as well as the visual spectrum. Note that, using this simple thresholding technique needs enhancement. Our goal here, however, is to demonstrate the benefits of the proposed transform.

CHAPTER 8

CONCLUSION

A main problem of the Joint Time-Frequency (JTF) transforms is the lack of a "universal" JTF transform, i.e., a transform which is accepted in all branches of engineering, to be the counterpart of the Fourier transform in the time frequency domain. In this dissertation, our objective has been to develop JTF transforms with such properties that make them applicable to practically all branches of engineering. These properties have been summarized as follows

1. Concentrated analysis function in time and in frequency
2. Linearity
3. Independent coefficients
4. Concentrated dual function in time and in frequency
5. Stability
6. Tractable computation requirements.

Throughout this thesis, the modulation product of the Gaussian window with a harmonic kernel was chosen as the elementary function (which are the optimal elementary

function suggested by Gabor[3]). This choice ensures the **MOST concentrated analysis function in time and in frequency** as was proved in [3]. Also, we choose to expand time signals into an independent set composed of a time and frequency shifts of this elementary function. This choice results in meeting the first three requirements⁹. Thus, we are left with the last 3 requirements, that is: concentrated dual function in time and in frequency, stability, and tractable computational requirements which have not been met by any critical-sampled Gabor transform available in the literature. Our aim in this thesis has been to develop JTF transforms which maintain the first three properties and satisfy, as close as possible, the last three ones.

In Chapter 4, the non-separable sampling of the JTF plane for the real Gabor transform is introduced for the *aperiodic* critical-sampling case. It was shown that the hexagon sampling, in particular, enhances the localization of the biorthogonal function in the frequency domain while maintaining all other properties. An efficient method to calculate the transform coefficients for any type of windows is presented. We have also derived a practical implementation of the transform using a truncated version of the analysis window to be of length $2N$. We showed that this truncation has negligible effect on the characteristics of the transform. In addition, it requires only $L \{2 + \frac{1}{2} \log_2 N\}$ operations for computing the transform coefficients and $5.5N$ operations for computing the biorthogonal function). Thus, it is faster than any Gabor transform currently available. Unlike other methods of truncation, this method gives exact reconstruction of the original signal.

In Chapter 5, the stability has been considered with the objective of developing an orthogonal linear JTF transform (thus achieving the highest possible stability). The necessary

⁹ This choice is exactly the same of the critical-sampled Gabor transform

and sufficient orthogonality conditions on the analysis window function which will lead to orthogonal transform has been derived. Two functions satisfying these conditions are presented. In addition to its nice stability property, the resulting transform is proven to be computationally attractive than any other currently available Gabor transforms. Compared to the Zak Transform based method, the computational saving ratio is $\frac{1+\log M+\frac{1}{2}\log_2 N}{2+\frac{1}{2}\log_2 N}$. It is worthy to note that this transform leads to an exact representation of the signal, i.e., using this transform leads to an exact reconstruction of the signal.

In Chapter 6, we have concentrated on how to meet all the requirements simultaneously. Thus, using alternate types of kernels, a *stable, linear, critically-sampled*, JTF transform with *localized biorthogonal function* and *analysis function* has been developed which overcomes the main problem of the other implementations. An efficient method to calculate the biorthogonal function for any type of window is presented. An inherent characteristic of this implementation is that a truncated version of the modulating window to a length of $2N$ leads to a biorthogonal function with the same length. Using this truncated Gaussian window and its biorthogonal function results in an algorithm which requires $L(2 + \frac{1}{2}\log_2 N)$ operations for computing transform coefficients and $5N$ operations for computing the biorthogonal function. This is faster than any other algorithm currently available in the literature. The effect of this truncation on the transform coefficients has been studied. It is worth noting that this truncated window function transform leads to an exact representation of the signal.

The JTF transform proposed in Chapter 6 has a good balance of all the requirements. Its analysis function is Gaussian which is the most concentrated function in the JTF domain (this indicates the highest resolution that could ever be achieved). Its biorthogonal function

was shown to have excellent localization in the JTF domain (this ensures that the transform will faithfully describe the signal local behavior). Also, the transform was shown to have excellent stability performance (the condition number is around 1.18 which is very close to be orthogonal). In addition to these qualities, the transform is linear and have independent coefficients. Thus, it is considered as the best one among the three and its computational requirements were thoroughly studied.

The hexagon-sampling transform is the worst among the three. It, however, gives an excellent example that rebuffs the widely accepted claim that the Gabor transform is the only transform that meets the optimality conditions derived by Gabor [3]. In this transform we maintain everything the same as the Real Gabor transform except changing the location of the sampling points, and thus the optimality conditions have been maintained. We showed how careful choice of the sampling point could lead to a better transform. We expect that extending this idea to the multidimensional signals will give even better results.

To demonstrate the usefulness of the proposed transforms in real-life situation, the third transform has been applied, in Chapter 7, to the traditional, yet difficult, problem of noise reduction of the nuclear magnetic resonance signals. It is shown that the proposed transform gives far better results with lower computational requirements than other JTF transforms.

8.1 Recommendations and Future Work

1. In Chapter 5, we derive the necessary and sufficient orthogonality conditions on the analysis window function which will lead to orthogonal transform. It is still, however,

an open area to choose the analysis window function that satisfies these requirements and maintains other optimal characteristics.

2. For the proposed transform to be accepted as the natural replacement of the Fourier transform for time variant systems, it needs a thorough study of its characteristics like, shift properties, linear and circular convolutions, . . .etc.
3. It is proposed that hardware implementation for computing the proposed JTF coefficients is to be investigated with the objective of reducing the computation time.
4. In this thesis, we focus on one-dimensional signals. Extending the work into two-dimensional signals is required. Note that direct extension into two-dimensional signals is straightforward. However, utilizing the added degree of freedom in positioning the elementary functions in the four-dimensional JTF space needs extra work.

APPENDICES

APPENDIX A: Permutation Matrices

Our developments in the thesis involve certain data movements such as the interchange of two columns or two rows. The permutation matrix [47] is used to describe this type of operation.

Definition A.1

A permutation matrix is the identity matrix with its rows re-ordered, e.g.

$$\mathbf{P} = \begin{bmatrix} 0 & 0 & 0 & 1 \\ 1 & 0 & 0 & 0 \\ 0 & 0 & 1 & 0 \\ 0 & 1 & 0 & 0 \end{bmatrix}$$

Permutation matrices are orthogonal, i.e., $\mathbf{P}^{-1} = \mathbf{P}^T$.

Let \mathbf{P} be an $n \times n$ permutation matrix. If A is a $n \times n$ general matrix, then

$\mathbf{P}A$ is a row permuted version of A

$A\mathbf{P}$ is a column permuted version of A

An efficient way to store or represent a general $n \times n$ permutation matrix \mathbf{P} is by its encoding vector p .

Definition A.2

An encoding vector p is a n -vector whose element $p(k)$ is the column index of the sole "1" in the \mathbf{P} 's k^{th} row.

Thus $p = [4, 1, 3, 2]$ is the encoding vector of the above \mathbf{P} .

One famous example of the permutation matrix, which is extensively used throughout

this thesis, is the anti-diagonal identity matrix J defined by

$$J = \begin{bmatrix} 0 & \cdots & 0 & 1 \\ 0 & \cdots & 1 & 0 \\ \vdots & \diagup & \vdots & \vdots \\ 1 & \cdots & 0 & 0 \end{bmatrix} \quad (\text{A-1})$$

Let J be an $n \times n$ permutation matrix. If A is a $n \times n$ general matrix, then

$$JA \triangleq \text{flip } A \text{ in up/down direction (rows flipped).}$$

$$AJ \triangleq \text{flip } A \text{ in left/right direction (columns flipped).}$$

Example 8.1

Let

$$A = \begin{bmatrix} 1 & 2 & 3 \\ 4 & 5 & 6 \\ 7 & 8 & 9 \end{bmatrix}$$

flipping A in up/down direction or JA is

$$JA = \begin{bmatrix} 7 & 8 & 9 \\ 4 & 5 & 6 \\ 1 & 2 & 3 \end{bmatrix}$$

while flipping A in left/right direction or AJ is

$$AJ = \begin{bmatrix} 3 & 2 & 1 \\ 6 & 5 & 4 \\ 9 & 8 & 7 \end{bmatrix}$$

It can be proved that, $J^{2k} = I$, $J^{2k+1} = J$, and $J^T = J$.

APPENDIX B: Circulant Matrices and Toeplitz Matrices

Matrices whose entries are constant along each diagonal arise in many applications. They have two cases.

Definition B.1

The $n \times n$ matrix A is *Circulant* if A is of the form

$$A = \begin{bmatrix} a_0 & a_{n-1} & \cdots & a_1 \\ a_1 & a_0 & \cdots & a_2 \\ \vdots & \vdots & \ddots & \vdots \\ a_{n-1} & a_{n-2} & \cdots & a_0 \end{bmatrix}$$

Any circulant matrix can be represented by the n -dimensional vector $\{a_0, a_1, \dots, a_{n-1}\}$.

Any circulant matrix is diagonalizable over \mathcal{C} (i.e., semi-simple) by the Discrete Fourier Transform, i.e.,

$$E_n A E_n^* = \begin{bmatrix} b_0 & 0 & \cdots & 0 \\ 0 & b_1 & \cdots & 0 \\ \vdots & \vdots & \ddots & \vdots \\ 0 & 0 & \cdots & b_{n-1} \end{bmatrix}$$

where $E_N = [e_{n,k}]_{N \times N}$ is the N -point Discrete Fourier Transform (DFT) matrix with $e_{n,k}$ given by

$$e_{n,k} = \sqrt{\frac{1}{N}} \exp\left(\frac{-j2\pi nk}{N}\right) \quad n, k = 0, 1, \dots, N-1 \quad (\text{B-1a})$$

Definition B.2

The $n \times n$ matrix A is *Toeplitz* if A is of the form

$$A = \begin{bmatrix} a_0 & a_{-1} & \cdots & a_{-n+1} \\ a_1 & a_0 & \cdots & a_{-n+2} \\ \vdots & \vdots & \ddots & \vdots \\ a_{n-1} & a_{n-2} & \cdots & a_0 \end{bmatrix}$$

Any Toeplitz matrix can be represented by the $(2n - 1)$ -dimensional vector

$$\{a_{-n+1}, \dots, a_{-1}, a_0, a_1, \dots, a_{n-1}\}$$

A generalization of the above two definitions is the block-Circulant and the block-Toeplitz matrices.

Definition B.3

The $nm \times nm$ matrix \mathbf{A} is *block-Circulant* of type (m, n) if \mathbf{A} is of the form

$$\mathbf{A} = \begin{bmatrix} A_0 & A_{n-1} & \cdots & A_1 \\ A_1 & A_0 & \cdots & A_2 \\ \vdots & \vdots & \ddots & \vdots \\ A_{n-1} & A_{n-2} & \cdots & A_0 \end{bmatrix}$$

where A_0, A_1, \dots, A_{n-1} is an $m \times m$ matrices

Any block-circulant matrix can be represented by the $nm \times m$ matrices $\{A_0, A_1, \dots, A_{n-1}\}$

Any block-circulant matrix is diagonalizable over \mathcal{C} (i.e., semi-simple) by the Discrete Fourier Transform, see theorem 5.6.4 of [40] page 180, i.e.,

$$(E_n \otimes E_m) \mathbf{A} (E_n \otimes E_m)^* = \begin{bmatrix} B_0 & 0 & \cdots & 0 \\ 0 & B_1 & \cdots & 0 \\ \vdots & \vdots & \ddots & \vdots \\ 0 & 0 & \cdots & B_{n-1} \end{bmatrix}$$

where B_k are arbitrary $m \times m$ square matrices

Definition B.4

The $n \times n$ matrix \mathbf{A} is *block-Toeplitz* if \mathbf{A} is of the form

$$\mathbf{A} = \begin{bmatrix} A_0 & A_{-1} & \cdots & A_{-n+1} \\ A_1 & A_0 & \cdots & A_{-n+2} \\ \vdots & \vdots & \ddots & \vdots \\ A_{n-1} & A_{n-2} & \cdots & A_0 \end{bmatrix}$$

where $A_{-n+1}, \dots, A_0, \dots, A_{n-1}$ is $m \times m$ matrices.

Block-Toeplitz matrix can be represented by the $m \times (2n - 1) m$ matrices

$$\{A_{-n+1}, \dots, A_{-1}, A_0, A_1, \dots, A_{n-1}\}$$

APPENDIX C: Discrete Critically-Sampled Gabor Transforms

As we have seen in Section 3.2, any Gabor transform implementation can be put in the matrix notation

$$\mathbf{x} = \mathbf{H} \mathbf{E}^T \mathbf{a}$$

This is called the synthesis equation. Its inverse, the analysis equation, is

$$\mathbf{a} = \mathbf{E} \mathbf{H}^{-1} \mathbf{x} \quad (\text{analysis equation})$$

Both \mathbf{H} , \mathbf{H}^{-1} and \mathbf{E} are different for different cases as detailed below.

C.1. Periodic Complex Gabor Transform

The discrete version of the complex Gabor expansion (2.14) is

$$x(k) = \sum_{m=0}^{M-1} h(k - mN) \sum_{n=0}^{N-1} a_{m,n} \exp \frac{j2\pi nk}{N} \quad (\text{C-1})$$

The above equation was put in matrix formulation by [27] which gave the synthesis equation (3.1) and the analysis equation (3.9), where \mathbf{H} is a block-circulant matrix

$$\mathbf{H} \triangleq \begin{pmatrix} H_0 & H_{M-1} & \cdots & H_1 \\ H_1 & H_0 & \cdots & H_2 \\ \vdots & \vdots & \ddots & \vdots \\ H_{M-1} & H_{M-2} & \cdots & H_0 \end{pmatrix} \quad (\text{C-2})$$

H_m is as given in (3.6) \mathbf{E} is a block-diagonal matrix

$$\mathbf{E} = \begin{bmatrix} E_N & & & \\ & E_N & & \\ & & \ddots & \\ & & & E_N \end{bmatrix} \quad (\text{C-3})$$

where $E_N = [e_{n,k}]_{N \times N}$ is the N -point Discrete Fourier Transform (DFT) matrix defined in (B-1a). Since \mathbf{H} is a square matrix, it has a unique inverse \mathbf{H}^{-1} which is also a $MN \times MN$ block-circulant matrix

$$\mathbf{\Gamma} = \mathbf{H}^{-1} \triangleq \begin{pmatrix} \Gamma_0 & \Gamma_1 & \cdots & \Gamma_{M-1} \\ \Gamma_{M-1} & \Gamma_0 & \cdots & \Gamma_{M-2} \\ \vdots & \vdots & \ddots & \vdots \\ \Gamma_1 & \Gamma_2 & \cdots & \Gamma_0 \end{pmatrix} \quad (\text{C-4})$$

with diagonal $N \times N$ blocks Γ_m is given by

$$\Gamma_m = \text{diag}(\gamma(mN), \gamma(mN+1), \dots, \gamma(mN+N-1))$$

The sequence $\gamma(k)$ is the resulting discrete biorthogonal function which is plotted in Fig. 60 for $M = N = 8$ and $\sigma = N$.

C.2. Aperiodic Complex Gabor Transform

The previous implementation was named periodic implementation because it involves a periodization of the window function as well as the analyzed signal, i.e., the signal $x(k)$ and $h(k)$ have periodicity L . According to [19], for the Gabor transform, the assumption of periodicity is a more radical assumption than for the Fourier transform, as it involves a substantial change from the natural structure of the transform. Another implementation

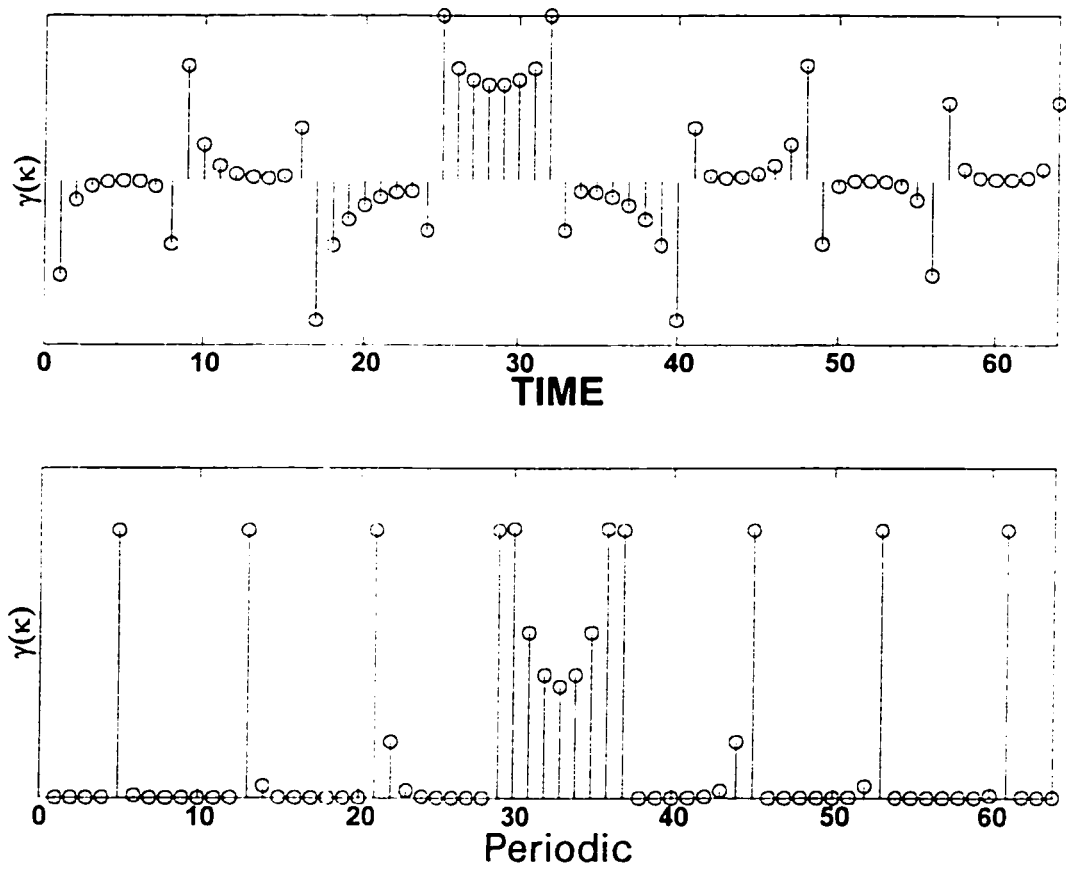


Figure 60: The discrete biorthogonal function of periodic complex Gabor transform centered on the analysis window $m = 3$.

which does not assume the periodicity of the window nor the analyzed signal was proposed in [19, 28]. It gives the same equations as the above case except that \mathbf{H} is block-Toeplitz matrix defined by

$$\mathbf{H} \triangleq \begin{pmatrix} H_0 & H_{-1} & \cdots & H_{-M+1} \\ H_1 & H_0 & \cdots & H_{-M+2} \\ \vdots & \vdots & \ddots & \vdots \\ H_{M-1} & H_{M-2} & \cdots & H_0 \end{pmatrix} \quad (\text{C-5})$$

The matrix \mathbf{H}^{-1} is not, in general, block-Toeplitz. \mathbf{H}^{-1} can be written as

$$\mathbf{\Gamma} = \mathbf{H}^{-1} \triangleq \begin{pmatrix} \Gamma_0^{(0)} & \Gamma_1^{(0)} & \cdots & \Gamma_{M-1}^{(0)} \\ \Gamma_{-1}^{(1)} & \Gamma_0^{(1)} & \cdots & \Gamma_{M-2}^{(1)} \\ \vdots & \vdots & \ddots & \vdots \\ \Gamma_{-M+1}^{(M-1)} & \Gamma_{-M+2}^{(M-1)} & \cdots & \Gamma_0^{(M-1)} \end{pmatrix} \quad (\text{C-6})$$

with $\Gamma_l^{(m)}$ is given by

$$\Gamma_l^{(m)} = \text{diag}(\gamma_m(lN), \gamma_m(lN + 1), \dots, \gamma_m(lN + N - 1))$$

The sequence $\gamma_m(k)$ is the resulting biorthogonal function for m time shift. This implementation leads to almost the same biorthogonal function as the previous case except that it is not periodic. For comparison with the periodic case, the aperiodic and the periodic cases for $M = N = 8$ are plotted in the Fig. 61

C.3. Periodic Real Gabor Transform

Instead of expanding real signals into the modulation product of the Gaussian window with the orthogonal set $\left\{ \cos \frac{2\pi n t}{T}, \sin \frac{2\pi(n+\frac{1}{2})t}{T} \right\}_{n \in \mathbb{Z}}$, as Gabor did in his 2nd expansion (2.18),

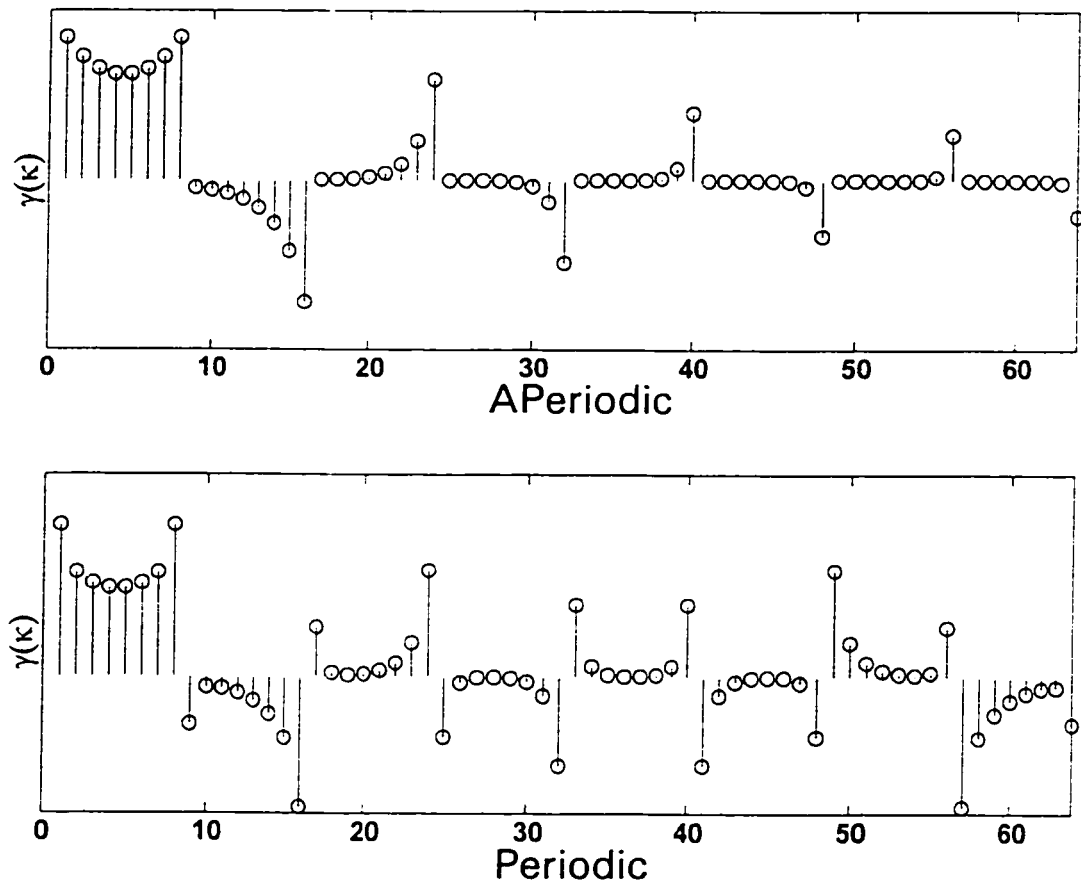


Figure 61: The biorthogonal function of the periodic and the aperiodic complex Gabor Transform centred on the analysis window $m = 3$.

Stewart *et al.* [25] used the complete orthogonal set $\{\cos \frac{\pi nt}{T}\}_{n \in \mathbb{Z}}$ instead. The discrete expansion equation is

$$x(k) = \sum_{m=0}^{M-1} h(k - mN) \left[\sum_{n=0}^{N-1} a_{m,n} \sqrt{\frac{2}{N}} \cos \frac{\pi n(k + \frac{1}{2})}{N} + a_{m,0} \sqrt{\frac{1}{N}} \right] \quad (\text{C-7})$$

which gives

$$\mathbf{H} \triangleq \begin{pmatrix} H_0 & H_{M-1}J & \cdots & H_1J \\ H_1J & H_0 & \cdots & H_2 \\ \vdots & \vdots & \ddots & \vdots \\ H_{M-1}J & H_{M-2} & \cdots & H_0 \end{pmatrix} \quad (\text{C-8})$$

$$\mathbf{H}^{-1} \triangleq \begin{pmatrix} \Gamma_0 & J\Gamma_1 & \cdots & J\Gamma_{M-1} \\ J\Gamma_{M-1} & \Gamma_0 & \cdots & \Gamma_{M-2} \\ \vdots & \vdots & \ddots & \vdots \\ J\Gamma_1 & \Gamma_2 & \cdots & \Gamma_0 \end{pmatrix} \quad (\text{C-9})$$

and

$$\mathbf{E} = \begin{bmatrix} C & & & \\ & CJ & & \\ & & \ddots & \\ & & & C \\ & & & & CJ \end{bmatrix}$$

where C is defined in (3.15). The function $\gamma(k)$ may be thought of as the resulting biorthogonal function which is plotted in Fig. 62 for $M = N = 8$ and $\sigma = N$.

C.4. Aperiodic Real Gabor Transform

This was developed in Section 3.3 on page 46.

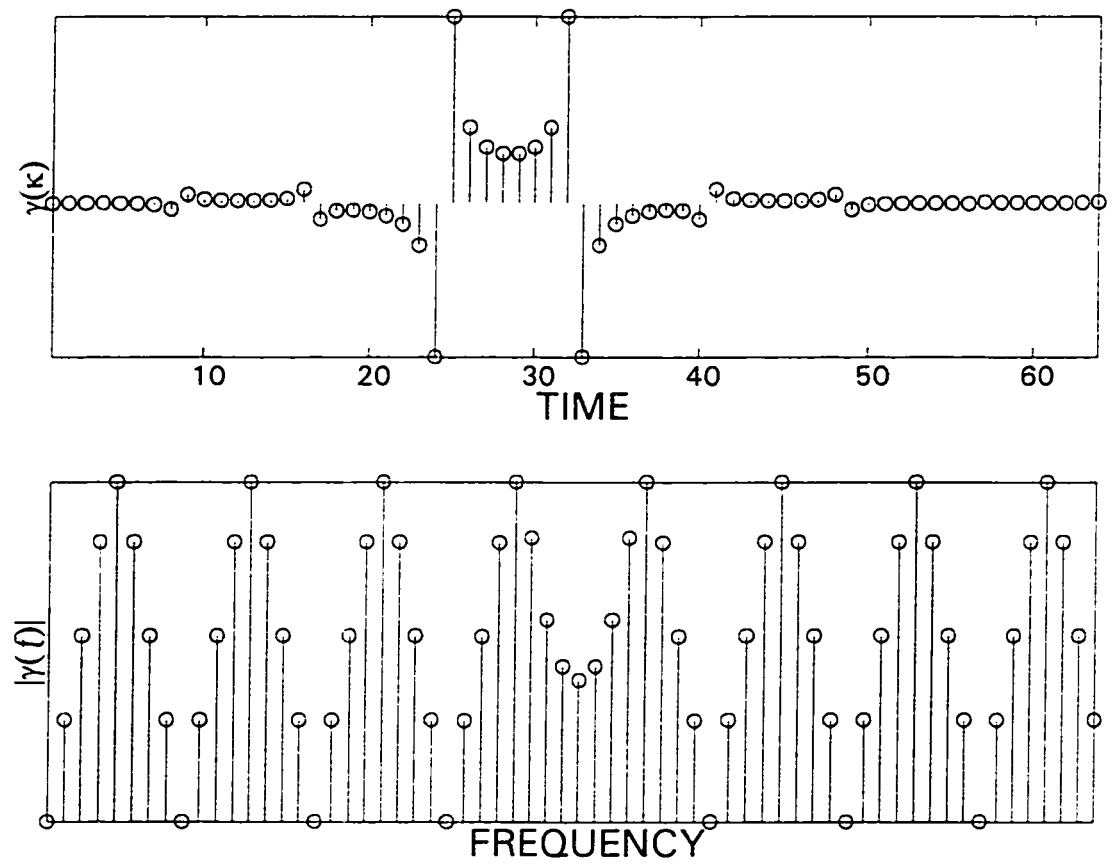


Figure 62: The discrete biorthogonal function of periodic real Gabor transform centered on the analysis window $m = 3$.

APPENDIX D: Discrete Over-Sampled Gabor Transform

In the over-sampling Gabor transform [16,26], the sampling distances in time and frequency become more denser than the case of the original, *critical-sampling*, Gabor expansion. In the over-sampling case, the dual function is not unique. This solves the problem by choosing a dual function which is closest in norm to the Gaussian window. The price to be paid is high redundancy and linear dependence among the coefficients. For a signal $x(k)$ of length $L = M\bar{N}$ with M shifts of the modulated Gaussian pulse and the number of frequency components in each shift is N where $N \geq \bar{N}$. The ratio N/\bar{N} represents the over-sampling rate (OVSR). Thus, there are $M\bar{N}$ sample point and MN Gabor coefficients. The over-sampling case of the complex Gabor expansion (2.14) was put in matrix formulation by [29] which gives, \mathbf{H} as the $M\bar{N} \times MN$ block matrix

$$\mathbf{H} \triangleq \begin{pmatrix} H_{0,0} & H_{0,1} & \cdots & H_{0,M-1} \\ H_{1,0} & H_{1,1} & \cdots & H_{1,M-1} \\ \vdots & \vdots & \ddots & \vdots \\ H_{\bar{M}-1,0} & H_{\bar{M}-1,1} & \cdots & H_{\bar{M}-1,M-1} \end{pmatrix} \quad (\text{D-1})$$

where $\bar{M} = M\bar{N}/N$. Each block is a $N \times N$ diagonal matrix $H_{m,n}$ defined by

$$H_{m,n} \triangleq \text{diag} (h(mN - n\bar{N}), h(mN - n\bar{N} + 1), \dots, h(mN - n\bar{N} + N - 1)) \quad (\text{D-2})$$

where $h(k)$ is as defined in (3.8). Here \mathbf{H} is not a square matrix and one can define many pseudo inverses \mathbf{H}^{-1} . Each one of them will result in a different biorthogonal function. \mathbf{H}^{-1}

has to be a right inverse of \mathbf{H} , i.e., $\mathbf{H}\mathbf{H}^{-1} = \mathbf{I}$. One solution is the least mean error solution

$$\mathbf{H}^{-1} = \mathbf{H}^T (\mathbf{H}\mathbf{H}^T)^{-1}$$

which is proved to give the optimal biorthogonal function in the sense of the least mean square error [29]. \mathbf{H}^{-1} has the structure

$$\mathbf{H}^{-1} \triangleq \begin{pmatrix} \Gamma_{0,0} & \Gamma_{0,1} & \cdots & \Gamma_{0,\tilde{M}-1} \\ \Gamma_{1,0} & \Gamma_{1,1} & \cdots & \Gamma_{1,\tilde{M}-1} \\ \vdots & \vdots & \ddots & \vdots \\ \Gamma_{M-1,0} & \Gamma_{M-1,1} & \cdots & \Gamma_{M-1,\tilde{M}-1} \end{pmatrix}$$

where $\Gamma_{m,n}$ is a $N \times N$ diagonal matrix.

The matrix \mathbf{E} is $MN \times MN$ block-diagonal matrix

$$\mathbf{E} = \begin{bmatrix} E_N & & & \\ & E_N & & \\ & & \ddots & \\ & & & E_N \end{bmatrix}$$

where E_N is the N -point DFT matrix defined in (B-1a). The resulting discrete biorthogonal function for $\text{OVSF} = 4$ is plotted in Fig. 63 for $M = N = 8$, $\text{OVSF} = 4$, and $\sigma = N$. The figure show the superiority of the this biorthogonal function over all critically sampling cases.

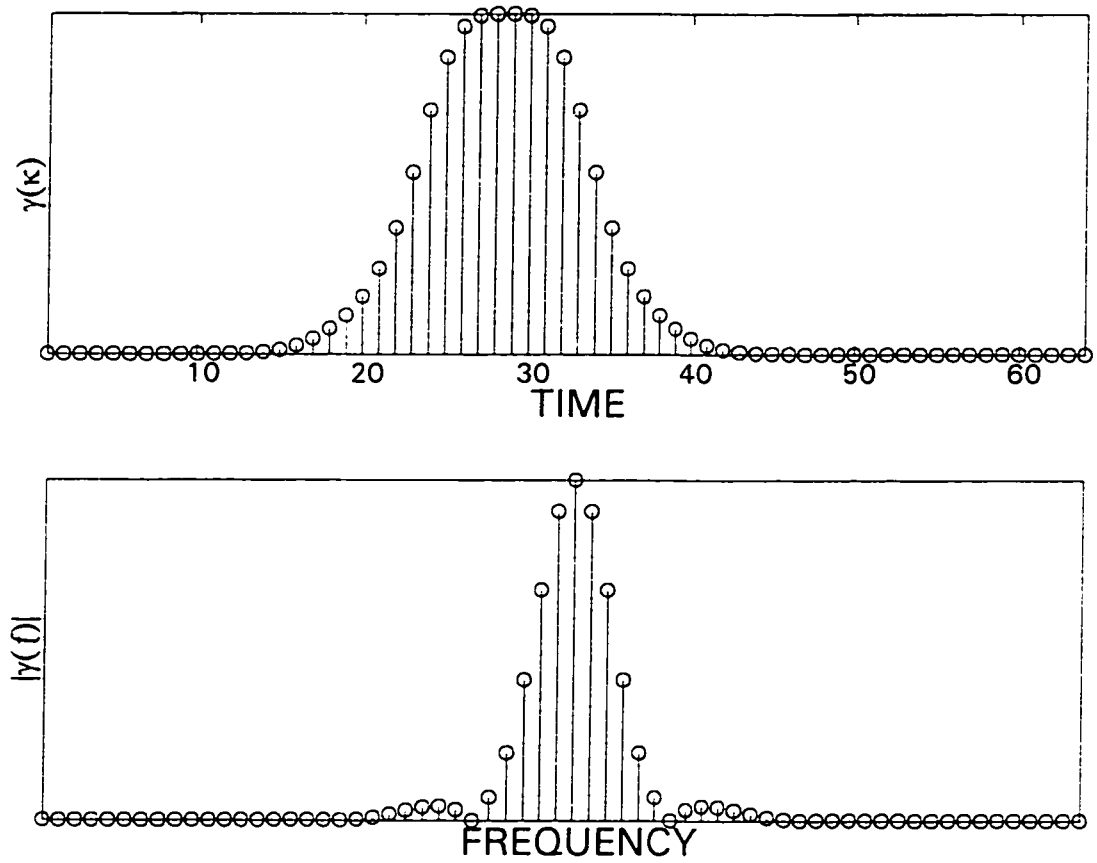


Figure 63: The discrete biorthogonal function of the over-sampling case, $\mathcal{OVS}\mathcal{R} = 4$.

APPENDIX E: Discrete Cosine Transform Type IV

Discrete cosine transform type IV (DCT-IV), also referred to as even discrete cosine transform-2 (EDCT-2), was introduced by Jain [48]. DCT-IV of an N -point real sequence $x(n)$, $n = 0, 1, \dots, N - 1$ is defined as:

$$X(k) = \sqrt{\frac{2}{N}} \sum_{n=0}^{N-1} x(n) \cos \frac{\pi (k + \frac{1}{2})(n + \frac{1}{2})}{N} \quad (\text{E-1})$$

$$x(n) = \sqrt{\frac{2}{N}} \sum_{k=0}^{N-1} X(k) \cos \frac{\pi (k + \frac{1}{2})(n + \frac{1}{2})}{N} \quad (\text{E-2})$$

DCT-IV has found several applications in signal processing [49]. Several algorithms are available in the literature for efficient calculation of this transform [50, 51]. It is easy to prove the following DCT-IV properties

$$\begin{aligned} x(k + N) &= \sqrt{\frac{2}{N}} \sum_{n=0}^{N-1} X(n) \cos \frac{\pi (N + k + \frac{1}{2})(n + \frac{1}{2})}{N} \\ &= -\sqrt{\frac{2}{N}} \sum_{n=0}^{N-1} X(n) \cos \frac{\pi ((N - 1 - k) + \frac{1}{2})(n + \frac{1}{2})}{N} \end{aligned} \quad (\text{E-3a})$$

$$\begin{aligned} x(k + 2N) &= \sqrt{\frac{2}{N}} \sum_{n=0}^{N-1} X(n) \times \cos \left(\frac{\pi (k + \frac{1}{2})(n + \frac{1}{2})}{N} + \pi (n + \frac{1}{2}) \right) \\ &= -\sqrt{\frac{2}{N}} \sum_{n=0}^{N-1} X(n) \times \cos \frac{\pi (k + \frac{1}{2})(n + \frac{1}{2})}{N} \end{aligned} \quad (\text{E-3b})$$

$$\begin{aligned} x(k + 3N) &= \sqrt{\frac{2}{N}} \sum_{n=0}^{N-1} X(n) \times \cos \left(\frac{\pi (k + \frac{1}{2})(n + \frac{1}{2})}{N} + 3\pi (n + \frac{1}{2}) \right) \\ &= \sqrt{\frac{2}{N}} \sum_{n=0}^{N-1} X(n) \times \cos \frac{\pi ((N - 1 - k) + \frac{1}{2})(n + \frac{1}{2})}{N} \end{aligned} \quad (\text{E-3c})$$

APPENDIX F: Discrete Sine Transform Type IV (DST-IV)

Discrete sine transform type IV (DST-IV), also referred to as even discrete sine transform-3 (EDST-3), was introduced by Jain [48]. DST-IV of an N -point real sequence $x(n)$, $n = 0, 1, \dots, N - 1$ is defined as:

$$X(k) = \sqrt{\frac{2}{N}} \sum_{n=0}^{N-1} x(n) \sin \frac{\pi (k + \frac{1}{2}) (n + \frac{1}{2})}{N} \quad (\text{F-4})$$

where $X(k)$ is the DST-IV transform of the sequence $x(n)$. The inverse of (F-4) is

$$x(n) = \sqrt{\frac{2}{N}} \sum_{k=0}^{N-1} X(k) \sin \frac{\pi (k + \frac{1}{2}) (n + \frac{1}{2})}{N} \quad (\text{F-5})$$

DST's has found several applications in signal and image coding [49], and in adaptive filtering [52]. Several algorithms are available in the literature for efficient calculation of this transform [50, 51]. It is easy to prove the following DST-IV properties

$$x(k + N) = \sqrt{\frac{2}{N}} \sum_{n=0}^{N-1} X(n) \sin \frac{\pi ((N - 1 - k) + \frac{1}{2}) (n + \frac{1}{2})}{N} \quad (\text{F-6a})$$

$$x(k + 2N) = -\sqrt{\frac{2}{N}} \sum_{n=0}^{N-1} X(n) \sin \frac{\pi (k + \frac{1}{2}) (n + \frac{1}{2})}{N} \quad (\text{F-6b})$$

$$x(k + 3N) = -\sqrt{\frac{2}{N}} \sum_{n=0}^{N-1} X(n) \sin \frac{\pi ((N - 1 - k) + \frac{1}{2}) (n + \frac{1}{2})}{N} \quad (\text{F-6c})$$

APPENDIX G: Generalized Gabor Transform

In [44], the authors used the periodic complex Gabor transform (C-1). They, however, replaced the Gaussian window function by a one sided exponential function, i.e.,

$$h(k) \triangleq \exp(-\pi d_1 \Delta_t k) \quad (\text{G-7})$$

where d_1 is the exponent constant and Δ_t is the sampling interval. This function is plotted in Fig. 64. This transform as the periodic complex Gabor transform (Appendix C.1) can be expressed in matrix formulation as

$$\mathbf{x} = \mathbf{H} \mathbf{E}^T \mathbf{a} \quad (\text{synthesis equation}) \quad (\text{G-8})$$

where \mathbf{H} and \mathbf{E} are as defined in (C-2) and (C-3) respectively. To measure the stability of the transform, we calculate the condition number $\kappa(\mathbf{H}\mathbf{E}^T)$ of the matrix $[\mathbf{H}\mathbf{E}^T]$. $\kappa(\mathbf{H}\mathbf{E}^T)$ varies widely with the parameter d_1 . Recalling that d is a design parameter depending on the nature of the problem thus one can not set it on a predefined optimum value. $\kappa(\mathbf{H}\mathbf{E}^T)$ for one sided exponential function and typical values of M , N and d for this transform are listed in Table 10. As seen from the table, the condition number is very high and increases unboundedly with increasing N and M which indicates the instability of the transform.

The resulting biorthogonal function has nice concentration in time domain, Fig. 65. In the frequency domain, however, the biorthogonal function has bad localization. As a consequence, the JTF domain is expected to be distorted.

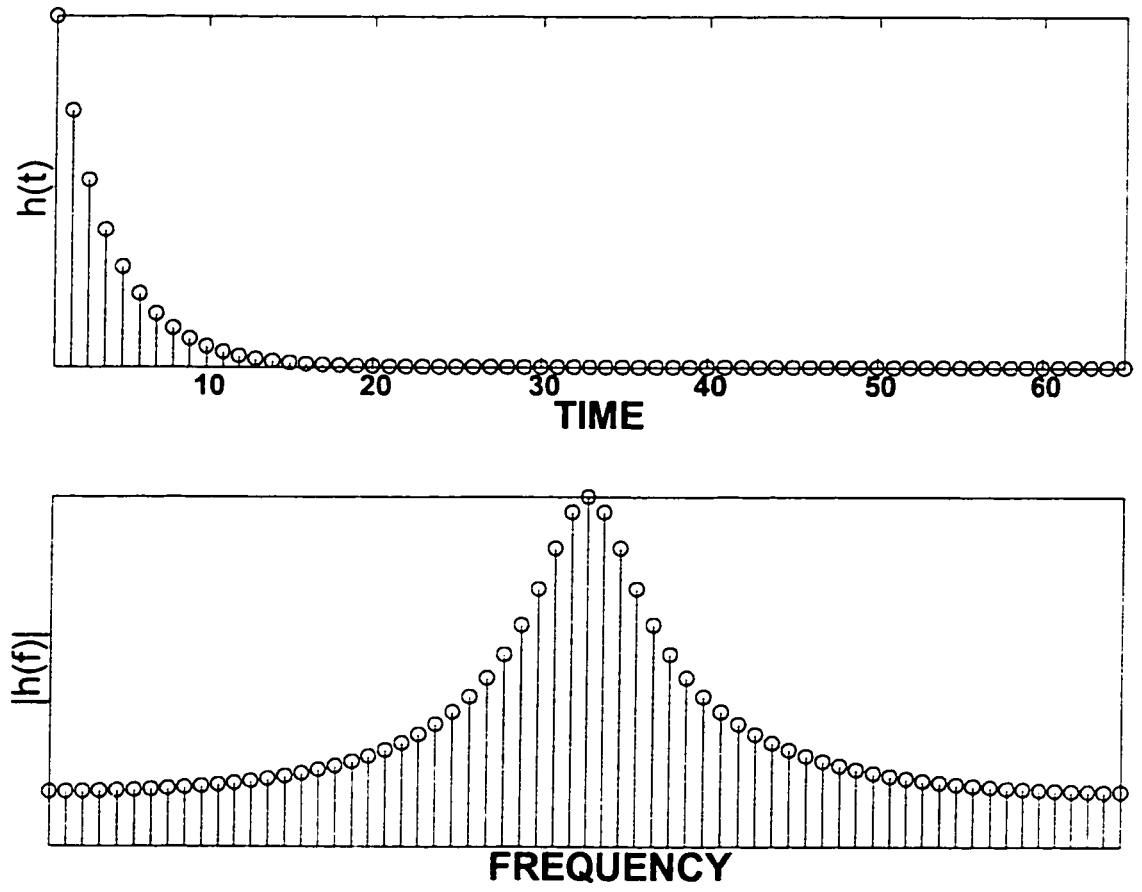


Figure 64: The analysis window function used in GGT.

(N, M)	$\kappa(\mathbf{H}\mathbf{E}^T)$	
	$d_1 = 33$	$d_1 = 10$
(8, 32)	24.39	34.46
(16, 16)	16.01	19.17
(16, 32)	24.47	34.49
(32, 16)	16.04	19.18
(32, 32)	24.51	34.51
(64, 64)	32.52	57.66
(128, 64)	32.53	57.67
(256, 128)	37.56	85.46

TABLE 10: Condition number of the GGT

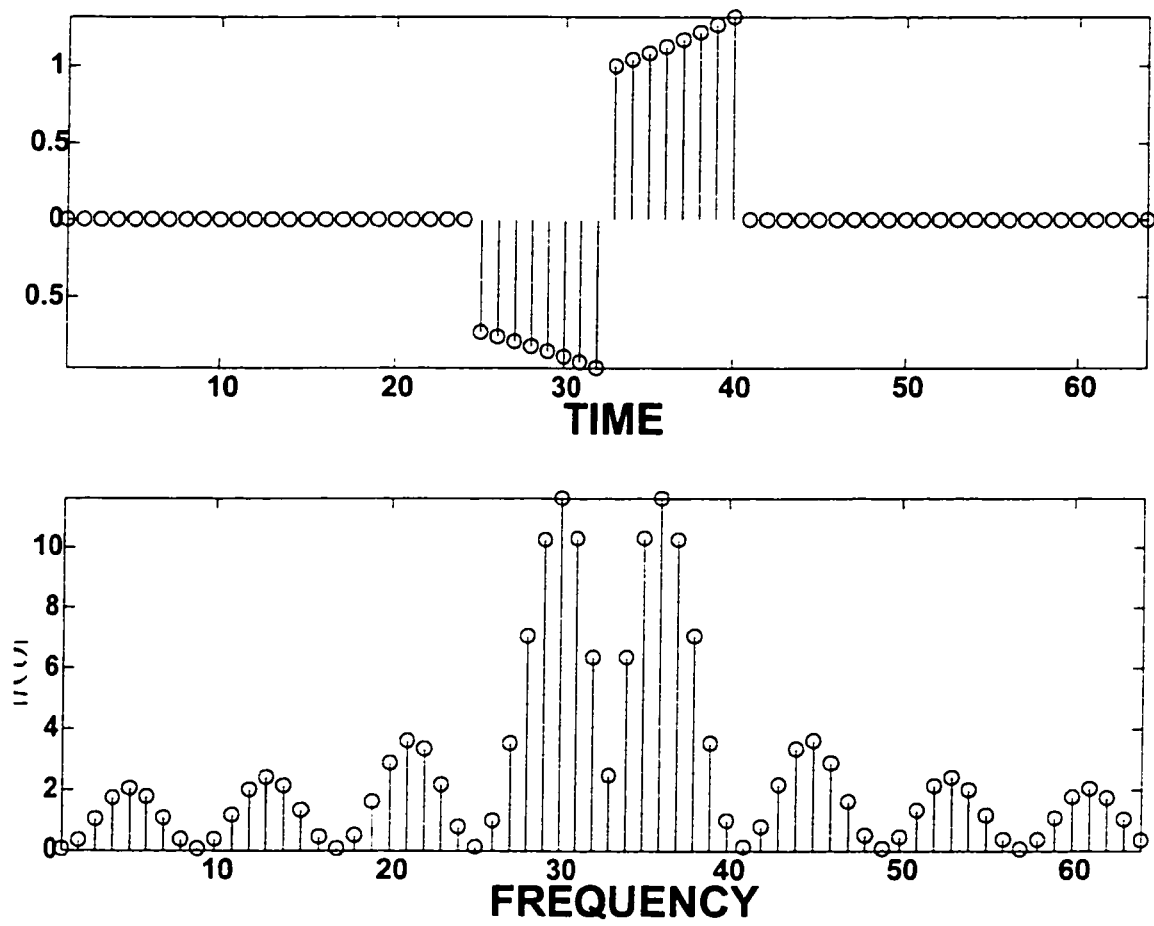


Figure 65: The discrete biorthogonal function of GGT.

REFERENCES

1. S. Qian and D. Chen, *Joint Time-Frequency Analysis: Methods and Applications*, Prentice Hall PTR, 1996.
2. A. V. Oppenheim and R. W. Schaffer, *Discrete-Time Signal Processing*, Prentice Hall signal processing series, 1989.
3. D. Gabor, "Theory of communication", *J. Inst. Elect. Eng.*, vol. 93, pp. 429–441, 1946.
4. T. Genossar and M. Porat, "Can one evaluate the gabor expansion using gabor's iterative algorithm?", *IEEE Transactions on Signal Processing*, vol. 40, no. 8, pp. 1852–1861, Aug. 1992.
5. B. Bastiaans, "A sampling theorem for the complex spectrogram, and gabor's expansion of a signal in gaussian elementary signals", *Optical Engineering*, vol. 20, no. 4, pp. 594–598, July 1981.
6. M. Porat and Y. Zeevi, "The generalized gabor scheme of image representation in biological and machine vision", *IEEE Transactions on Pattern Analysis and Machine Intelligence*, vol. 10, no. 4, pp. 452–468, July 1988.
7. J. Daugman, "Complete discrete 2-d gabor transform by neural networks for image analysis and compression", *IEEE Transactions on Acoustics, Speech, and Signal Processing*, vol. 36, no. 7, pp. 1169–1179, July 1988.
8. A. Teuner and B. J. Hosticka, "Adaptive gabor transformation for image processing", *IEEE Transactions on Image Processing*, vol. 2, no. 1, pp. 112–117, Jan. 1993.
9. A. Ibrahim and M. Azimi-Sadjadi, "A fast learning algorithm for gabor transformation", *IEEE Transactions on Image Processing*, vol. 5, no. 1, pp. 171–175, Jan. 1996.
10. I. Daubechies, "The wavelet transform, time-frequency localization and signal analysis", *IEEE Transactions on Information Theory*, vol. 36, pp. 961–1005, Sep. 1990.
11. C. E. Heil and D. F. Walnut, "Continuous and discrete wavelet transforms", *SIAM Rev.*, vol. 31, no. 4, pp. 628–666, Dec. 1989.
12. R. A. Gopinath and C. S. Burrus, *Wavelet transforms and filter banks*, pp. 603–654, NY Academic, 1992.

13. M. R. Portnoff, "Time-frequency representation of digital signals and systems based on short-time fourier analysis", *IEEE Transactions on Acoustics, Speech, and Signal Processing*, , no. 4, pp. 55–69, Feb. 1980.
14. I. Daubechies, "Characterization of functional spaces by means of wavelets", in *Ten Lectures on Wavelets*, chapter 9, pp. 53–106. Montpellier, Capital City, 1992.
15. R. S. Orr, "Derivation of the finite discrete gabor transform using bessel's equality", *Signal Processing*, vol. 30, no. 2, pp. 257–262, 1993.
16. J. Wexler and S. Raz, "Discrete gabor expansions", *Signal Processing*, vol. 21, no. 3, pp. 207–221, Nov. 1990.
17. R. S. Orr, "The order of computation for finite discrete gabor transform", *IEEE Transactions on Signal Processing*, vol. 41, no. 1, pp. 122–130, Jan. 1993.
18. S. Qiu, "Block-circulant gabor-matrix structure and discrete gabor transforms", *Optical Engineering*, vol. 34, no. 10, pp. 2872–2878, Oct. 1995.
19. N. Redding and N. Newsam, "Efficient calculation of finite gabor transforms", *IEEE Transactions on Signal Processing*, vol. 44, no. 2, pp. 190–200, Feb. 1996.
20. I. Daubechies, S. Jaffard, and J-L. Journé, "A simple wilson orthonormal basis with exponential decay", *SIAM J. Math. Anal.*, vol. 22, no. 2, pp. 554–572, Mar. 1991.
21. A. Teuner, P. Nielsen, and B. Hosticka, "An extension to the analytical gabor expansion with applications in image coding", in *Proceedings of the IEEE International Conference on Acoustics, Speech and Signal Processing*, 1994, vol. 5, pp. V–585:V–588.
22. R. Balian, "Un principe d'incertitude fort en théorie du signal ou en mécanique quantique", *C. R. Acad. Sci. Paris*, pp. 292:1357–1362, 1981.
23. F. Low, "Complete sets of wave packets", in *A Passion for Physics-Essays in Honor of Geoffrey Chew*, C. DeTar, Ed., pp. 17–22. World Scientific, Singapore, 1985.
24. G. Battle, "Heisenberg proof of the balian-low theorem", *Lett. Math. Phys.*, vol. 15, pp. 175–177, 1988.
25. D. F. Stewart, L. C. Potter, and S. C. Ahalt, "Computationally attractive real gabor transforms", *IEEE Transactions on Signal Processing*, vol. 43, no. 1, pp. 77–83, Jan. 1995.
26. S. Qian, K. Chen, and S. Li, "Optimal biorthogonal sequence for finite discrete-time gabor expansion", *Signal Processing*, vol. 27, no. 2, pp. 177–185, May 1992.

27. R. Balart, "Matrix reformulation of the gabor transform", *Optical Engineering*, vol. 31, no. 6, pp. 1235–1242, 1992.
28. Jie Yao, "Complete gabor transformation for signal representations", *IEEE Transactions on Image Processing*, vol. 2, no. 2, pp. 152–159, April 1993.
29. J. Yao, P. Krolak, and C. Steele, "The generalized gabor transform", *IEEE Transactions on Image Processing*, vol. 4, no. 7, pp. 978–988, July 1995.
30. W. Kahan, "Numerical linear algebra", *Canadian Math. Bull.*, vol. 9, pp. 757–801, 1966.
31. H. G. Feichtinger and O. Christensen, "Group theoretical approach to gabor analysis", *Optical Engineering*, vol. 34, no. 6, pp. 1697–1703, June 1995.
32. P. Prinz, "Calculating the dual gabor window for general sampling sets", *IEEE Transactions on Signal Processing*, vol. 44, no. 8, pp. 2078–2082, Aug. 1996.
33. J. Makhoul, S. Roucos, and H. Gish, "Vector quantization in speech coding", *PROCEEDINGS OF THE IEEE*, vol. 73, no. 11, pp. 1551–1567, Nov. 1985.
34. N. Levinson, "The wiener rms (root-mean square) error criterion in filter design and prediction", *J. Math. Phys.*, vol. 25, pp. 261–278, 1947.
35. T. Ku and C. J. Kuo, "Preconditioned iterative methods for block toeplitz systems", in *IEEE, CH/2977-7/91*, 1991, pp. 2341–2344.
36. H. Akaike, "Block toeplitz matrix inversion", *SIAM J. Appl. Math.*, vol. 24, no. 2, pp. 234–241, Mar. 1973.
37. G. Labahn, D. K. Choi, and S. Cabay, "The inverses of block hankel and block toeplitz matrices", *SIAM J. Computing*, vol. 19, pp. 98–123, Feb. 1990.
38. H. Wang and H. Yan, "Efficient implementation of gabor transforms for image compression", *ELECTRONICS LETTERS*, vol. 28, no. 9, pp. 870–871, 23rd April 1992.
39. H. S. Malvar, "Lapped transforms for efficient transform/subband coding", *IEEE Transactions on Acoustics, Speech, and Signal Processing*, vol. 38, no. 6, pp. 969–978, June 1990.
40. P. J. Davis, *Circulant Matrices*, John Wiley, 1979.
41. M. Joliot, B. M. Mazoyer, and R. H. Heusman, "In vivo nmr spectral parameter estimation: A comparison between time and frequency domain methods", *Magnetic Resonance in Medicine*, vol. 18, pp. 358–370, 1991.

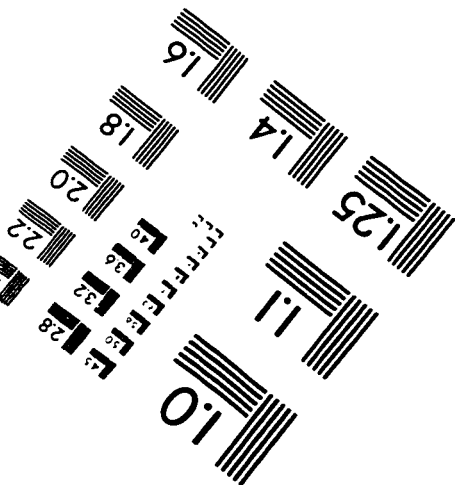
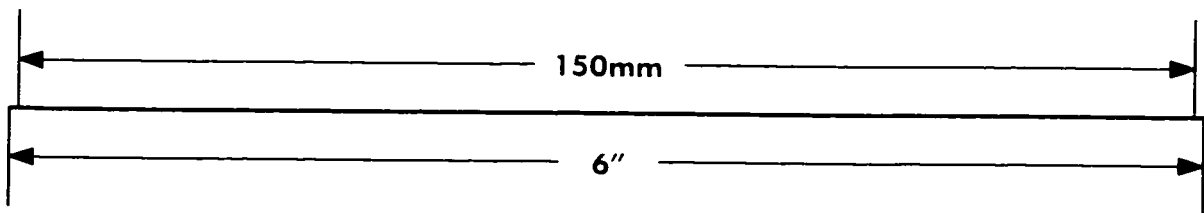
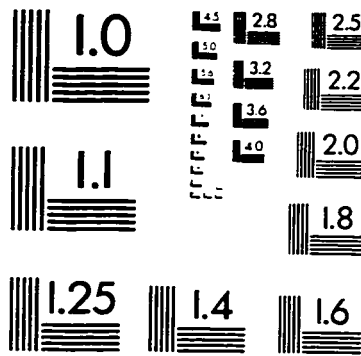
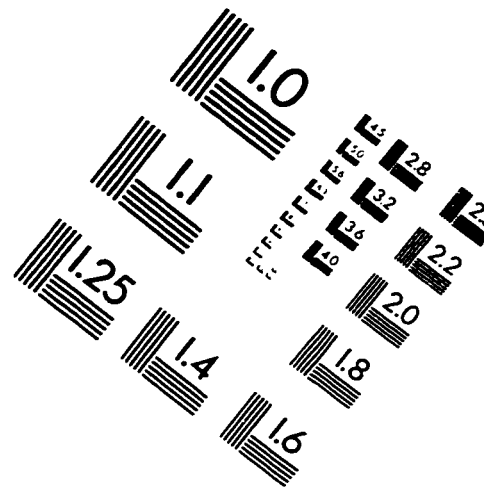
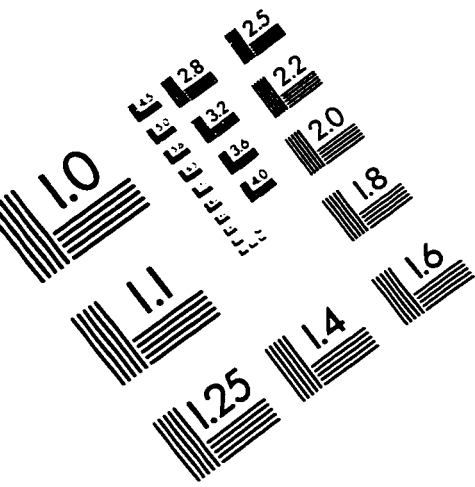
42. J. H. J. Leclerc, "Time-frequency representation of damped sinusoids", *Journal of Magnetic Resonance*, , no. 95, pp. 10–31, 1991.
43. P. A. Angelidis and G. D. Sergiads, "Time-frequency representation of damped sinusoids using the zak transform", *Journal of Magnetic Resonance*, , no. Series A, 103, pp. 191–195, 1993.
44. Y. Lu, S. Joshi, and J. M. Morris, "Noise reduction for nmr fid signals via gabor expansion", *IEEE Transactions on Biomedical Engineering*, vol. 44, no. 6, pp. 512–528, June 1997.
45. Martha D. Bruch, Ed., *NMR Spectroscopy Techniques*, vol. 21 of *PRACTICAL SPECTROSCOPY SERIES*, Marcel Dekker, Inc., second edition, 1996.
46. A. Abragam, *The Principles of Nuclear Magnetism*, Oxford, U.K., 1961.
47. G. Golub and C. Van Loan, *Matrix Computations*, The Johns Hopkins University Press, second edition, 1989.
48. A. K. Jain, "A sinusoidal family of unitary transforms", *IEEE Transactions on Pattern Analysis and Machine Intelligence*, vol. 1, pp. 356–365, Sept. 1979.
49. H. S. Malvar, *Signal Processing with Lapped Transforms*, Norwood, MA: Artech House, 1991.
50. N. R. Murthy and M. N. Swamy, "On the on-line computation of dct-iv and dst-iv transforms", *IEEE Transactions on Signal Processing*, vol. 43, no. 5, pp. 1249–1251, May 1995.
51. Z. Wang, "Fast algorithms for the discrete w transform and for the discrete fourier transform", *IEEE Transactions on Acoustics, Speech, and Signal Processing*, pp. 803–816, Aug. 1984.
52. J. L. Wang and Z. Q. Ding, "Discrete sine transform domain lms adaptive filtering", in *International Conference on Acoustics, Speech, and Signal Processing*, 1985, pp. 260–263.

VITA

Osama Abdl-Wahhab Ahmed

April 19, 1966	Born at CAIRO, EGYPT
July 1988	B.Sc. in Electronics and Communications Eng. Cairo University, Cairo, Egypt
Jan 1990-Oct.1992	Research Assistant, National Telecom. Institute, Cairo, Egypt
Oct.1992-Nov.1994	Research Assistant, KFUPM, Dhahran, Saudi Arabia
July 1994	MS. in Electrical Engineering , KFUPM, Dhahran, Saudi Arabia
Nov.1994-Aug.1998	Lecturer, KFUPM, Dhahran, Saudi Arabia
May 1998	Ph.D. in Electrical Engineering, KFUPM, Dhahran, Saudi Arabia

IMAGE EVALUATION TEST TARGET (QA-3)



APPLIED IMAGE, Inc.
1653 East Main Street
Rochester, NY 14609 USA
Phone: 716/482-0300
Fax: 716/288-5989

© 1993, Applied Image, Inc., All Rights Reserved

